Universität Ulm
Institut für Analytische und Bioanalytische Chemie

Investigation of antimicrobial and antibiofouling systems *via* scanning probe microscopy

DISSERTATION

zur Enlangung des Doktorgrades Dr. rer. nat.
der Fakultät für Naturwissenschaften der Universität Ulm

vorgelgt von
Giada Caniglia
aus Italien, Asiago (Venetien)

Ulm, **2022**

Amtierender Dekan: Prof. Dr. Thorsten Bernhardt
Erstgutachter: Apl. Prof. Dr. Christine Kranz
Zweitgutachter: Prof. Dr. Holger Barth
Tag der Promotion: 25.05.2023

16. Aufwärts

„Wie komm ich am besten den Berg hinan?“

„Steig nur hinauf und denk nicht dran!“

(*Die fröhliche Wissenschaft*, F. Nietzsche)

Acknowledgments/*Agradecimientos*

I have written these acknowledgments in Spanish first, as I could express them better from the heart. I hope the translation does not lose its deepness and meaning. When I chose to embark on this journey, I knew that I would have said goodbye to many important people in my life, but this is life and I can happily say that these three years gave me the best persons, without whom all this work would not have been possible. I certainly would not be here without the unconditional support of my mentors in Tenerife whom I thank for the years and months before my Ph.D.: Dr. Javier Izquierdo, who pushed me to pursue my Ph.D. and believed in me from the first moment; Dr. Ricardo Souto who made me love electrochemistry and, of course, Dr. Pedro Martín Zarza, to whom I always have a special thought, thanks to our long discussions that sometimes went into the philosophical.

A special and sincere thank goes to my supervisor, Apl. Prof. Dr. Christine Kranz, who bet on me and has always been my point of reference both as a scientist and as a woman. Her decisiveness, strength, and sense of fairness have made me grow not only professionally but also as a person. To quote Rita Levi Montalcini: "*The choice of a young person depends on his inclination, but also on the luck of finding a great teacher*", I was lucky. Thank you.

My arrival in Ulm brought me good colleagues and for this, I thank my colleagues at iABC, the whole Break Biofilm group, and our infinite patient and dedicated administrative assistant Monja Claus for making life easier and for the nice conversations. A special thank must be directed to Julian Kund and Andreas Hellmann, for all the hours spent in our *SPM lab*, for the *Feierabend* beers… for the unforgettable memories. But I must stop to address a warm and unconditional thank you to my – not only colleague – but also my exceptional friend (and often psychologist), Andrea Teuber, for all the moments you have been present, moments of joy, stress, nervousness, or life-saving craziness. This acknowledgment is perhaps the most complicated for me because there are not enough words to describe how much I feel blessed for that lucky month of July when you built up your "*Andrea's Spielplatz*" and from there began that adventure made of long evenings at the university, deep conversations and incredible trips that filled *and fill* my heart with warmth and happiness. I will never forget all the moments I hit the ground and there you were, holding out your hand, with a sweet smile... or with a well-deserved *flip-flop*. I always like to say that friends are the family we choose in life… you know which part of my heart will always belong to you.

And finally, for sure not for importance, I thank my parents, Ester and Paolo. *Grazie!* I can only imagine the effort they have made to support my decisions, to push me to always give the best of me and I hope they are somehow proud of their daughter at the end of this stage: the thought of the hard work of the Venetian people and the Sicilian boldness are characteristics that flow in my blood.

I take this opportunity to thank also all the people who helped in the development of this thesis either in discussions and explanations or for providing me with laboratories and instruments: thanks to Prof. Dr. Boris Mizaikoff, director and head of the iABC, to Dr. Gregor Neusser, for the hours at the FIB center (sourcing *scratches*...), to Dr. Sven Daboss for the advice on AFM force

spectroscopy and sincere thanks to the Institut für Pharmakologie und Toxikologie (and in particular to Anna Anastasia) and the Institut für Mikrobiologie und Biotechnologie for all the times they have provided me with bacterial cultures. I also would like to acknowledge our collaborators from the Warwick Electrochemistry and Interface group (University of Warwick), led by Prof. Dr. Patrick Unwin, for the possibility to join their laboratories and for the kind atmosphere during my stay.

Thanks to all of you.

He escrito estos agradecimientos en español primero ya que pude exprimirlos mejor desde el corazón. Espero que la traducción en inglés tenga la misma profundidad y el mismo sentido. Cuando elegí emprender este viaje sabía que habría dicho adiós a muchas personas importantes en mi vida, pero así es la vida y puedo alegremente decir que estos tres años me han regalado las mejores personas, sin las cuales todo este trabajo no hubiera sido posible. Desde luego no estaría aquí sin el apoyo incondicionado de mis mentores en Tenerife a quienes agradezco los años y meses previos mi doctorado: Dr. Javier Izquierdo, quien me empujó para seguir mi doctorado y creyó en mi desde el primer momento; Dr. Ricardo Souto quien me hizo amar la electroquímica y, por supuesto, Dr. Pedro Martín Zarza a quien siempre tengo un pensamiento especial gracias a nuestras largas discusiones que a veces se iban en lo filosófico.

*Un especial y sincero agradecimiento va dirigido a mi directora, Apl. Prof. Dr. Christine Kranz, quien apostó en mí y siempre ha sido mi punto de referencia tanto como científica que como mujer. Su decisión, fortaleza y sentido de lo justo me han hecho crecer no solo profesionalmente sino también como persona. Por citar Rita Levi Montalcini: "*La elección de un joven depende de su inclinación, pero también de la suerte en encontrar un gran maestro*", yo tuve esta suerte. Gracias.*

Mi llegada en Ulm me aportó buenos colegas tanto en el instituto como fuera y por ello agradezco a mis colegas en iABC, a todo el grupo de Break Biofilm y por supuesto a nuestra paciente y dedicada asistente administrativa Monja Claus, para facilitarnos la vida todos los días entre risas, charlas y trabajo. Un especial agradecimiento tengo que dirigirlo a Julian Kund y Andreas Hellmann, por todas las horas pasadas en nuestro SPM lab*, por las cervezas compartidas, por la alegría en las discusiones, por los recuerdos bonitos e inolvidables. Pero debo pararme para dirigir un afectuoso e incondicional agradecimiento a mi – no son colega – sino gran amiga (y muchas veces psicóloga), Andrea Teuber, por todos los momentos en que has estado presente, momentos de alegría, estrés, nerviosismo o salvadora locura. Esta parte de agradecimiento es quizás la más complicada para mí porque no hay palabras suficientes para describir lo mucho que me siento bendecida por aquel afortunado mes de julio, cuando montaste tu "*Andrea´s Spielplatz*" y desde ahí empezó esa aventura hecha de largas tardes en la universidad, profundas conversaciones e increíbles viajes que me llenaron y llenan el corazón de ternura y alegría. Nunca olvidaré todos los momentos que toqué el suelo y ahí estabas tú, tendiéndome tu mano, con una cálida sonrisa… o con una merecida chancla. Siempre me gusta*

decir que los amigos son la familia que nosotros elegimos en la vida… ya sabes la parte de mi corazón que te pertenece.

Y finalmente, por supuesto no por importancia, agradezco a mis padres, Ester y Paolo. Grazie! *Puedo solo imaginar el esfuerzo qua han hecho para apoyar mis decisiones, empujarme en dar siempre lo mejor de mí y espero que de alguna forma estén orgullosos de su hija al terminar esta etapa: el pensamiento del duro trabajo véneto junto con la chispa traviesa siciliana son características que fluyen en mi sangre.*

Aprovecho para agradecer también todas las personas que han ayudado en el desarrollo de esta tesis ya sea en discusiones y explicaciones o por facilitarme los laboratorios e instrumentos: gracias a Prof. Dr. Boris Mizaikoff, director y jefe del iABC, a Dr. Gregor Neusser, por las horas en el FIB center (buscando scratches*…), a Dr. Sven Daboss por los consejos en AFM force spectroscopy y un sincero agradecimiento al Institut für Pharmakologie und Toxikologie (e in particular a Anna Anastasia) y el Institut für Mikrobiologie und Biotechnologie por todas las veces que me han procurado las culturas de bacteria. También quisiera agradecer a nuestros colaboradores del grupo de investigación* Warwick Electrochemistry and Interface *(Universidad de Warwick), dirigido por el Prof. Dr. Patrick Unwin, por la posibilidad de incorporarme a sus laboratorios y el amable ambiente durante mi estancia.*

Gracias a todos ustedes.

ABSTRACT

Given the increasingly high resistance of biofilms to conventional antibiotics, the demand for formulations of new and more effective antimicrobial agents is steadily increasing, due to critically economic, industrial, and healthcare concerns. Biofilms are ubiquitous communities of bacteria that can grow on almost any type of surfaces. The crucial step in biofilm formation is the cell-surface interaction that leads to the attachment and subsequent proliferation of bacteria across a substrate. Bacterial attachment is highly influenced by several surface properties, including hydrophobicity, surface charge density, and the potential presence of antimicrobials. Thus, functionalization and surface modification are one of the most effective strategies to inhibit the formation of biofilms, by preventing the first cell attachments.

In this thesis, different formulations of antimicrobial and antibiofouling systems have been investigated, focusing on the understanding of bacterial behavior in the early stages of biofilm formation. With this purpose, scanning probe microscopy (SPM) techniques, such as scanning electrochemical microscopy (SECM), scanning electrochemical cell microscopy (SECCM), and atomic force microscopy (AFM), have been used to develop and characterize the antimicrobial/antibiofouling surfaces presented within the scope of this thesis. As the fundamental priniciple of any SPM techniques is based on the interaction of a micro- and nano-sized probe, they offer the possibility (*i*) to investigate the bacterial cell/surface interaction down to the single-cell level, (*ii*) allow localized quantitative *in situ* electroanalysis, and (*iii*) provide fast surface modification at the micro- and nanoscale level. Three efficient and promising antimicrobial systems will be herein described.

The first antimicrobial system consists of pulsed-deposited polydopamine on gold (e-PDA), which was tested against *Escherichia coli*. Polydopamine, a mussel-inspired biocompatible polymer, is well-known for its excellent adhesive properties and is used nowadays in a multitude of applications, *e.g.*, in biomolecule grafting processes and as coating in filtration membranes. In this thesis, the surface charge density of e-PDA has been locally investigated as a function of the pH using AFM force spectroscopy. The point of zero charge (PZC) of the e-PDA has been – for the first time – determined, being PZC = 5.37 ± 0.06. The antibiofouling effects of e-PDA have been studied against *E. coli* as a function of the surface charge density of the polymer, by controlling the pH of the culture media. AFM force spectroscopy allowed the quantitative evaluation of the adhesion of *E. coli*, which exhibits higher adhesion force on positively charged e-PDA (pH 5), in comparison to *E. coli* grown on neutral and negative e-PDA (pH 5.5 and pH 7, respectively). It has been also observed that the bacterial adhesion on neutral and

negatively charged polymer does not change significantly, indicating that the electrostatic interactions between the bacteria and polymer are not always the main cause of cell attachment, but also other interactions – *e.g.*, hydrophobic interactions – might overlap and favor bacterial adhesion (and biofilm proliferation).

The second antimicrobial system is a composite antimicrobial thin film material based on silver nanoparticles (AgNPs) embedded in a biocompatible fluoropolymeric matrix. An *in situ* SECM mechanistic study of the silver(I) ion release from the embedded AgNPs has been performed. The kinetic data of silver(I) ion release were recorded for the composite immersed in an aqueous solution within the first 14 h of immersion and further evaluated using the Korsmeyer-Peppas model. This model describes the mechanism of drug release from polymers. Results revealed that the release of the antimicrobial agent – silver(I) ions – follows a non-Fickian diffusion, *e.i.,* the diffusion of the silver(I) ion is highly dependent on the relaxation of the polymeric chains (swelling) of the matrix. AFM studies confirmed the swelling of the polymer over time with a total swelling equal to 128 ± 5 nm when the composite was immersed in MilliQ water during 14 h. The antimicrobial effects of these composite films have been investigated by mapping the morphological changes of bacterial cells (*Pseudomonas fluorescens*) in contact with the composite *via* AFM. The study revealed that exposure to the antimicrobial composite leads to an alteration of the shape and size of bacteria, promoting a transition from rod-shaped cells (control) to smaller coccoidal-like bacteria.

The third system is based on the synergistic antimicrobial effects of AgNPs and e-PDA. For the first time, structured patterns of electrodeposited AgNPs on e-PDA thin films have been generated *via* SECCM. The optimization of the electrodeposition was performed by forming arrays of 4x4 AgNPs spots with a diameter of ~5 µm under different experimental conditions. This protocol favored the execution of screening experiments and enabled single-cell studies on the same substrate. The optimal parameters for the electrodeposition of AgNPs lead to particles with a diameter smaller than 20 nm. AFM and AFM force spectroscopy studies also showed that bacteria (*E. coli*) attached in the proximity of the AgNPs spots (less than 2 µm distance) exhibit increased hydrophobicity, loss of stiffness, and major corrugation due to cell membrane damages than bacteria attached far away (more than 20 µm distance) from the AgNPs spots.

TABLE OF CONTENTS

ABSTRACT ..... **XI**

LIST OF PUBLICATIONS ..... **XV**

ABBREVIATIONS AND NOMENCLATURE ..... **XVI**

SCOPE OF THE THESIS ..... **XIX**

1.CHAPTER 1: INTRODUCTION **21**

1.1.STATE-OF-ART AND MOTIVATION 21

2.CHAPER 2: SCANNING PROBE MICROSCOPY TECHNIQUES **25**

2.1.INTRODUCTION 25

2.2.SCANNING ELECTROCHEMICAL MICROSCOPY 26

2.2.1.Fundamentals *26*

2.2.2.SG-TC mode combined with anodic stripping voltammetry *29*

2.3.SCANNING ELECTROCHEMICAL CELL MICROSCOPY 31

2.3.1.Fundamentals *31*

2.4.ATOMIC FORCE MICROSCOPY 34

2.4.1.Fundamentals *34*

2.4.2.AFM force spectroscopy *37*

3.CHAPTER 3: ANTIBIOFOULING, THE ROLE OF THE SURFACE CHARGE DENSITY **43**

3.1.BIOFOULING AND SURFACE CHARGE DENSITY: WHY IS IT IMPORTANT? 43

3.2.POLYDOPAMINE: A VERSATILE, BIOCOMPATIBLE POLYMER 47

3.3.ATOMIC FORCE MICROSCOPY AND INFRARED SPECTROSCOPIC STUDIES ON THE ROLE OF SURFACE CHARGE FOR THE ANTI-BIOFOULING PROPERTIES OF POLYDOPAMINE FILMS 49

3.3.1.Introduction *49*

3.3.2.Results and discussion *50*

3.3.3.Conclusions *58*

4.CHAPTER 4. SILVER NANOPARTICLES A WEAPON AGAINST BACTERIA **61**

4.1.AGNPS: SYNTHESIS AND ANTIMICROBIAL MECHANISMS 62

4.1.1.Synthesis of AgNPs *62*

4.1.2.Mechanism of action of AgNPs: a synergistic activity *65*

4.2.SILVER-FLUOROPOLYMER (AG-CFX) FILMS: KINETIC STUDY OF SILVER RELEASE, AND SPECTROSCOPIC-MICROSCOPIC INSIGHT INTO THE INHIBITION OF P. FLUORESCENS BIOFILM FORMATION 69

4.2.1.Introduction *69*

4.2.2.Results and discussion *70*

4.2.3.Conclusions *81*

4.3.ELECTRO-DEPOSITION OF ANTIMICROBIAL SILVER NANOPARTICLES ON POLYDOPAMINE FILMS BY SCANNING ELECTROCHEMICAL CELL MICROSCOPY 82

4.3.1.Introduction *82*

4.3.2.Results and discussion *83*

4.3.3.Conclusions *94*

5.CHAPTER 5. EXPERIMENTAL SECTION 95

5.1.ATOMIC FORCE MICROSCOPY AND INFRARED SPECTROSCOPIC STUDIES ON THE ROLE OF SURFACE CHARGE FOR THE ANTI-BIOFOULING PROPERTIES OF POLYDOPAMINE FILMS: CHAPTER 3.3 95

5.1.1.Materials and chemicals *95*

5.1.2.Electrochemical deposition of polydopamine *95*

5.1.3.Bacterial culture conditions *96*

5.1.4.AFM and AFM force spectroscopy experiments *96*

5.1.5.ATR-FTIR experiments *97*

5.2.SILVER-FLUOROPOLYMER (AG-CFX) FILMS: KINETIC STUDY OF SILVER RELEASE, AND SPECTROSCOPIC-MICROSCOPIC INSIGHT INTO THE INHIBITION OF P. FLUORESCENS BIOFILM FORMATION: CHAPTER 4.2 97

5.2.1.Materials and chemicals *97*

5.2.2.Synthesis and characterization of Ag-CF_X films *97*

5.2.3.Kinetics of silver(I) ion release *98*

5.2.4.Swelling study via AFM *99*

5.2.5.Bacterial culture conditions and morphological study *99*

5.3.ELECTRO-DEPOSITION OF ANTIMICROBIAL SILVER NANOPARTICLES ON POLYDOPAMINE FILMS BY SCANNING ELECTROCHEMICAL CELL MICROSCOPY: CHAPTER 4.3 100

5.3.1.Materials and chemicals *100*

5.3.2.Electrochemical deposition of polydopamine *100*

5.3.3.Electro-deposition of AgNPs micro-spots *101*

5.3.4.Scanning electron microscopy (SEM) *102*

5.3.5.Bacterial culture conditions *102*

5.3.6.AFM and AFM force spectroscopy experiments *102*

REFERENCES 103

CURRICULUM VITAE 141

DECLARATION OF AUTHORSHIP 147

EIDESSTATTLICHE ERKLÄRUNG 147

LIST OF PUBLICATIONS

Articles

1. Caniglia, G.; Kranz, C. Scanning Electrochemical Microscopy and Its Potential for Studying Biofilms and Antimicrobial Coatings. *Anal. Bioanal. Chem.* **2020**, *412* (24), 6133–6148. https://doi.org/10.1007/s00216-020-02782-7.
2. Caniglia, G.; Sportelli, M. C.; Heinzmann, A.; Picca, R. A.; Valentini, A.; Barth, H.; Mizaikoff, B.; Cioffi, N.; Kranz, C. Silver-Fluoropolymer (Ag-CF_X) Films: Kinetic Study of Silver Release, and Spectroscopic-Microscopic Insight into the Inhibition of P. Fluorescens Biofilm Formation. *Anal. Chim. Acta* **2022**, *1212* (April), 339892. https://doi.org/10.1016/j.aca.2022.339892.
3. Caniglia, G.; Tezcan, G.; Meloni, G. N.; Unwin, P. R.; Kranz, C. Probing and Visualizing Interfacial Charge at Surfaces in Aqueous Solution. *Annu. Rev. Anal. Chem.* **2022**, *15* (1). https://doi.org/10.1146/annurev-anchem-121521-122615.
4. Caniglia, G.; Teuber, A.; Barth, H.; Mizaikoff, B.; Kranz, C. Atomic force and infrared spectroscopic studies on the role of surface charge for the anti-biofouling properties of polydopamine films. *Anal. Bioanal. Chem.* **2022**, https://doi.org/10.1007/s00216-022-04431-7.
5. Teuber, A.; Caniglia, G.; Wild, M.; Godejohann, M.; Kranz, C.; Mizaikoff, B.; Espresso Laser Spectroscopy: Diamond Thin-Film Waveguides for the Qualitative and Quantitative Analysis of Caffeine. *ACS Sensors.* **2022** (*revised manuscript submitted*).
6. Caniglia, G.; Valavanis, D.; Tezcan, G.; Barth, H.; Unwin, P. R.; Kranz, C. Electrodeposition of antimicrobial silver nanoparticles on polydopamine films by scanning electrochemical cell microscopy (*in preparation, 2022*).

Book chapter:

7. Hellmann, A.; Caniglia, G.; Kranz, C. Applications of Miniaturized Electrochemical Biosensors. In *Reference Module in Biomedical Sciences*; Elsevier, 2022. https://doi.org/10.1016/B978-0-12-822548-6.00152-7.

This thesis was conducted in the framework of the “Break Biofilms” project that has received funding from the European Union’s Horizon 2020 research and innovation program under the Marie Skłodowska Curie Grant Agreement No. 813439.

ABBREVIATIONS AND NOMENCLATURE

Abbreviations

AFM	Atomic force microscopy
AFM-FS	Atomic force microscopy-force spectroscopy
Ag-CF_X	Fluoropolymer-based nanoparticle composite
AgNPs	Silver nanoparticles
AM AFM	Amplitude modulation atomic force microscopy
AMP	Antimicrobial polymer
ASV	Anodic stripping voltammetry
ATP	Adenosine triphosphate
ATR-FTIR	Attenuated total reflectance Fourier transform infrared spectroscopy
CE	Counter electrode
CLSM	Confocal laser scanning microscopy
DAC	Dopamine-chrome
DAQ	Dopamine-quinone
DLVO	Derjaguin, Landau, Verwey, and Overbeek
DMT	Derjaguin-Muller-Toporov
DNA	Deoxyribonucleic acid
EDL	Electrical double layer
e-PDA	Electrochemically deposited polydopamine
EPS	Extracellular polymeric substances
ETAAS	Electrothermal atomic absorption spectroscopy
FD	Force-distance (curve)
FIB	Focused ion beam
FM AFM	Force modulation atomic force microscopy
IBS	Ion beam sputtering
KP	Korsmeyer-Peppas
LB	Luria-Bertani culture medium
LOD	Limit of detection
LOQ	Limit of quantification
MIC	Minimal inhibitory concentration
NPs	Nanoparticles
OM	Outer membrane
PBE	Poisson-Boltzmann equation
PBS	Phosphate buffer solution
PDA	Polydopamine
PTFE	Polytetrafluorethylene
PZC	Point of zero charge
QRCE	Quasi reference counter electrode

RE	Reference electrode
RG	Ratio of insulating glass sheath radius and microelectrode radius
ROS	Reactive oxygen species
SECCM	Scanning electrochemical cell microscopy
SECM	Scanning electrochemical microscopy
SEM	Scanning electron microscopy
SG/TC	Sample generation/tip collection SECM mode
SPM	Scanning probe microscopy
STM	Scanning tunnelling microscope
SWV	Square-wave voltammetry
TG/SC	Tip generation/sample collection SECM mode
UME	Ultramicroelectrode
WE	Working electrode
XPS	X-ray photoelectron spectroscopy

Nomenclature

A	Area (m^2)
A_H	Hamaker constant (J)
C_0	Bulk concentration
d	Tip-sample distance
D_0	Diffusion coefficient
e	Unit charge (1.602 x 10^{-19} C)
E	Potential (V)
E_g	Particle growth potential (V)
E_n	Particle nucleation potential (V)
E_S	Young´s modulus (Pa)
f, f_A, f_B	Frequency (s^{-1})
F	Faraday constant (96 485 s A mol^{-1})
F_{adh}	Adhesion force (N)
F_{con}	Conservative force (N)
F_{dis}	Dissipative force (N)
F_{EDL}	Electric double layer force
F_{VdW}	Van der Waals force
i	Current (A)
i_{ss}	Steady-state current (A)
I	Normalized current (i/i_{ss})
I_{DC}	Induced ionic current (A)
k	Rate constant (h^{-1})
k_B	Boltzmann constant (1.381 x 10^{-23} J K^{-1})
L	Normalized tip-substrate distance (d/r)

m_O	Steady-state mass transport coefficient (g s^{-1} cm^{-1})
pK_a	Dissociation constant
q	Electric charge (C)
r, r_0	Tip radius (m)
S_a	Roughness parameter, arithmetical mean height (m)
S	Slope of the calibration curve
S_y	Standard deviation of the response in the calibration curve
t	Time (s)
t_g	Particle growth time (s)
t_n	Particle nucleation time (s)
v	Stripping scan rate is square-wave voltammetry (V s^{-1})
V	Voltage (V)
z	Ion valency
Greek letters	
δ	Indentation (m)
δ_m	Indentation at maximum adhesion (m)
ε	Dielectric constant of the medium
ε_0	Vacuum permittivity (8.854 x 10^{-12} A s V^{-1} m^{-1})
η	Overpotential (V)
λ_D	Debye length (m)
ν	Poisson´s ratio
σ_S	Surface charge density of the sample in aqueous media (C m^{-2})
σ_T	Surface charge density of tip in aqueous media (C m^{-2})
ψ	Electric potential (V)

SCOPE OF THE THESIS

The present thesis is focused on the development and characterization of antimicrobial and antibiofouling systems based on polymeric surfaces and nanoparticles-based composites, using scanning probe techniques, in particular scanning electrochemical microcopy and atomic force microscopy. The thesis is divided into five chapters presenting the state-of-art and scientific background (**Chapter 1** and **Chapter 2**), the role of surface charge density in biofouling processes (**Chapter 3**), and the antimicrobial effects of AgNPs on the morphology and the nanomechanical properties of bacterial cells (**Chapter 4**). The experimental parts are summarized in **Chapter 5**.

Chapter 1. Introduction. In this chapter, an overview of the state-of-art and the motivation of this thesis is presented.

Chapter 2. Scanning probe microscopy techniques. In this chapter, the fundamentals of scanning probe microscopy techniques used in the course of this thesis are explained with special attention to scanning electrochemical microscopy (SECM), scanning electrochemical cell microscopy (SECCM), and atomic force microscopy (AFM). **Chapter 2** is partly based on the following reviews:

- Caniglia, G.; Kranz, C. Scanning Electrochemical Microscopy and Its Potential for Studying Biofilms and Antimicrobial Coatings. *Anal. Bioanal. Chem.* **2020**, *412* (24), 6133–6148. https://doi.org/10.1007/s00216-020-02782-7.
  Copyright: this is an open-access article distributed under the terms of the *Creative Commons CC BY license*, which permits unrestricted use, distribution, and reproduction in any medium, provided the original work is properly cited. Copyright © 2020, Springer Nature.

- Caniglia, G.; Tezcan, G.; Meloni, G. N.; Unwin, P. R.; Kranz, C. Probing and Visualizing Interfacial Charge at Surfaces in Aqueous Solution. *Annu. Rev. Anal. Chem.* **2022**, *15* (1). https://doi.org/10.1146/annurev-anchem-121521-122615.
  Copyright: the material of this article is reproduced with permission from the Annual Review of Analytical Chemistry, Volume 15 © 2022 by Annual Reviews, http://www.annualreviews.org

Chapter 3. The role of surface charge density for bacterial adhesion. The study on the influence of the surface charge of a biocompatible polymer, namely polydopamine will be presented in **Chapter 3**. The antibiofouling properties of electrodeposited polydopamine have been evaluated *via* atomic force microscopy-based force microscopy and attenuated total reflection Fourier transform infrared spectroscopy. A thorough characterization of the polymer in terms of pH-dependency of surface charge density is presented. This chapter is partly based on the following article:

- Caniglia, G.; Teuber, A.; Barth, H.; Mizaikoff, B.; Kranz, C. Atomic force and infrared spectroscopic studies on the role of surface charge for the anti-biofouling properties of polydopamine films. *Anal. Bioanal. Chem.* **2022**, https://doi.org/10.1007/s00216-022-04431-7.

  Copyright: this is an open-access article distributed under the terms of the *Creative Commons CC BY license*, which permits unrestricted use, distribution, and reproduction in any medium, provided the original work is properly cited. Copyright © 2022, Springer Nature.

Chapter 4. Silver nanoparticles: a weapon against bacteria. This chapter is focused on the development and characterization of composite materials containing silver nanoparticles. In particular, embedded nanoparticles either in Teflon-based polymers or mussel-inspired biocompatible catecholamines (polydopamine) were studied. The results of these studies are partly published in the following article:

- Caniglia, G.; Sportelli, M. C.; Heinzmann, A.; Picca, R. A.; Valentini, A.; Barth, H.; Mizaikoff, B.; Cioffi, N.; Kranz, C. Silver-Fluoropolymer (Ag-CFX) Films: Kinetic Study of Silver Release, and Spectroscopic-Microscopic Insight into the Inhibition of P. Fluorescens Biofilm Formation. *Anal. Chim. Acta* **2022**, *1212* (April), 339892. https://doi.org/10.1016/j.aca.2022.339892.

  Copyright: the author of this Elsevier article retains the right to include it in a thesis or dissertation, provided it is not published commercially. Permission is not required, but the author must ensure that the journal is referred to as the original source. Copyright © 2022, The Authors. Published by Elsevier B.V.

Chapter 5. Experimental section. The description of experimental methods used in Chapter 3 and Chapter 4 is explained here in detail.

1 INTRODUCTION

1.1. State-of-art and motivation

Since the discoveries of Antonie van Leuwenhoek in 1674, it has been accepted that bacteria can exist in two different types of entities: as planktonic, *i.e.*, free-living motile cells often equipped with flagella, and as sessile, *i.e.*, as biofilms [1,2]. The transition from a planktonic to a sessile lifestyle is characterized by a change in phenotypic and physiological processes [3].

Biofilms are defined as well-organized communities of bacteria that attach to and colonize solid surfaces [4]. Although biofilms have many important functions in biogeochemical and bioremediation processes [5,6], they have also become a globally critical concern since they exhibit up to 1000-times greater resilience against antibiotics and disinfectants, compared to their planktonic counterparts [5,7]. Biofilms are ubiquitous, and the ability of bacteria to stick to both biotic and abiotic surfaces leads to serious problems not only in industrial sectors, where biofilms account for US$ 4,000 billion per year but also in the healthcare domains, as according to the US National Institute of Health, over 80% of microbial infections in humans are due to biofilms [8].

The formation of biofilms is a well-regulated multi-step process that begins with bacterial adhesion to a surface or tissue, followed by cell division, aggregation,

proliferation, and the formation of a 3D biofilm structure (Figure 1.1) [9]. During the evolution of the biofilm, bacteria secrete extracellular polymeric substances (EPS), which form a viscous matrix composed mostly of extracellular nucleic acids, proteins, and polysaccharides that serves as a physical barrier against external stressors [3,9,10].

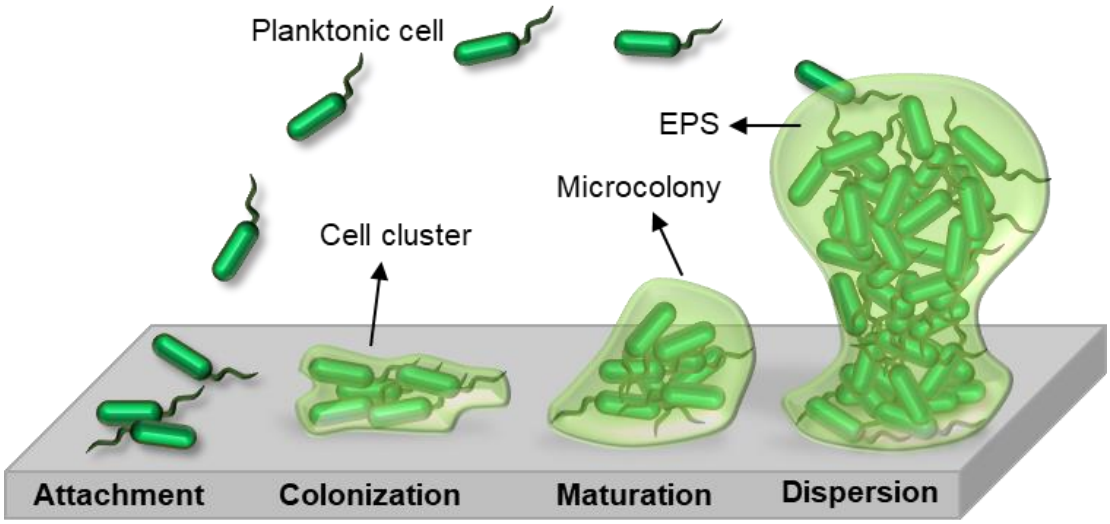

Figure 1.1. Schematic of the steps involved in the formation of bacterial biofilms.

Due to their versatility, bacteria are able to attach to surfaces with a varied range of physical and chemical properties. Cells adhere to metal surfaces, wood, cement, and a wide spectrum of polymeric materials, such as polyvinyl chloride (PVC), polyethylene, polypropylene, and latex [11]. However not every material exhibits the same susceptibility to bacterial attachment and biofilm formation. For instance, studies of marine biofilms demonstrated that bacterial proliferation is higher in plastic, such as polyethylene terephthalate (PET) than in metallic and wooden substrates [12]. Also, aluminum-based materials show significant resistance to biofouling, however when these materials are doped with iron, bacterial colonization increases [13]. These studies reveal that the physicochemical properties of the substrates highly influence the first attachment of microorganisms. Surface energy and surface charge density are the most critical factors affecting the ability of bacteria to adhere to substrates – and form biofilms. Most studies report that substrates with low surface energy (*i.e.,* hydrophobic surfaces) hinder or reduce bacterial proliferation [11], due to the hydrophilic nature of the majority of bacteria. Further, considering that bacteria possess a net negative surface charge, due to the presence of carboxyl, phosphate, and amino groups in the outer envelope, increased adhesion is often observed on positively charged surfaces [14]. However, even though numerous studies have shown reduced bacterial adhesion on negatively charged

surfaces, the relation between surface charge and cell adhesion is still not fully understood, since contradictory results are often reported [14]. Indeed, bacteria can overcome the electrostatic repulsion and adhere strongly to negatively charged surfaces, and form biofilms. Rzhepihevska et al. [15] suggested that the adhesion of gram-negative bacteria to negatively charged surfaces might be promoted by the presence of lipopolysaccharides at the surface of the outer membrane of the bacteria (such as *E. coli* and *P. aeruginosa*). Although, the interaction of bacteria with surfaces is intensively studied, further research is still needed to provide better insight into how surface charge density affects cell adhesion and biofilm proliferation.

Bacterial adhesion and biofilm development are also reduced or prevented by modifying the substrates of interest with bactericidal agents, *via* structural functionalization of the surface or by coating the surface with antimicrobial materials. Up to date, numerous antimicrobials have been screened regarding their ability to inhibit biofilms [16]. Here the focus is on engineered nanostructured antimicrobial materials, which have opened new perspectives for the development of multifunctional and broad-spectrum antimicrobials. Nanostructured antimicrobials include metal NPs (AgNPs, CuNPs, AuNPs) and metal oxide NPs (ZnONPs, TiO_2NPs, MgONPs) [17]. Silver and its compounds, including AgNPs, are the longest-known antibacterial agents that can inhibit bacterial growth at very low concentrations. Indeed, recent studies showed that AgNPs have a minimum bactericidal concentration (MCB) in the range of 3-7 µg/mL against gram-negative bacteria [18] and 10-14 µg/mL against gram-positive bacteria [19]. The antimicrobial activity of AgNPs – and NPs in general – can be synergistically enhanced by the incorporation of the AgNPs into antimicrobial/antibiofouling polymeric matrices [20–22]. The mechanism of action of such AgNPs-polymer composits is based on the controlled release of metal ions and the antibacterial activity of the polymer itself [20,23]. However, the formulation and preparation of new AgNPs-polymer systems highly depend on the nature of the polymer – functional groups, hydrophobicity, conductivity – and the final targeted application – *e.g.*, medical or industrial. Hence, the selection of fast screening methods to evaluate the antimicrobial activity of new formulations is often critical.

Optical microscopy methods, spectroscopic techniques, and proteomic methods are powerful strategies routinely used to test and characterize antimicrobial materials. These methods provide overall information about the microbial population – *e.g.,* cell wall disintegration and the number of dead/alive cells – but are unable to bring information at the single-cell level [24,25]. Scanning probe microscopy (SPM) techniques offer the possibility to study the early stages of cell attachment and the influence of the antimicrobials down to the microscale and molecular level. Atomic force microscopy

(AFM) [26] not only allows the investigation of bacterial cells in terms of morphological changes with excellent spatial resolution but also permits the analysis of nanomechanical properties – adhesion and elasticity – at the single-cell level [27,28]. These properties are useful to understand the changes in the cell envelope when bacteria have been grown, for example, under stressful conditions. Scanning electrochemical microscopy (SECM) [29], an electroanalytical SPM technique, has shown its potential for locally investigating not only concentration profiles of target molecules, such as metabolites [30,31], during biofilm formation but also for the kinetics of drugs released from antimicrobial substrates [32,33]. Scanning electrochemical cell microscopy (SECCM), one of the most recently developed SPM techniques [34], has been employed for the investigation of single events in confined nanoscale-sized electrochemical cells, such as the electrodeposition of single AgNPs [35] or the crystallization of $CaCO_3$ [36]. The possibility to create confined electrochemical cells permits the modification of a wide range of surfaces with the formation of tens of spots down to the nanoscale level [37,38]. The surface patterning at micro- and nanoscale level allows the acquisition of large datasets in a short period of time and the possibility to perform fast screening experiments.

The object of the presented thesis is to contribute to the understanding of bacterial behavior under different stress conditions at the single-cell level using SPM techniques.

2 SCANNING PROBE MICROSCOPY TECHNIQUES

2.1. Introduction

The first attachment of bacteria and the formation of biofilms are processes influenced by many factors, such as hydrophobicity, chemical structure, and surface charge, presence of antimicrobials in the medium, as well as temperature, pH, ionic strength, and nutrient content of the environment [2,39]. Several well-established analytical methods ranging from spectroscopic techniques (element and molecular specific) [40–42], microscopic techniques (electron, optical) [43,44], electrochemical techniques (bulk and laterally resolved) [45–47] and generally sensing methods, are nowadays routinely used to investigate the multistage processes of biofilm formation and the influence of the various parameters [48].

Although these are well-established techniques that play a pivotal role in understanding biofilms, the investigation of biofilm formation at the single-cell level is challenging and not always feasible with conventional methods. On the counter part, SPM is a family of techniques that operates in the range of the micro-scale level down to the atomic-scale, providing a variety of physical and chemical information – *e.g.*, electrochemical, topographical, nanomechanical information – on the sample in dependence of the specific probe-sample interaction. Since the introduction in 1982 of scanning tunneling microscopy (STM) [49], the earliest member of the SPM family, SPM

techniques have found numerous applications to study biological entities such as cells [31,50–53] and there is a large body of literature proving their potential to investigate bacterial samples and antimicrobial systems [54,55]. This thesis is focused on three of the most important SPM techniques: SECM [56–58], SECCM [59,60], and AFM [61–63]. Theoretical background as well as the fundamental principles are described in the following sections of this chapter.

2.2. Scanning Electrochemical Microscopy

2.2.1. Fundamentals

SECM, pioneered by Bard in 1989 [54,55], is an electroanalytical scanning probe technique in which a current response is recorded at an ultramicroelectrode (UME), immersed in an electrolytic solution and positioned or moved in close proximity to a substrate. The potential of the UME is controlled by a bipotentiostat and the current response, caused by the electrochemical reactions at the UME, usually depends on both the topography and electrochemical activity of the surface [29]. The radius of UMEs used in SECM experiments ranges from 25 µm down to several nanometers [64,65]. Due to the small electrode size, UMEs exhibit distinctive and advantageous properties in comparison to macroelectrodes: *i.e.*, small time-constants, low ohmic drops, reduced capacitive current, and enhanced mass transfer [57,66].

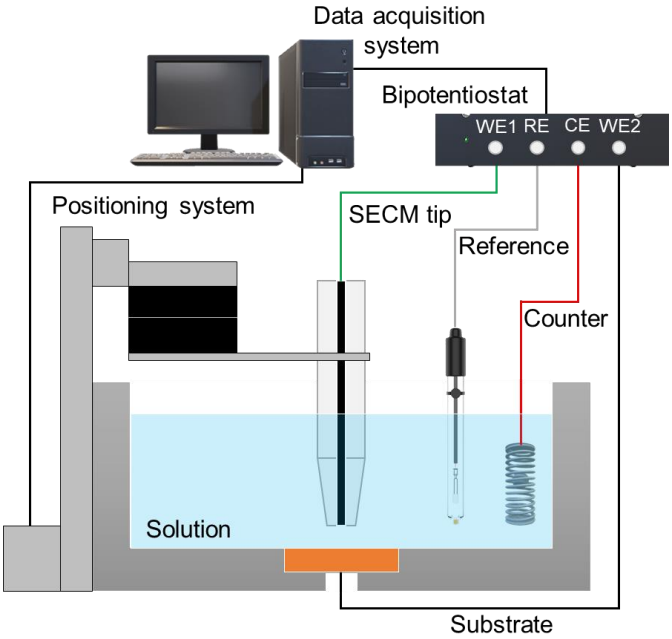

Figure 2.1. Schematic of the SECM instrument.

A schematic of the SECM set-up is depicted in Figure 2.1. The set-up consists of a three- or four-electrode electrochemical cell: the UME, mounted on a xyz positioner and serving as working electrode (WE), the counter-electrode (CE), the reference electrode (RE, usually a quasi-silver/silver chloride electrode) and if needed, the (conductive) sample as a second working electrode. The electrodes are immersed in an electrolyte solution containing a certain concentration, C_O, of electroactive species with fast electron transfer kinetics (also called redox mediator) that ─ in the example shown in Figure 2.1 ─ are present only in their oxidized form (O). When a specific potential is applied to the UME, the electroactive species is reduced ($O + ne^- \rightarrow R$) at the UME, resulting in a current flow.

For a conventional disk-shaped macroelectrode, the current-time relationship is given by the Cottrell equation (equation 2.1) [66]. For disk-shaped UMEs, the current flow is given by the modified Cottrell equation (equation 2.2) with a second term for a time-independent current contribution.

$$i(t) = \frac{nFAD_O^{0.5}C_O}{\pi^{0.5}t^{0.5}} \tag{2.1}$$

$$i(t) = \frac{nFAD_O^{0.5}C_O}{\pi^{0.5}t^{0.5}} + \frac{nFAD_OC_O}{r_0} \tag{2.2}$$

According to equation 2.2, at short times, when the diffusion layer is thin compared to the UME radius, the first term dominates and the current at the UME follows the Cottrell equation, applying semi-infinite linear diffusion, as for conventional macroelectrodes (Figure 2.2a); however, at larger times ($\sim r_0^2/D$, *i.e.*, ns to µs timescales depending on the radius of the nano- or microelectrode [57,67]) when the diffusion layer is thicker than r_0, the first term of equation 2.2 is neglectable and the current at the UME becomes time-independent, *i.e.*, the UME approaches a steady-state regime. The mass transport is dominated by hemispherical diffusion, as shown in Figure 2.2b. Due to the relatively short time in which the UME reaches the steady-state, most of the SECM experiments are performed under steady-state conditions and treated as a steady-state system [57,66]. For a disk-shaped UME far away from the surface (*i.e.*, a few UME radii), the steady-state diffusion-controlled current, i_{ss}, is given by equation 2.3 [66].

$$i_{ss} = 4nFD_OC_or_o \tag{2.3}$$

When the UME (or tip) is moved close to an insulating surface, the steady-state current measured at the UME decreases compared to i_{ss}, due to the physical presence of the substrate that partially hinders the diffusion of the electroactive species toward the UME. The current decrease is a function of the tip-surface distance, d, and this process is referred to as negative feedback (Figure 2.2c) [56,57].

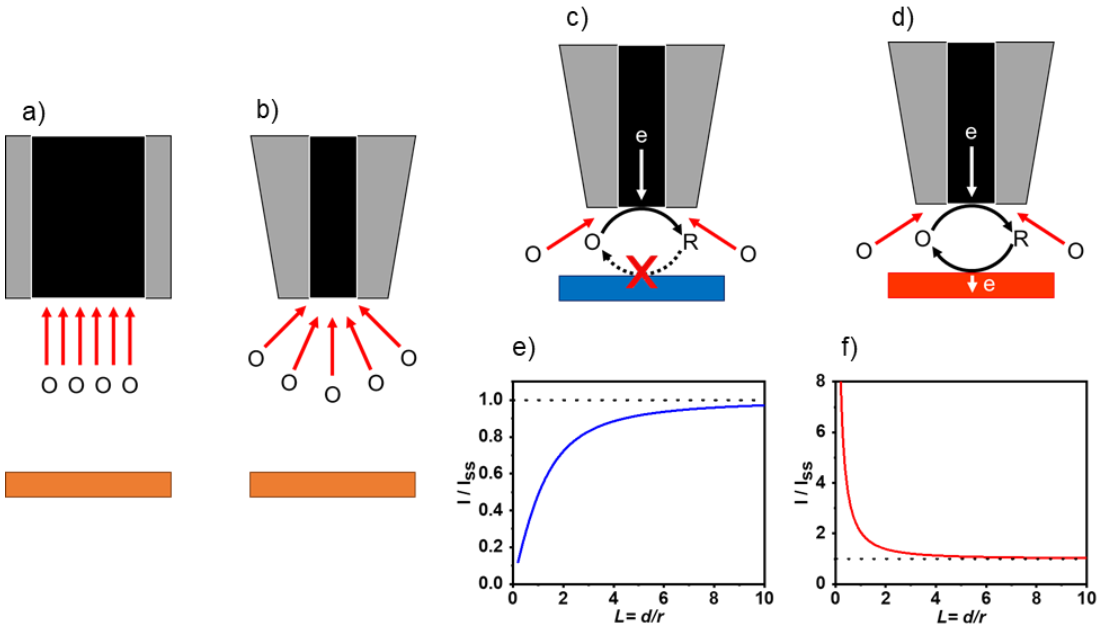

Figure 2.2. Diffusion profiles at (**a**) a macroelectrode (planar diffusion) and (**b**) a microelectrode (hemispherical diffusion). Schemes are not to scale. Schemes of SECM feedback mode for (**c**) insulating samples (negative feedback) and (**d**) conducting samples (positive feedback). Theoretical approach curves for (**e**) insulating samples (negative feedback) and (**f**) conducting samples (positive feedback). The approach curves are derived from equations 2.4 and 2.5, respectively, for a UME with an RG – ratio of the insulating glass sheath radius and the electrode radius – equal to 10.

When the tip approaches a conductive substrate, even though the substrate hinders the diffusion of the electroactive species, the reduced R generated at the UME can be re-oxidized (regenerated). The regeneration of the electroactive species increases the concentration of O in the gap between the tip and sample, which leads to an increased current at the UME, compared with i_{ss}. This process is called positive feedback (Figure 2.2d) [56,57]. The tip current *vs.* the tip-surface distance plot is known as the approach curve and is usually given in a dimensionless form by plotting the normalized current, $I = i/i_{ss}$ *vs.* the normalized tip-substrate distance, $L = d/r$, which is shown for a negative and a positive feedback approach curve in Figure 2.2e and Figure 2.2f, respectively. Pure negative feedback and pure positive feedback approach curves can be calculated with equations 2.4 and 2.5 [68]:

$$I(L) = \frac{1}{k_1 + k_2/L + k_3 \exp\,(k_4/L)} \tag{2.4}$$

$$I(L) = k_1 + k_2/L\ + k_3 \exp\,(k_4/L) \tag{2.5}$$

Where k_1, k_2, k_3 and k_4 are constants that depend on the RG – ratio of the insulating glass sheath radius and the electrode radius – of the tip. The analysis of the $I\ vs\ L$ curves, by fitting the experimental curves with theoretical models, allows (*i*) to obtain quantitative kinetic information of the sample, *e.g.*, to determine the rate constants of the electron transfer for the specific redox species at the surface; (*ii*) to determine the tip-substrate distance, and (*iii*) to characterize the UME, determining, *e.g.*, the RG of the tip. In this work, experimental approach curves were employed to obtain the tip-surface distance using an approximation introduced by Lefrou and Cornut [69] (equation 2.6) for fitting the data.

$$I(L) = \frac{\frac{2.08}{RG^{0.358}}\left(L - \frac{0.147}{RG}\right) + 1.585}{\frac{2.08}{RG^{0.358}}(L + 0.0023RG) + 1.57 + \frac{lnRG}{L} + \frac{2}{\pi RG} ln\left(1 + \frac{\pi RG}{2L}\right)} \quad (2.6)$$

Besides the feedback mode, several other SECM modes have been developed, as shown in Figure 2.3. Since mainly generation/tip collection (SG/TC) mode was used in this thesis, the readers are directed toward excellent reviews, providing detailed information on SECM modes and their applications [56,58].

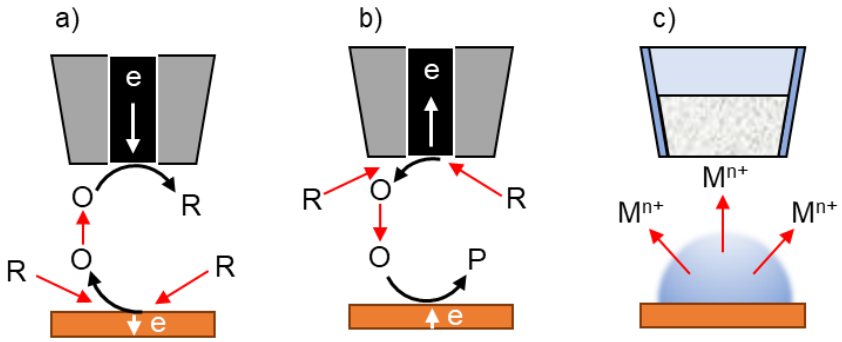

Figure 2.3. Schematic of SECM operational modes. (**a**) Substrate-Generation/Tip-Collection (SG/TC). (**b**) Tip-Generation/Substrate-Collection (TG/SC). (**c**) Potentiometric mode with an ion-selective electrode, where M^{n+} is a cation in solution with charge n.

2.2.2. SG-TC mode combined with anodic stripping voltammetry

Conventionally, in the SG/TC mode, the tip current is used to monitor ("collect") the flux of electroactive species generated at the substrate. In SG/TC mode the tip-substrate distance is usually larger than in SECM feedback mode and, in particular for conductive substrates, the tip-substrate distance must be sufficiently large that no feedback effect is observed, *i.e.,* the products from the reaction at the tip does not react at the surface of the substrate. SG/TC mode has been used to determine concentration profiles of a redox-active species by recording approach curves. Alternatively, the tip is

kept at a fixed distance at a certain position above the substrate and the current response is recorded over time. Using electrochemical techniques, such as anodic stripping voltammetry (ASV) [70], the concentration of the electrochemically active species can be quantitatively determined. Especially metal ions, released from a substate have been determined by SG-TC-ASV. In ASV a pre-electrolysis step is applied, where the analyte (the species in solution or released from a substrate) is electro-deposited and pre-concentrated onto the surface of the UME biased at a cathodic potential. In the following step, the stripping step, the deposited species are anodically re-dissolved applying voltammetric techniques, such as linear sweep voltammetry (LSV), differential-pulse voltammetry (DPV), or square-wave voltammetry (SWV, Figure 2.4) [66,71] that allow the quantitative determination of the analyte.

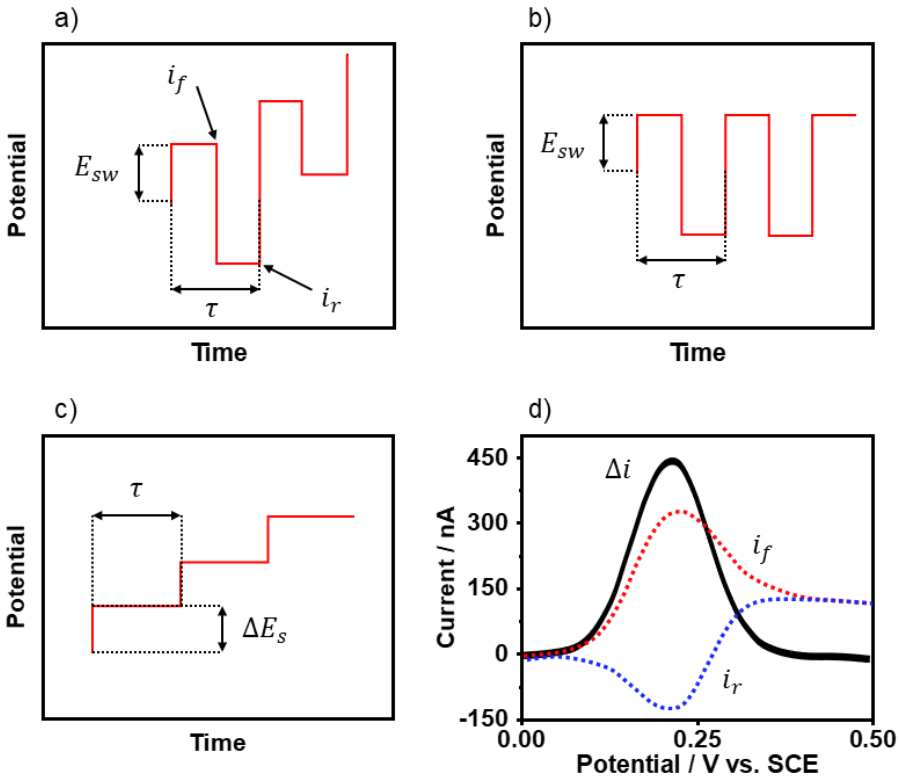

Figure 2.4. (**a**) Square-wave waveform formed by the superimposition of a (**b**) symmetric square wave on a (**c**) base staircase potential. E_{SW} and ΔE_s determine the amplitude of the square-wave and the potential step of the staircase potential, respectively, τ is the square-wave period, i_f and i_r are the forward and the reverse currents, respectively. The arrows highlight the time when the forward and backward current is recorded. (**d**) Square-wave voltammogram (black line) of the oxidation of 20 mmol L^{-1} $K_4Fe(CN)_6$ in 2.0 mol L^{-1} KNO_3 recorded at a Pt UME with a radius of 13 µm. The dotted lines represent the forward current (red) and the reverse current (blue). [Adapted from reference [75] ref with permission of Elsevier Science].

Compared to voltammetric sweep techniques that do not require pre-concentration steps, ASV in combination with voltammetric step techniques is highly sensitive, allowing the quantification of low concentrations (down to 10^{-11} mol L^{-1}) due to the pre-concentration of the analyte [71].

Up to date, most SECM experiments performed on bacterial samples and antimicrobial surfaces have mostly employed the combination of ASV and LSV to monitor the silver(I) ion efflux from living cells [72] or the silver(I) ion release from NPs immobilized at a polymeric surface [70,73], by positioning the SECM tip in close proximity to the sample. Alternatively, SWV is used due to the excellent sensitivity (*i.e.,* an enhanced current signal), fast analysis, and the suppression of no-faradaic background current, a known drawback in linear and cyclic voltammetry [66,71,74]. The enhanced current signal of SWV arises from the intrinsic characteristics of the technique since the excitation signal in SWV (Figure 2.4a) is obtained by the superimposition of a waveform composed of a symmetric square wave (Figure 2.4b) on a base staircase potential (Figure 2.4c). Under these conditions, in each cycle, the analyte is oxidized in the forward pulse and reduced during the reverse pulse. Thus, in each cycle, the current response is recorded twice: once shortly before the end of the forward pulse (cathodic current, i_f) and once shortly before the end of the reverse pulse (anodic current, i_r). The difference in current responses ($\Delta i = i_f - i_r$) is plotted *vs*. the base staircase potential, giving a peak-shaped voltammogram symmetrically positioned at the half-wave potential. The peak current is proportional to the concentration of the analyte [66,71,74]. Figure 2.4d shows an exemplary representation of the voltammogram recorded on a Pt UME, highlighting the forward (red dotted line), reverse (blue dotted line), and net current (black line), for the oxidation of 20 mmol L^{-1} $K_4Fe(CN)_6$ in 2.0 mol L^{-1} KNO_3 [75].

2.3. Scanning Electrochemical Cell Microscopy

2.3.1. Fundamentals

SECCM [59,60] belongs to the family of electrochemical SPM techniques and it is based on the scanning droplet cells, which intrinsic principle is the micro- and nano-confinement of the electrochemical cell. SECCM has been so far employed for spatially resolved surface investigations of conductive and semi-conductive substrates with application in different fields, in particular corrosion-related research [76] and catalytic materials [77]. The SECCM set up [60] is shown in Figure 2.5a. The SECCM probe consists of a single- or dual-barrel nano- or micro-pipette filled with an electrolyte solution and a quasi-reference counter electrode(s) (QRCE) that is (are) inserted into the barrel(s).

The probe is mounted on a z piezoelectric positioner and is moved in the normal direction to the surface (mounted on a x, y positioner) until contact occurs through a meniscus formed between the orifice of the pipette and the sample. The parameters used to position the pipette and to ensure the formation of the meniscus depend on whether a single-barrel (Figure 2.5b) or a double-barrel (Figure 2.5c) pipette is used. When using single-barrel pipettes, a potential is applied between the QRCE and the sample, and the current response of the sample is monitored during the approach of the pipette.

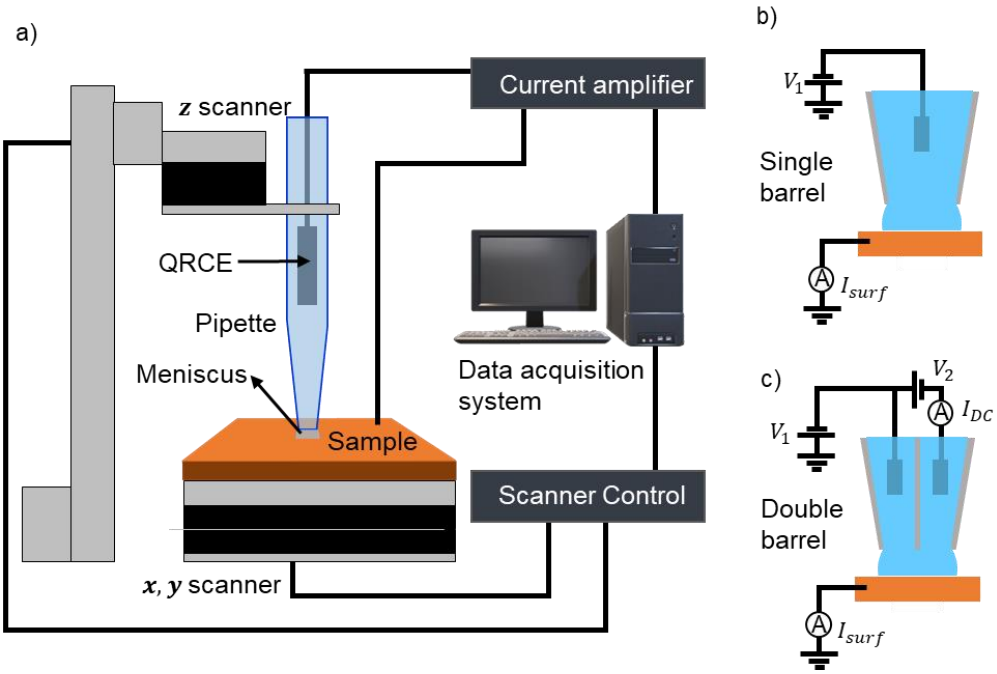

Figure 2.5. (**a**) Schematic of the SECCM instrumentation. Detail of (**b**) single-barrel pipette and (**c**) double-barrel pipette. Abbreviations: V_1 applied potential, V_2 potential applied between the QRCEs, I_{DC} induced ion current, I_{surf} current of the sample surface.

As depicted in Figure 2.6, when the single-barrel pipette is in air, *i.e.*, the meniscus is not formed, the current response is zero, while, upon droplet contact with the surface, a change in current reveals the formation of the meniscus. Since the current of the sample is used as feedback signal to detect the formation of the meniscus, one important limitation of the single-barrel pipettes is that the sample must be (semi)conductive. When using double-barrel pipettes (Figure 2.5c), a potential bias is applied between the QRCEs in the two barrels (V_2) and the induced ionic current (I_{DC}) across the droplet at the end of the pipette is monitored. Once the meniscus is formed, the droplet morphology changes, and a change in I_{DC} occurs. Using double-barrel pipettes, any material (conductive or insulating) can be investigated [59,77]. Independently on the feedback used for monitoring the meniscus formation, once contact is established, a confined

electrochemical cell is formed where the (conductive) sample serves as a working electrode, and electrochemical measurements can be performed (*e.g.*, chronoamperometry, cyclic voltammetry, etc.), by varying the potential of the QRCE(s). Due to the nano- or micro-sized area probed at the working electrode, SECCM benefits from the characteristic of the UMEs (described in **Section 2.2**), such as radial diffusion and efficient mass transport. After the electrochemical measurements are performed in one location, the pipette can be retracted and approached in another area of the sample and further measurements can be performed resulting in sets of data for statistical analysis. The movement of the sample in the x, y plane is controlled by the piezoelectric positioner; thus, the distance of each investigated spot (hopping distance) can be controlled at the nano-scale level [59,77].

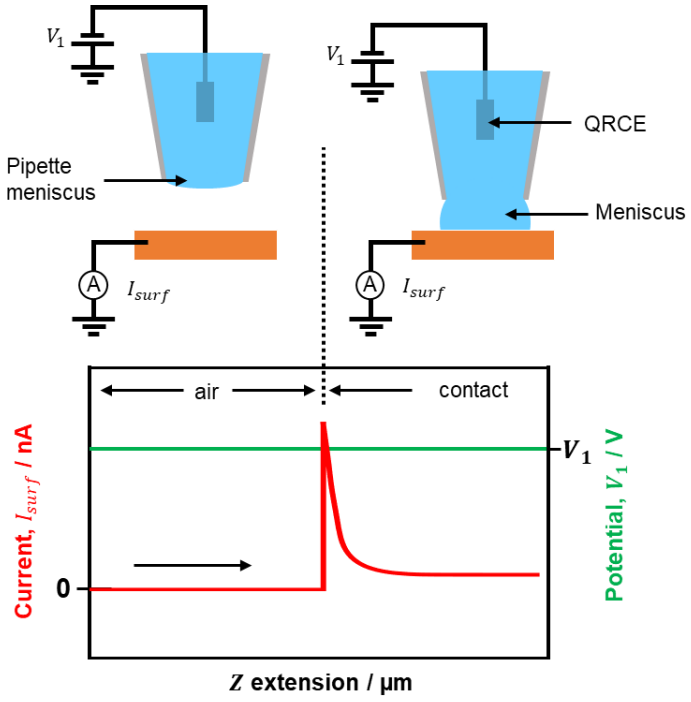

Figure 2.6. Schematic of an approach curve of a SECCM single-barrel pipette and respective current response before and after the pipette-sample contact. Three parts are identified: in air, where the pipette meniscus has not yet established contact with the sample, the jump-to-contact (dotted line), and the contact regime, where a droplet is formed between the pipet and the sample.

Even though SECCM was originally designed to investigate the electrochemical activity of a variety of materials with high resolution [60,76,78,79], recent works have focused attention on employing SECCM to modify different samples with nano- and micro-sized patterns and structures [80,81]. The species that should be deposited can be dissolved in the electrolyte solution of the pipette and arrays of deposited spots can be

obtained by approaching the pipette at different locations with a determined hopping distance. The surface modification can be conducted by chemical modification of the spot, *i.e.,* by maintaining the pipette in contact with the surface during a certain time to favor the the deposition due to solvent evaporation [80], or by performing electro-deposition experiments [81], as it will be discussed in **Chapter 4** of this thesis.

2.4. Atomic Force Microscopy

2.4.1. Fundamentals

AFM was introduced in 1986 by Binnig, Quate, and Gerber [26]. In contrast to the STM, almost all types of samples, without the limitation of the conductivity of the material, can be investigated. Experiments can be performed not only in high vacuum and ambient environment but also in liquids, *e.g.,* in buffered solutions [82,83]. Since its introduction, AFM has become a routine technique to characterize a wide range of materials with nano- and sub-nanoscale resolution, in terms of morphology, roughness, and inter- and intra-molecular forces [62,63,84–86]. Indeed, up to date more than 110.000-AFM-related articles have been published (Clarivate *Web of Science*, Copyright Clarivate 2022), revealing the multitude of applications of AFM and AFM-based techniques, ranging from polymer science, mechanobiology, semiconductors, and corrosion science [87–91].

A schematic illustration of the AFM setup is shown in Figure 2.7.

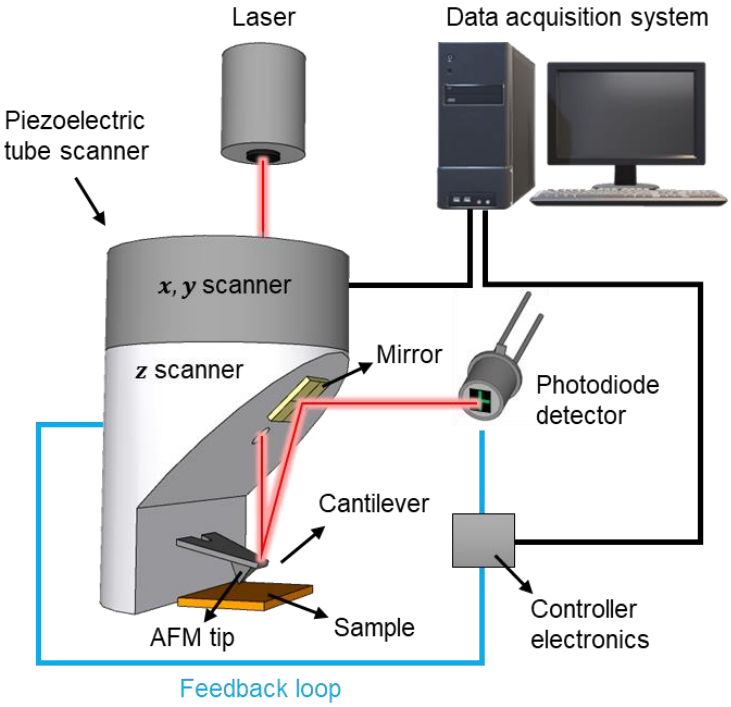

Figure 2.7. Schematic of the AFM instrumentation.

The fundamental of an AFM measurement arises from long- and short-range interaction forces between the sample and the AFM probe, which consists of a sharp tip or a colloidal probe located at the apex of a flexible cantilever. During scanning, the cantilever bends vertically upwards or downwards due to the repulsive or attractive interactions with the sample. This deformation of the cantilever (deflection) is typically detected by a laser beam (red line in Figure 2.7) focused on the backside of the cantilever and directed to a position-sensitive 4-segmented photodiode detector. The forces experimented by the AFM probe can be approximated by the Lennard-Jones potential curve (Figure 2.8a), with principally three different AFM imaging modes (Figure 2.8b-d): contact mode, non-contact mode, and intermittent mode. The last two modes are known as AFM dynamic modes.

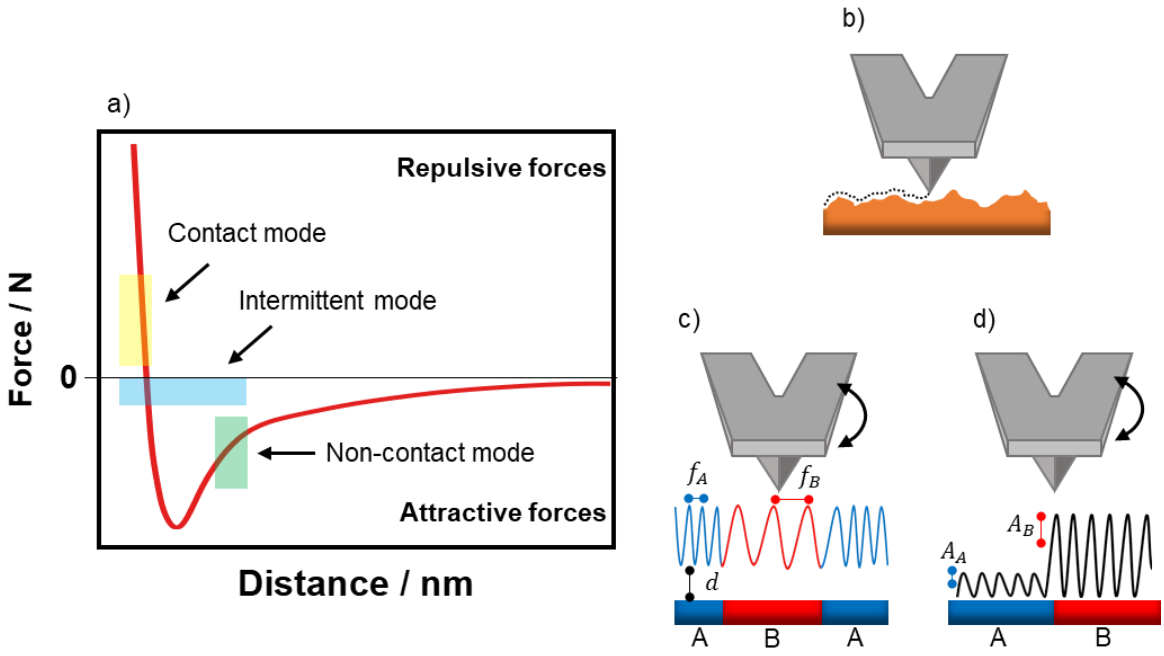

Figure 2.8. (**a**) Simplified Lennard-Jones potential curve highlighting the force regimes for the different AFM operational modes. Schematics of the AFM operational mode: (**d**) contact mode, (**c**) non-contact mode, also known as frequency modulation, FM-AFM, and (**d**) intermittent mode, also known as amplitude modulation, AM- AFM. f_A and f_B denote the frequency of the probe in dependence of the material (material A and B), recorded in FM-AFM mode, d is the AFM probe-surface distance; A_A and A_B denote the amplitude of the probe recorded for material A and B, respectively, in AM -AFM mode.

Contact mode (Figure 2.8b). At short distances (up to 10 nm), the AFM probe manly experiences repulsive interatomic forces that can be short-range Born forces (~ 0.1 nm) or long-range Van der Waals forces. At very small distances (~ 1.0 Å), the

probe is subjected to Pauli repulsion, which arises from the overlapping of the electron orbitals of the tip and the sample. In this case, where repulsive forces are predominant, the AFM probe and the sample are considered to be in "contact", *i.e.*, the AFM operational mode is in the contact regime. Two different approaches exist when operating in contact mode: (i) constant height and (ii) constant force. In constant height mode, the tip-sample distance is kept constant and the deflection of the cantilever is directly recorded and used to determine the topographical data. This mode can usually only be employed for atomically flat samples since topographical features can lead to damage of the AFM probe or sample. In constant force mode, the deflection, *i.e.*, the force[a] of the cantilever, is held constant at a fixed value (set-point) through an electronic z feedback system determining the actual difference of the deflection signal with the setpoint value, which is frequently called the error signal. When the cantilever bends due to changes in morphology or tip-surface interactions, and thus the deflection value changes, the error signal (voltage) is applied to the piezo scanner through the z feedback system (controller) to re-adjust the height of the piezo scanner to maintain the set-point. The topographical image is then generated from the z-motion of the scanner.

Non-contact mode (Figure 2.8c). In non-contact mode, also called frequency modulation, FM-AFM, attractive interactions are predominant. In FM-AFM, the cantilever is located a short distance above the sample surface and is driven to the oscillation at its resonance frequency. The frequency feedback system is employed to maintain a constant amplitude. In FM-AFM constant amplitude mode, a second feedback loop ensures that the amplitude of the cantilever is kept constant, these detected changes in amplitude can also be recorded and a complementary image showing only the non-conservative forces is acquired [92]. Traditionally, FM-AFM has been employed for studies under ultra-high vacuum (UHV) conditions, achieving atomic resolution. Q-factors of the cantilever, a parameter related to the force sensitivity of the cantilever, greater than 10^4 is required [92,93], hence quartz tuning forks due to their high stiffness are employed. The operation of FM-AFM in liquid environments has been a challenge since the motion of the cantilever is highly damped due to the viscosity of the medium, which leads to a decrease of the Q-factor down to 20-30 [94]. However, recently, significant advances have been achieved in FM-AFM operated in liquids [95–97]. Even though the low Q-factor results in a reduced force sensitivity, real atomic resolution has been achieved [94].

[a] In AFM contact mode, at small deflection values, the cantilever can be considered as a Hookean spring with an associated spring constant, k. In these conditions, the cantilever obeys Hook´s law that describes a proportional relationship between the deflection, D and the force, F: $F = -kD$.

Intermittent mode (Figure 2.8d). The intermittent mode [98–100], also known as amplitude modulation, AM-AFM, was first introduced in 1993 by Zhong et al. [101] and differs from the contact mode AFM and FM-AFM, since the oscillating cantilever gently strikes the surface, minimizing the friction and lateral forces. In AM-AFM, the cantilever is, thus, driven at a fixed frequency slightly below its free resonance frequency, and the variation of the amplitude oscillation and/or the phase shift of oscillation is detected by a lock-in amplifier resulting in amplitude and phase images [102]. The amplitude oscillation, usually set in the range of 1 to 100 nm, is used as a feedback signal to measure the topography of the sample. The amplitude is compared to the set-point and the difference in amplitude is used to adjust the tip-sample distance (z–piezo), for topographical information. For phase images, the phase lag of the tip is recorded while the amplitude is kept fixed by the feedback system. Since the phase shift is closely related to the dissipation energy during the tip-sample contact, phase images give qualitative information related to the variation in the properties of the scanned material (*i.e.*, adhesion, elasticity, viscoelasticity) [103]. For instance, AM-AFM mode has been used to investigate polymeric and copolymeric substrates and, while the topographical images did not reveal any particular feature in the polymeric surface, the contrast obtained in the phase images revealed the organization and crystalline phases of the copolymer [104].

As in FM-AFM, the resolution in AM-AFM is limited by the damping of the cantilever during its oscillation and the Q-factor varies, to 200–600 in air, and 1–20 in liquid [103].

2.4.2. AFM force spectroscopy

When the AFM probe is approached and retracted to/from a fixed point of a sample, the deflection of the cantilever, *i.e.*, the forces experienced by the tip, can be monitored as a function of the tip-sample distance, resulting in so-called force-distance (FD) curves. This static AFM mode is called AFM force spectroscopy (FS) [86], and a schematic of a characteristic FD curve is depicted in Figure 2.9. When the tip is retracted at a distance of a few micrometers from the surface, the cantilever is not deflected due to the absence of the interaction between the tip and the sample (position A in Figure 2.9). As the tip starts to approach the surface, long- and short-range forces, such as van der Waals forces and capillary forces pull on the tip towards the sample. Once the total force gradient that acts on the tip exceeds the value of the spring constant of the cantilever, the tip jumps into contact with the sample (jump-to-contact, position B in Figure 2.9) [105,106]. If the distance is further decreased after the jump-to-contact point, the repulsive interaction between the tip and the sample increases due to the Pauli repulsion (position C

in Figure 2.9). During the retraction, the repulsive forces decrease again, however, the interactions between the tip and sample during the contact cause the tip to adhere to the sample, and the cantilever to band downward (adhesion hysteresis, position D in Figure 2.9). When the spring constant of the cantilever overcomes the adhesion forces, the tip experiences the “snap off” and the cantilever returns to its original position (again position A in Figure 2.9). By fitting the FD curves to an appropriate model, various properties of the sample, such as Young´s modulus, adhesion, dissipation energy, and surface charge density can be quantitatively evaluated. Usually, the nanomechanical properties measured by AFM are explained in terms of continuum mechanics models [86,107–109]; it is assumed that the total interaction force has conservative (elastic), F_{con} and non-conservative (dissipative), F_{dis} contributions (*i.e.*, $F = F_{con} + F_{dis}$). While conservative forces are correlated to the elastic energy stored in the deformation of the material, the non-conservative forces are related to the energy dissipated through viscous losses, rupture of molecular bonds, and surface adhesion hysteresis. To investigate surface charge density properties, continuum surface models are employed, where the surface charge is assumed to be uniformly distributed across the surface [110].

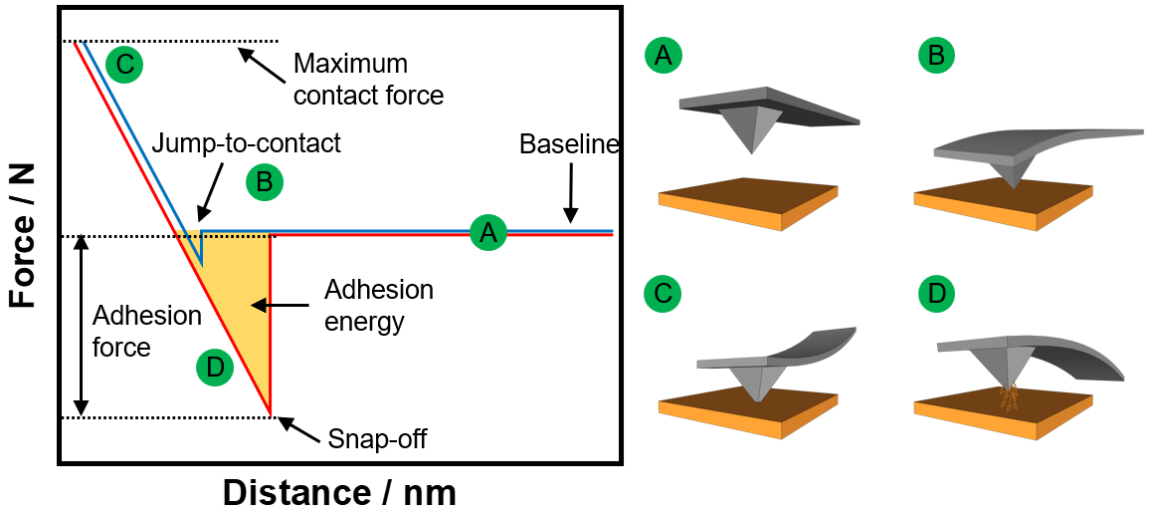

Figure 2.9. Illustration of an AFM force-distance curve, highlighting the non-contact position of the cantilever (position A), the jump-to-contact with the tip indentation (position B), the maximum contact force with high repulsive interactions (position C), and the retraction where adhesion forces produce adhesion hysteresis (position D).

Elasticity, adhesion, and surface charge density have been investigated for different samples described in this thesis, thus the evaluation and interpretation of these parameters will be explained in more detail in the following.

Elasticity. Elasticity is a property of materials that can be described by Hooke's law in terms of stress and strain, in which the stress is the ratio of the applied force, F, to a cross-section area, A_0, and the strain expresses the amount of deformation. The ratio of the stress to the strain gives a constant, the elastic modulus, that depends on the investigated material and the type of deformation. Depending on the type of deformation experienced by the material, different elastic moduli can be defined [111]. However, mainly Young´s modulus (E_S) is reported that is defined as the mechanical resistance of the material during the elongation or compression, *i.e.*, the tendency of an object to deform along an axis when opposite forces are applied along the same axis. In AFM-FS experiments, during the approach FD curves, the AFM tip is pushed onto the surface of the sample and the total deformation is the sum of the deformation of the tip and the deformation of the probed sample area (indentation) [63,112]. The approach FD curves can then be employed to derive Young's modulus of the probed sample area. Different indentation models are used, depending on the geometry of the tip. The commonly used indentation model is the Hertzian model [109]. The Hertz theory, shown in equation 2.7, assumes that (*i*) the tip is a rigid sphere with radius r, (*ii*) the modulus of the tip is higher than the modulus of the surface, and (*iii*) neither adhesion nor visco-elasticity is present. A more accurate model is the Derjaguin-Muller-Toporov (DMT) model [107] (equation 2.8), in which long large attractive forces (*i.e.*, adhesion properties) are taken into account. The DMT model considers also the retract FD curves, since it substitutes the zero-indentation point of the Hertz model, with the point of maximum adhesion. These models are only valid for "rounded" (tip curvature radius of ~20 nm), colloidal probes and samples with small indentation (*i.e.*, with deformations smaller than the radius of the probe). When sharp tips with radii < 10 nm are used to study hard samples, the Sneddon model [108] (equation 2.9) is usually the more appropriate model since it considers the nano-indenter as a rigid cone truncated into de surface. Like in the Hertz model, adhesion and viscoelastic parameters are neglected.

$$F_{Hertz} = \frac{4}{3}\frac{E_S}{(1-v_s^2)} r^{0.5}\delta^{1.5} \tag{2.7}$$

$$F_{DMT} = \frac{4}{3}\frac{E_S}{(1-v_s^2)} r^{0.5}\delta_m^{1.5} - F_{adh} \tag{2.8}$$

$$F_{Sneddon} = \frac{2}{\pi}\frac{E_S}{(1-v_s^2)} \tan(\alpha)\delta^2 \tag{2.9}$$

E_s is Young's modulus of the sample, v the Poisson ratio[a] of the sample, r the radius of curvature of the tip, δ the indentation, δ_m the indentation at maximum adhesion, $F_{adh}$the adhesion force and α the half-cone opening angle in a sharp triangular tip.

Adhesion. The term adhesion between two objects often appears ambiguous, since the term encompasses generally two processes: (*i*) the formation of interfacial bonds (or interactions) at the interface between two materials that cause their attraction, and (*ii*) the energy required to break the formed bonds. Using an appropriate model for evaluating the FD curves, these two processes can be distinguished and both quantitative and chemically sensitive adhesion properties, as well as thermodynamic parameters related to the surface energy, due to the surface adhesion hysteresis present in every FD curve can be obtained. The surface adhesion hysteresis derives from the concept that the work to separate two surfaces in contact dissipates more energy than bringing two surfaces in contact, *i.e.*, the tip-surface system exhibits different surface energy, γ, during the approach and retraction. The interaction force that includes the term of adhesion is described by the abovementioned DMT theory (equation 2.8), where $F_{adh} = 4\pi r\gamma$. Practically, the adhesion force is obtained by determining the maximum negative force of the retraction FD curve, where a sudden change in deflection occurs. The adhesion energy corresponds to the area between the retraction FD curve and the baseline, as shown in Figure 2.9.

The adhesion forces are a direct consequence of the tip-surface interaction. Indeed, when the AFM-FS experiment is performed in ambient conditions, the most prominent interactions between the tip and the sample are capillary forces and van der Waals interactions [63,113], in contrast to FS in aqueous solutions, where hydrogen bonds, Coulomb forces, and, in some cases, chemical covalent bonds play a significant role [63]. Therefore, relevant chemical information related to functional groups, ionic state, and hydrophobicity of the sample can be evaluated from the FD curves.

Surface charge density. The most common used model that correlates the interaction forces between two surfaces and the surface charge density is the Derjaguin, Landau, Verwey, and Overbeek (DLVO) theory [114]. In case the AFM tip curvature radius is large enough ($r < 20$ nm), the tip-surface system can be considered as a sphere-flat surface system and the DLVO theory can be fitted to the AFM-FS measurements. The DLVO theory takes the attractive van der Waals forces, F_{VdW} and repulsive electrostatic

[a] The Poisson ratio is defined as the ratio of transverse contraction strain to longitudinal extension strain in the direction of stretching force. For biological and soft samples, it is usually assumed to be 0.5 (perfect rubber), while metals and stiffer surfaces exhibit a Poisson ration in the range of 0.31-0.35.

forces, F_{EDL} into account, and short-range interactions such as hydration forces are neglected ($F = F_{VdW} + F_{EDL}$). The dependency of the van der Waals forces with the tip-surface distance is shown in equation 2.10, where the tip is assumed to exhibit a conical shape with a curvature radius, r [63,115].

$$F_{\mathrm{VdW}}(d) = -\frac{2A_H r^2}{3(2r+d)^2 d^2} \tag{2.10}$$

Where d is the tip-surface distance and A_H the Hamaker constant, a parameter that depends on the physico-chemical properties of the system. Typical values of A_H of condensed matter in water are about 10^{-20} J [116].

Electrostatic forces arise from the generation of the so-called electrical double layer (EDL). Every surface immersed in a liquid exhibits an EDL, due to the redistribution of the ions close to the surface. When two surfaces approach each other, the EDLs are perturbed, and a force that depends on two contributions is generated, which is explained in terms of disjoining pressure (equation 2.11). The first repulsive contribution is the osmotic pressure force, which arises from the fact that the concentration of ions in the gap between the surfaces is higher than the concentration in the region outside the gap (first term in equation 2.11). The second attractive contribution is produced by the actual electrostatic force generated by the charged particles (second term in equation 2.11).

$$\Pi_{EDL}(d) = -\frac{\varepsilon\varepsilon_0}{2}\left(\frac{d^2}{dd^2}\psi(d)\right) + k_B T\rho(d) \tag{2.11}$$

$$F_{EDL} = \frac{2\pi r\lambda_D}{\varepsilon\varepsilon_0}\left[2\sigma_S\sigma_T \exp\left(-\frac{d}{\lambda_D}\right) + (\sigma_S^2 + \sigma_T^2)\exp\left(-\frac{2d}{\lambda_D}\right)\right] \tag{2.12}$$

The solution of equation 2.11 can be derived by using the continuum theory within the DLVO model, in which first the potential distribution is calculated by solving the Poisson-Boltzmann equation (PBE), and secondly, the potential is correlated to the surface charge density, following the Gouy-Chapman model [117–119]. The final expression that correlates the electrostatic force with the tip-surface distance is shown in equation 2.12, where σ_S and σ_T are the surface charge density of the sample and the AFM tip, respectively. By fitting equation 2.12 to the approach FD curves, it is possible to obtain the surface charge density of the sample taking following assumptions into account: (*i*) the surface potential must be lower than 50-80 mV (Debye-Hückel approximation) [120,121], (*ii*) the surface charge of the AFM tip and the sample remain constant during the approach (constant charge approximation) [63,122,123], and (*iii*) the equation is valid provided that the tip-surface distance is larger than two times the Debye length [63].

3 ANTIBIOFOULING: THE ROLE OF THE SURFACE CHARGE DENSITY

3.1. Biofouling and surface charge density: why is it important?

The capability of bacteria to attach to a surface and form biofilms gives rise to biofouling problems for a wide range of scenarios, including pipelines, ship hulls in marine transport, biomedical devices, and even water purification plants (*e.g.*, membrane filtration systems) [124]. For instance, it has been estimated that *ca*. US$56 million is the annual cost associated with hull biofouling only for the US Navy´s ships cleaning [125] and US$150 billion per year for the marine transportation business to overcome biofouling-related drawbacks, such as transport delays, maintenance, and hulls' repair [126]. Biofouling control encompasses several strategies to avoid bacteria proliferation and can be classified into five groups:

1. *Chemical*: which consists either of the application of biocides to control the development of biofilms (*e.g.*, chlorines, aldehydes, or isothiazolinone) or of surface modification strategies using antimicrobial polymers.
2. *Physical*: either *via* ultrasonic wave treatments or manual cleaning (*e.g.*, wiping and brushing).
3. *Biological*: though the application of enzymes or bacteriophages.

4. *Electrochemical*: *via* applying an electrical field to tailor the surface activity and particle charge to produce a hostile environment at the surface.
5. *Nutrient limitation*: with the aid of organic carbon and phosphates using filtration and ion exchange methods.

Independently on the type of strategy used to overcome the biological fouling, one of the main goals of research in fighting biofouling is the formulation of permanent antibiofouling materials based on the self-cleaning of surfaces. Thus, the trend has been driven toward polymeric-based coatings [126] and superhydrophobic surfaces [127–129]. Recently, also amphiphilic and hydrophilic polymers have emerged as a new approach to mitigate the adhesion of microorganisms [130,131].

But one of the main questions that has to be addressed is: *what is the function of surface charge density in bacterial adhesion and why is it important to develop efficient antibiofouling materials*?

It is well known that gram-positive and gram-negative bacteria carry a net negative charge in their envelope surface, due to the presence of teichoic acids, membrane proteins, and negatively charged phospholipids [132]. Thus, the surface charge of the antibiofouling coatings plays a significant role in the first contact between the bacterial cell and the surface. The surface charge density of a surface arises from the ionization (or dissociation) of chemical functional groups present in the structure of the surface or by the adsorption of ions from the solution [133]. In metallic and semiconductive materials, the surface charge density depends also on the electrode potential [66]. The adsorption and rearrangement of ions and solvent molecules at the solid-liquid interface give rise to a region close to the surface, the EDL [133,134]. The EDL is usually described by the mean-field description of the Gouy-Chapman-Stern model, depicted in Figure 3.1a, which combines the Helmholtz model and the Gouy-Chapman model. In the Helmholtz model, the EDL is treated like a parallel-plate capacitor (Helmholtz or Stern layer), in which one plate is the charged interface and the second plate corresponds to the center of the nearest hydrated ions (outer Helmholtz layer, OHP). In this model, the specifically absorbed species are neglected and described in the refined Grahame´s model [135] as the inner Helmholtz plane (IHP). Accordingly, the potential between the two plates decreases linearly. By combining the Helmholtz model with the Gouy-Champann model, which defines the presence of a diffuse electrified layer, the potential decays exponentially, moving away from the surface, and is described by the Poisson-Boltzmann equation [136]. The diffuse layer is mathematically defined by the Debye length (λ_D) equation 3.1.

$$\lambda_D = \left(\frac{\varepsilon \varepsilon_0 k_B T}{\sum_{j=1}^{N} c_j^0 q_j^0} \right)^{0.5} \quad (3.1)$$

Where ε and ε_0 are the relative dielectric constant and the vacuum permittivity, respectively, k_B is the Boltzmann constant, T the absolute temperature, c_j^0 and q_j^0 are the bulk concentration and charge of the species j, and N is the number of charged species.

Methods to measure surface charges can be classified into two general groups: (*i*) bulk methods, such as titration, electrochemical impedance spectroscopy, and electrokinetic techniques, which provide information on the averaged surface charge density without considering the charge heterogeneities, *e.g.*, between particles, and (*ii*) localized methods, using SPM techniques, such as scanning ion conductance microscopy (SICM) [137] and AFM to determine the local surface charge and possible heterogeneities in surface charge distributions [110]. Since the research of this thesis (and this chapter) have been focused on the determination of surface charge density using AFM (described in detail in **Chapter 2**), the reader is directed to other reviews focused on the surface charge density analysis using SICM [79,110,138].

The principle of AFM for surface charge analysis is depicted in Figure 3.1b.

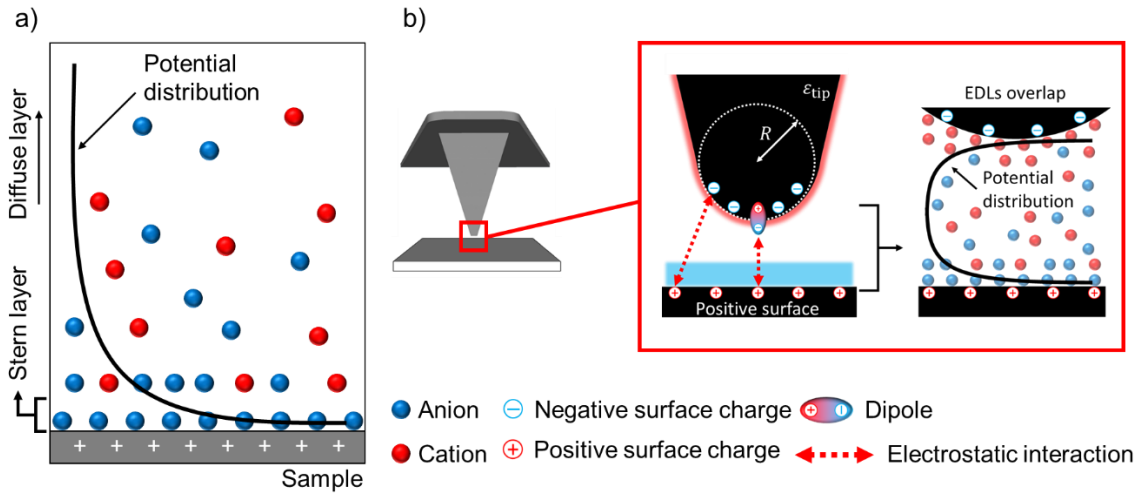

Figure 3.1. (**a**) Schematic of the Gouy-Chapman-Stern model EDL at a positively charged surface. (**b**) Representation of the surface charge measurement using AFM. This method is based on the overlapping of AFM tip and surface EDLs. Panel adapted with permission from the Annual Review of Analytical Chemistry, Volume 15 © 2022 by Annual Reviews, reference [110].

The surface charge density is an important factor that must be considered when formulating a new antibiofouling material since the charge depends not only on the structural characteristic of the material but also on the medium surrounding the surface. The surface charge of a substrate can be tailored *via* different strategies [128,139,140]:

(*i*) electrochemically, by applying a certain potential, in case the surface is conductive (Figure 3.2a), (*ii*) *via* chemical functionalization to create a net negative surface charge to increase the repulsive electrostatic interactions and avoid bacteria attachment (*repelling surfaces* or *passive biofouling,* Figure 3.2b) [140], or (*iii*) *via* chemical functionalization by covalently linking biocidal positive groups [139], *i.e.*, quaternary ammonium compounds that can interact with the cell envelope *via* electrostatic interactions and penetrate the cell ("*killing" surfaces* or *active biofouling,* Figure 3.2c) [141].

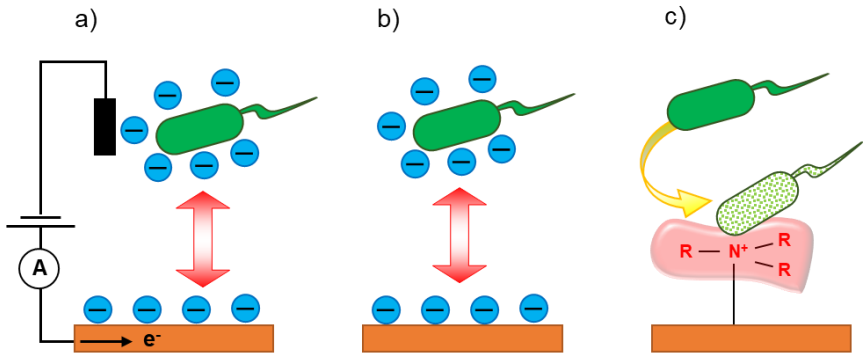

Figure 3.2. Strategies for tailoring the surface charge density of a substrate. (**a**) Electrochemical approach. (**b**) Functionalization with negative groups (passive biofouling). (**c**) Functionalization with biocide groups (active biofouling).

Over the last decades, a plethora of new antibiofouling materials has been developed, following the above-mentioned routes. Within the course of this thesis, the research focus was on polydopamine (PDA), a functional polymer, mainly obtained *via* self-oxidation of dopamine (dip-coating) in presence of *i.e.,* oxygen, which is often referred to as a synthetic analog of naturally formed melanin [142]. PDA not only exhibits antibiofouling properties due to the presence of amine and catechol moieties [143–145], but it is also a suitable platform for the incorporation of organic and inorganic active biofouling agents [142,146–148]. Furthermore, the mechanical, electrical, and chemical properties of PDA, *i.e.*, adhesion properties, surface charge, and presence of functional groups, highly depend on, and can be tailored by, the deposition method and the experimental conditions. For instance, it has been shown that the point of zero charge (PZC) of PDA films obtained by dip-coating can vary from 4.0 to 6.0, depending on the experimental conditions and the buffer used during the polymerization. The PZC of PDA and its influence on bacterial attachment is one of the main objectives of this work, which is described in this chapter.

An overview of the deposition methods of PDA and their implication on the structure of the polymer are described in the following, as background information for the discussion and conclusion of the work described in **Section 3.3**.

3.2. Polydopamine: a versatile, biocompatible polymer

PDA is a mussel-inspired biocompatible polymer, known to be a product of the self-oxidation of dopamine. The self-polymerization of dopamine was first investigated in 1970 by Swan et al. [149] revealing the presence of indole, pyrrole, and dopamine sub-units in the obtained polymeric film. However, the interest in PDA increased exponentially after the work of Lee et al. [150], where the authors showed the versatility of PDA to adhere to almost every type of surface. They also reported reproducible deposition of PDA films *via* dip-coating in basic (pH 8.5) dopamine solutions. Even though coating materials with PDA based on the dopamine auto-oxidation approach has been widely used to modify a plethora of surfaces, including Teflon-based materials, it has been observed that during the formation of the polymeric film on the surface, heterogeneous black particles in solution are also formed [142]. An alternative strategy to selectively deposit PDA is *via* electrochemical methods in buffered (pH 7.0 – 7.5) oxygen-free dopamine solutions, using either cyclic voltammetry or pulsed-deposition [151–154]. Recently, it has been shown that electrochemical pulsed-deposition leads to excellent control of the polymeric thickness and allows tuning of the oxidation state of PDA, by applying a constant cathodic or anodic potential after the deposition for a certain period of time [153,154]. Furthermore, AFM force spectroscopy studies revealed that the oxidized form of PDA exhibits higher adhesion than the reduced form, and PDA immersed in alkaline solutions (pH 10) presents stronger adhesion forces than when in acidic solutions (pH 3) [154]. Thus, the nature of the functional groups of PDA plays a pivotal role in the nanomechanical properties of the polymer.

Mechanistic studies related to the formation of PDA have been reported mostly for PDA obtained *via* dip-coating [155,156]. Within this thesis, the focus is on the electro-polymerization. The electro-polymerization of dopamine to form PDA films follows an electrochemical-chemical-electrochemical (ECE) pathway [151,157]. The generally accepted route is depicted in Figure 3.3 [151,157,158]. Namely, dopamine is electro-oxidized to dopamine-quinone (DAQ) in a two-electron, two-proton reaction that converts the o-phenolic group of dopamine to quinone groups [159,160]. The consecutive intramolecular cyclization of DAQ *via* 1,4-Michael addition leads to the formation of leucodopaminechrome (LDAC) [151,160]. Recently, a second pathway – during the electrochemical deposition of PDA – has been suggested, in which the Michael cyclization after the first oxidation step of dopamine does not take place. Indeed, oxidative degradation of indole-based species of DAQ can occur, resulting in open-chains amines [158,159]. This pathway is in accordance with the observation of a small number of

pyrrole-carboxyl groups in the PDA structure that was observed *via* X-ray photoelectron spectroscopy [159].

After the formation of LDAC *via* Michael addition, the final electrochemical step leads to the formation of dopaminechrome (DAC). Further polymerization and interactions of DAC and intermediate structures lead to the final melanin-like polymer [151,157,158].

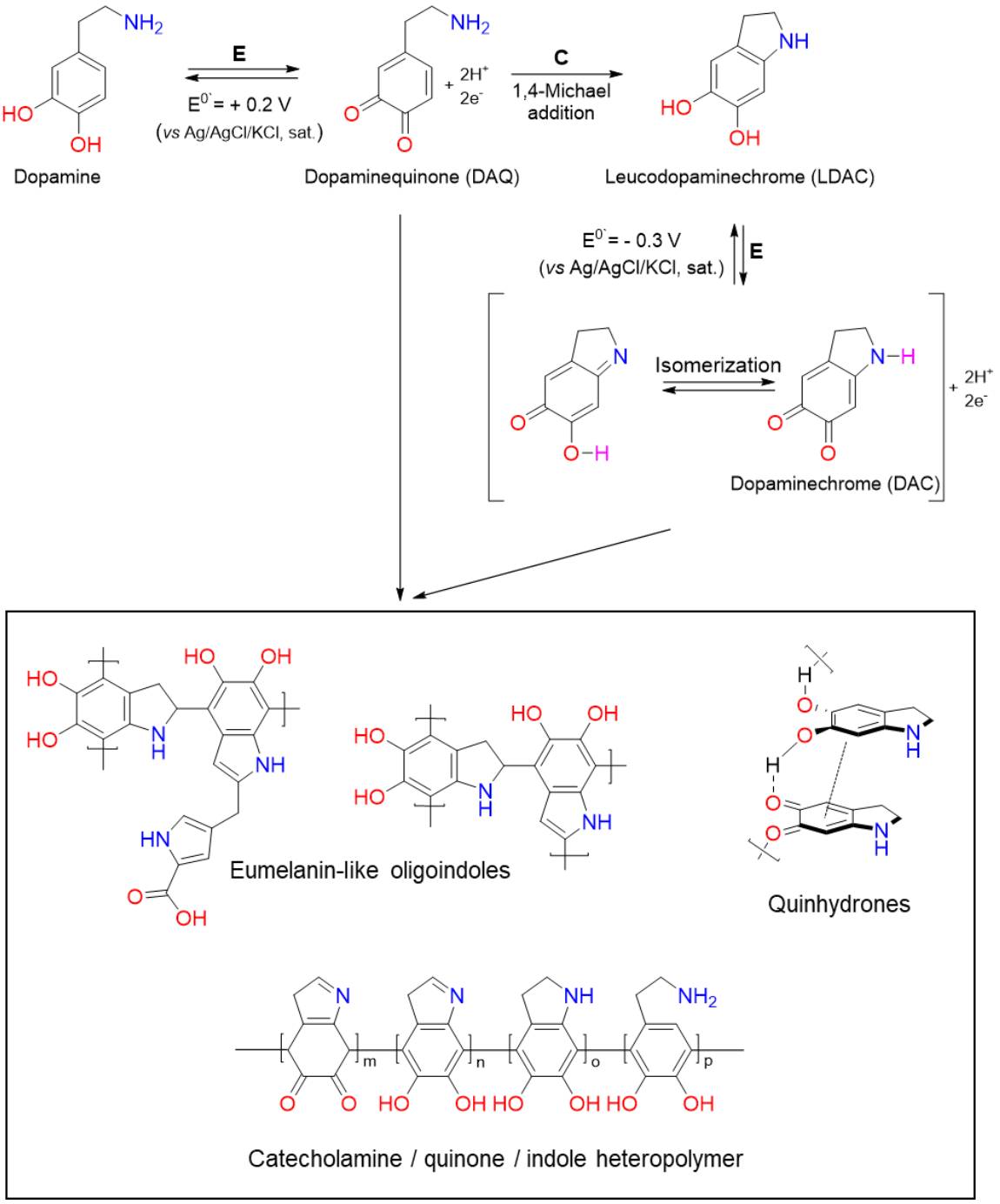

Figure 3.3. Proposed mechanistic pathways for the electro-polymerization of dopamine and final polymeric products. "**E**" denotes an electrochemical reaction and "**C**" is a chemical reaction.

3.3. Atomic force microscopy and infrared spectroscopic studies on the role of surface charge for the anti-biofouling properties of polydopamine films

Parts of this section have been already published and are reprinted from the following article: **Caniglia, G**.; Teuber, A.; Barth, H.; Mizaikoff, B.; Kranz, C., Atomic force and infrared spectroscopic studies on the role of surface charge for the anti-biofouling properties of polydopamine films. *Analytical and Bioanalytical Chemistry* (in press, **2022**, doi: 10.1007/s00216-022-04431-7). Copyright © 2022, Springer Nature.

Declaration of contribution: Giada Caniglia and Andrea Teuber: conceptualization, data curation, writing-review, and editing. Holger Barth: resources. Boris Mizaikoff and Christine Kranz: supervision-review and editing. The AFM and AFM force spectroscopy studies have been performed by Giada Caniglia. The ATR-FTIR studies have been performed by Andrea Teuber.

3.3.1. Introduction

Biofouling is generally an undesirable process generated by the colonization of microorganisms that affect several fields, from medical devices to marine and industrial systems [124,161]. Different strategies are nowadays used to overcome this problem, such as the mechanical removal of biofilms or the implementation of antibiofouling and antimicrobial agents [161], such as superhydrophobic surfaces, the application of chemical agents (*e.g.*, furanone-derivative [124]) and surface modification with antimicrobial polymers [141]. The latter has gained interest since they can inhibit bacterial colonization or eradicate biofilms with greater efficiency in comparison with their monomeric counterparts [141]. Their efficiency arises from the presence of biocidal functional groups, such as tertiary amines, quaternary nitrogen groups, and catechol groups. PDA can be classified as an antibiofouling agent. Indeed, it has been demonstrated recently that, due to the presence of catechol and amine functional groups, PDA can lead to the generation of reactive oxygen species and exhibit promising antimicrobial activity [143,162].

Up to date, there are two main strategies to produce thin PDA films: (*i*) by dip-coating, exploiting the self-polymerization of dopamine in basic solutions [150,155], and (*ii*) *via* electrochemical methods, like cyclic voltammetry [164,165] and pulsed-deposition [153,154,166,167]. In comparison to chemical methods and other electrochemical approaches, the electro-deposition of PDA *via* pulsed methods (e-PDA) has shown excellent reproducibility in terms of homogeneity, thickness, and oxidation state of the

polymer [154]. Despite this, the chemical and mechanical properties of PDA and e-PDA have been extensively studied [151,152,164,168,169], however, the interaction of bacteria with e-PDA and its antibiofouling properties have been still poorly investigated [152,167,170,171].

It is well known that the early stages of bacterial adhesion can be controlled partially by the surface charge of the polymer to which they are attached. Previous works demonstrated that the surface charge density of dip-coated PDA can be modified by varying the pH and ionic strength of the solution in which the polymer is immersed and that the PZC of PDA strongly depends on the deposition conditions. Indeed, the PZC of PDA dip-coated using Tris-buffer is PZC = 4.00 [172] while the PZC of PDA dip-coated using copper(II) as oxidant is equal to 6.50 [173]. To date, only limited studies have been conducted on the surface charge density of e-PDA and its interactions with bacterial cells.

AFM-based force spectroscopy [84,174–176] and ATR-FTIR [44,173,177–182] have been employed to investigate the early stage of attachment of *E. coli* at pulsed-deposited e-PDA and the influence of the surface charge density of the polymer. Also, since the adhesion properties of e-PDA have shown significant dependency on pH [154], AFM force titration [176] studies have been conducted to determine the dissociation constants (pK_a) of e-PDA.

3.3.2. Results and discussion

3.3.2.1Characterization of e-PDA

The e-PDA samples were obtained by electrochemical pulsed-deposition as shown exemplarily in Figure 3.4a. Since PDA is a non-conductive polymer, a decrease in current is expected with the formation of the polymeric film, which hinders the charge transfers for further oxidation steps of the monomer and oligomers. The insulated nature of PDA can be observed in the drop in current response after the application of 100 pulsed-cycles (Figure 3.4a) and by the cyclic voltammograms depicted in Figure 3.4b in which the decrease in the current of the PDA-modified gold electrode (red line) is clearly visible.

As mentioned in **Section 3.2**, the electro-polymerization of dopamine follows an electrochemical-chemical-electrochemical (ECE) pathway, in which the dopamine first electro-oxidizes to form dopamine-quinone (DAQ) through a two-electron two-proton reaction. The subsequent intramolecular cyclization of DAQ leads to the formation of the 5,6-dihydrocyindoline which is further electro-oxidize to form dopamine-chrome (DAC) [151,157,160].

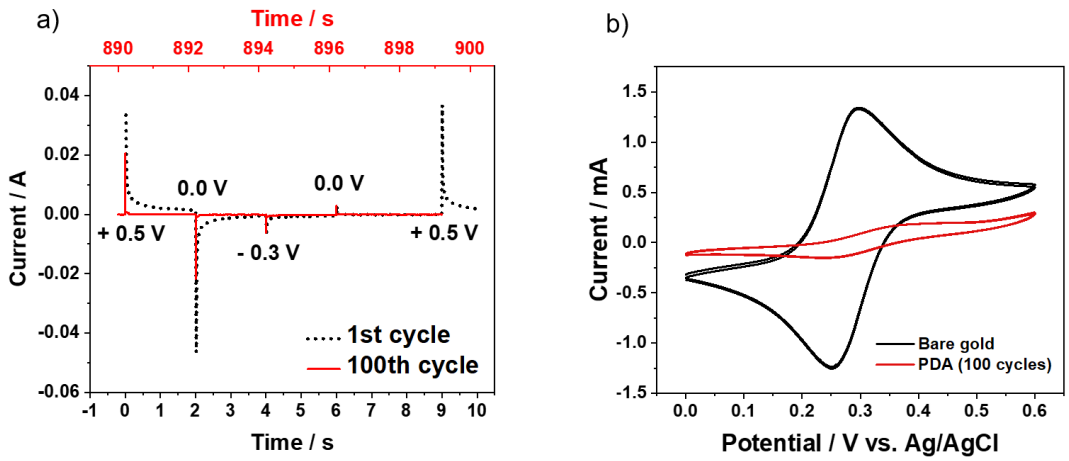

Figure 3.4. (**a**) Chronoamperometric curve during the pulsed-deposition of PDA: first cycle (black) and hundredth cycle (red). (**b**) Cyclic voltammograms were recorded in 5 mmol L^{-1} ferrocene-methanol and 0.1 M KCl before (Au substrate, black) and after e-PDA deposition (100-pulsed cycles, red); scan rate 0.05 V s^{-1}.

The reaction between these species and their intermediate products, including reactive radicals, leads to the formation of a polymeric film characterized by the presence of a plethora of functional groups including o-quinone motifs, pyrrole-carboxyl groups, open-chains amines, amides, and indole-based groups [158,159]. The nature of the e-PDA, however, is still under debate, and to gain a better understanding of the chemistry of e-PDA, force titration studies were performed to obtain the pK values of the surface functional groups of the polymer. Further, the PZC of the e-PDA was locally evaluated using AFM force spectroscopy.

Force titration of e-PDA. In previous studies, it has been demonstrated that the adhesion force of e-PDA is strongly influenced by the pH of the solution in which the polymer is immersed. Kund et al. [154] showed that the e-PDA exhibits high adhesion force at alkaline pH (pH 10) and a pronounced decrease in adhesion was reported in acidic conditions (pH 3). Starting from these findings, a detailed study of the adhesion forces in dependence on the pH value was conducted in the course of this thesis by using force titration. As shown in Figure 3.5, the magnitude of the adhesion force recorded by AFM force spectroscopy is influenced by the ionization state of both the AFM probe and e-PDA surface, and an abrupt change in adhesion at a certain pH can be associated with the dissociation constant, pK, of the polymer.

Since the ionization state of the AFM probe is an important factor that influences the interpretation of the results, the chemical nature of the AFM must be taken into account.

.

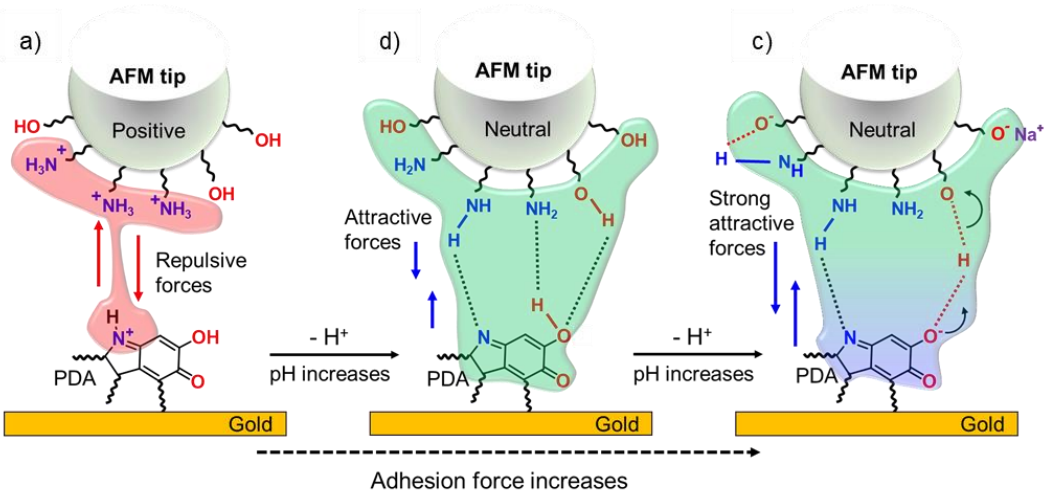

Figure 3.5. Schematics of the interactions between the AFM probe and the e-PDA substrate at (**a**) acidic pH (pH < 6), (**b**) neutral and slightly acidic pH (pH 6 – 7), and (**c**) alkaline pH (pH > 8).

The AFM probe used in this work is made of silicon nitride and when immersed in an aqueous solution the tertiary amide (Si_3N), present at the probe surface, yields amine ($SiNH_2$) and silanol (SiOH) sites, according to equations 3.2 and 3.3 [183].

$$Si_3N + H_2O \leftrightarrows Si_2NH + SiOH \quad (3.2)$$

$$Si_2NH + H_2O \leftrightarrows SiNH_2 + SiOH \quad (3.3)$$

According to the literature [183], both reactions are kinetically very fast, thus the secondary amine ($SiNH_2$) and the silanol (SiOH) species are assumed to be the predominant species at the surface of the AFM tip, and thus, are the responsible for the charge regulation of the AFM tip. Depending on the pH, the interface between the silicon nitride probe and water can be charged due to the dissociation *via* acid-base reactions of the amine and silanol groups. The chemical equilibria are described in the following equations [183–186].

$$SiOH \leftrightarrows -SiO^- + H^+ \quad (3.4)$$

$$SiOH + H^+ \leftrightarrows SiOH_2^+ \quad (3.5)$$

$$SiNH_2 + H^+ \leftrightarrows SiNH_3^+ \quad (3.6)$$

X-ray photoelectron spectroscopy (XPS) studies [187] demonstrated that at low pH (pH < 2) the $SiOH_2^+$ groups (equation 3.5) are predominant, while the formation of SiO^- (equation 3.4) is expected at a slightly alkaline pH (pH > 8). Therefore, in the pH range

investigated here (pH 3 to 10), the surface charge of the silicon nitride AFM probe may be mainly influenced by the equilibria shown in equations 3.4 and 3.6. Thus, the variation in adhesion force can be explained by the attractive and repulsive forces between the AFM tip and the e-PDA surface, that arise from the protonation and deprotonation of the functional groups of both surfaces.

Figure 3.6a shows the force titration curve recorded on the e-PDA surface and Figure 3.6c-d displays representative histograms of the adhesion forces at acidic, neutral, and alkaline pH, respectively.

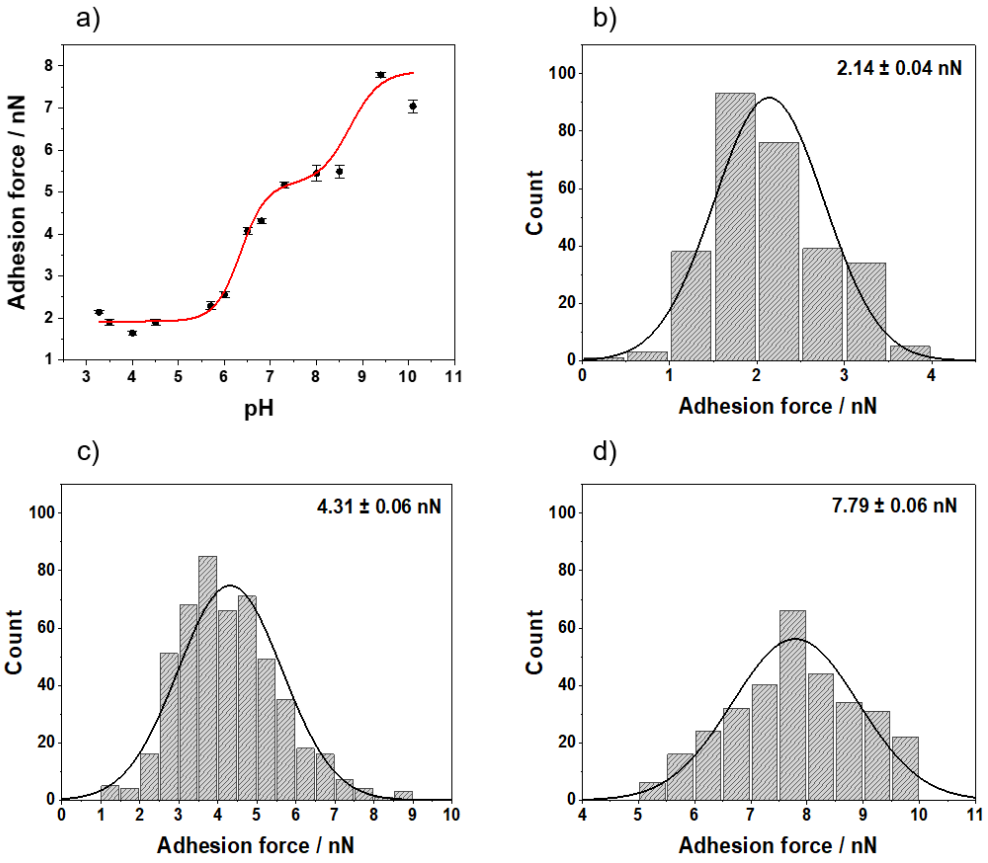

Figure 3.6. (**a**) Force titration curve of e-PDA. Force titrations on e-PDA were performed in MilliQ water with the pH adjusted by adding HCl or NaOH. Histograms of the adhesion forces at (**b**) pH 3.27, (**c**) pH 6.80, and (**d**) pH 9.40 (n = 300).

At acidic pH, low adhesion forces have been observed (2.14 ± 0.04 nN at pH 3.27, n = 300). At pH < 6, the AFM probe is positively charged due to the presence of $-\mathrm{NH}_3^+$ groups and the low adhesion might be due to the electrostatic repulsions between the protonated surface groups of the AFM probe and the e-PDA surface, which is assumed to be positively charged due to the presence of indoline and indole motifs (pK_a ~ 5.5 [144,172]). At pH values close to 6, the adhesion increases significantly (4.31 ± 0.06 nN at pH 6.80, n = 300). At this pH, the amine groups of both surfaces

(AFM probe and e-PDA) start to deprotonate, and the attractive interactions increase, due to the formation, *e.g.*, of hydrogen bonds (Figure 3.5). This variation in interactions is also revealed by the higher dispersion of the adhesion values at a pH between 6 and 7 (broad histogram shown in Figure 3.6c), which may be related to the presence of protonated and deprotonated groups. The pH value, at which an abrupt change in adhesion is observed, represents an approximation of the pK_a of the e-PDA surface functional groups (pK_a = 6.3 ± 0.2, as first inflection point of the double Boltzmann sigmoidal fit in Figure 3.6a). The obtained value of the dissociation constant of e-PDA is in reasonable agreement with the predicted dissociation constants of amine and imine groups present in the polymer, which are $pK_a = 5.8$ (indoline-quinones) and $pK_a = 5.4$ (indole-quinones) [144,172]. A deviation of *ca.* 8.6% from the predicted pK_a values might arise from the presence of deprotonated carboxyl and semiquinone groups of e-PDA ($pK_a = 3.6$ and 4.7, respectively [169]) that increase the interaction (and thus the adhesion force) between the surface groups of the AFM probe and the e-PDA surface. At higher pH values (pH > 8), a second jump of the adhesion values is observed (7.79 ± 0.06 nN at pH 9.40, n = 300) with an inflection point at pH 8.7 ± 0.6. This value can be correlated to a second dissociation constant of the e-PDA, due to the deprotonation of amine groups present in open-chains dopamine-motifs (pK_a = 9.27[a]) and the ionization of the quinone-like functional groups (pK_a = 8.98[a]). A deviation of 4-6% might be due to the reactions that occur at the AFM probe surface, including (*i*) the interaction of the $\mathrm{SiO^-}$ groups with the cations in solution (*i.e.*, $\mathrm{Na^+}$ derived from the NaOH added to the solution) that reduce the concentration of negatively charged silanol groups and (*ii*) the formation of hydrogen bonds between the $\mathrm{SiO^-}$, SiOH and $\mathrm{SiNH_2}$ groups present on the surface of the AFM probe.

Point of zero charge of e-PDA. The surface charge density of the e-PDA was obtained as described in **Section 2.4.2**, *i.e.*, by performing AFM force-distance approach curves and fitting them to equation 3.7. This equation is valid under the following conditions: (*i*) the AFM probe has a radius equal to or larger than 20 nm, (*ii*) the surface charge of the probe and the sample remains constant during the approach of the AFM probe (*constant charge condition*), and (*iii*) the major force contributions arise from the electrostatic interactions, neglecting van der Waals forces since the probe-surface system was studied at a distance greater than the Debye length [114,188,189].

$$F_{EDL} = \frac{2\pi r \lambda_D}{\varepsilon \varepsilon_0}\left[2\sigma_S \sigma_T \exp\left(-\frac{d}{\lambda_D}\right) + (\sigma_S^2 + \sigma_T^2)\exp\left(-\frac{2d}{\lambda_D}\right)\right] \quad (3.7)$$

[a] Dissociation constants have been obtained using the pK_a predictor, MarvinSuite - Fermium v. 5 (20.8.5) by ChemAxon (https://www.chemaxon.com).

The values of the surface charge density of the AFM probe, σ_T, have been taken from previous works [190], performed under the same experimental conditions, *i.e.*, using a silicon nitride AFM probe and adjusting the pH with HCl and KOH solutions. Figure 3.7a-c show representative force-distance curves (dotted lines) recorded on e-PDA at different pH values and the corresponding fitting curves (red lines), obtained using the surface charge density of the sample (e-PDA), σ_S, as fitting parameter from equation 3.7. The fitting analysis was performed by limiting the fit to a probe-surface distance equal to 5 nm (dotted blue line) to minimize the influence of strong repulsive short-range forces such as hydration forces, which act at distances lower than 2-3 nm [85].

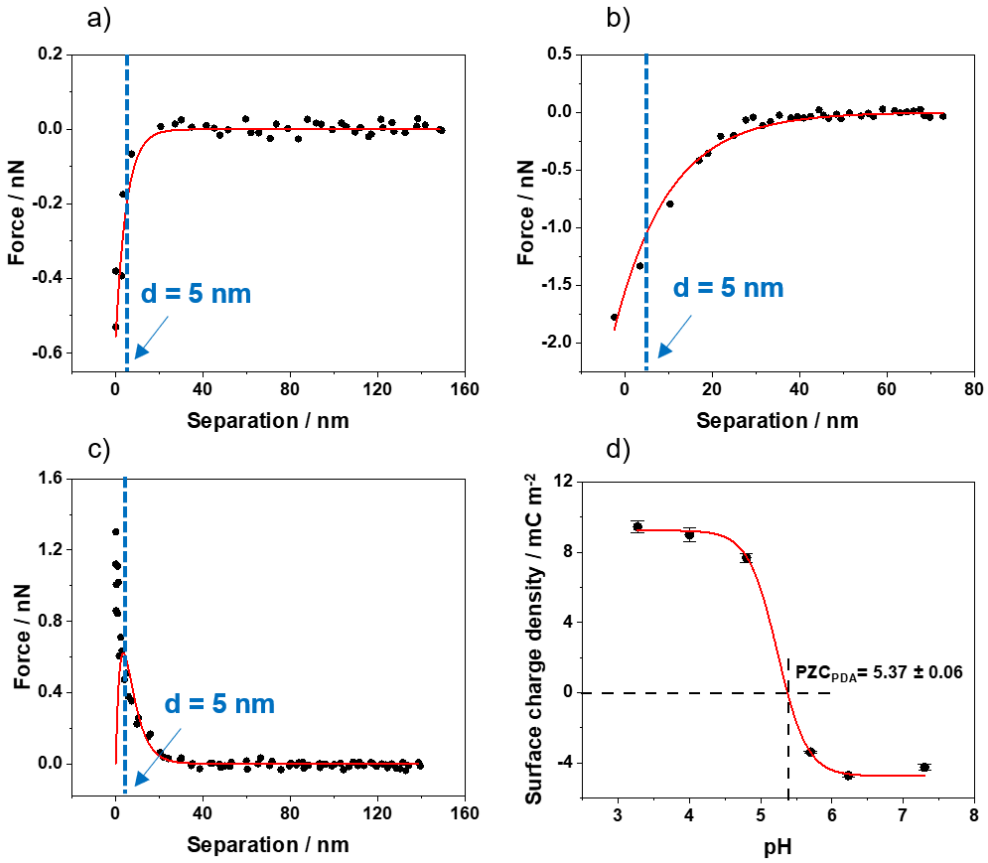

Figure 3.7. Fitting of force-distance curves assuming constant charge conditions at (**a**) pH 3.27, (**b**) pH 4.80, and (**c**) pH 7.30. (**d**) Effect of the pH on the surface charge density of e-PDA at 25°C. Fitting parameters: curvature radius of the AFM probe r = 20 nm, surface charge of the AFM probe -0.010 C m^{-2} < σ_T < +0.015 C m^{-2} [190], Debye length 10^{-7} m < λ_D < 10^{-9} m depending on the pH. For each pH value, 20 approach curves were used to obtain the surface charge density.

Figure 3.7d shows the pH-dependency of the surface charge density of e-PDA resulting from the fitting of 20 force-distance approach curves at each pH level. The PZC obtained was equal to 5.37 ± 0.06, which fits quite well with the previous results obtained by force titration and the expected ionic state of the functional groups of e-PDA. Indeed,

at pH below the PZC, the predominant species are protonated indole and indoline groups responsible for the positive charge of the e-PDA surface. It is worth mentioning that the decrease in surface charge density at pH higher than 4.0, might arise from the contribution of negatively charged carboxylate groups, whose pK_a is equal to 3.6 that may be formed during the electro-deposition of PDA [159,169].

3.3.2.2Antibiofouling properties of e-PDA

Once the PZC of e-PDA was evaluated, the influence of the surface charge on the biofouling activity of the polymer was investigated against *E. coli*. To this end, e-PDA samples were inoculated with *E. coli* cultures at their exponential phase (concentration of 10^8 CFU mL^{-1}) in LB medium at three different pH values. Extreme pH has been excluded to avoid bacterial stress; thus, the selected pH values were pH 5 where e-PDA is positively charged, pH 5.5 where e-PDA is considered neutral, and pH 7.0 where e-PDA is negatively charged.

After 16 h of incubation, the inoculated samples were studied *via* AFM imaging. As shown in Figure 3.8, the density and morphology of bacteria grown at different pH do not show any significant difference.

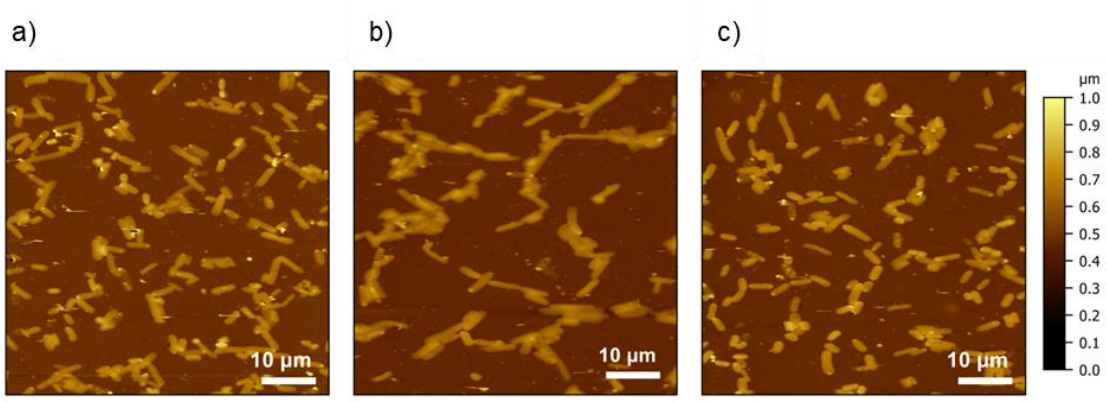

Figure 3.8. Contact mode AFM topography images recorded in air of E. coli grown on (**a**) negatively charged PDA, (**b**) neutral PDA, and (**c**) positively charged PDA.

Even though, force spectroscopy and ATR-FTIR studies showed a strong influence of the surface charge density of e-PDA on bacterial attachment.

As shown in Figure 3.9a, *E. coli* grown on positive e-PDA (pH 5) exhibits an adhesion force equal to 11.6 ± 0.5 nN, while the cell adhesion drops down to 4.2 ± 0.6 nN when e-PDA is neutral (pH 5.5 ~ PZC). These values are consistent with the composition of the bacterial surface, which exhibits a net negative charge due to the presence of lipopolysaccharides that contain negatively charged groups such as phosphates and carboxylates [191,192]. Hence the interaction of *E. coli* with a positive surface, such as e-

PDA at pH 5, is expected to be higher due to electrostatic attraction between the two surfaces. The difference in adhesion can also be observed from the force-distance curves depicted in Figure 3.9b. Interestingly, the adhesion of *E. coli* is similar for neutral and negative e-PDA (Figure 3.9a, green and blue bars), even though a decrease for negative e-PDA surfaces was expected. This similarity in adhesion forces might be due to the contribution of other attractive forces between the bacteria and the e-PDA, for example, while the electrostatic repulsions between *E. coli* and negatively charged e-PDA prevent bacterial attachment, hydrophobic interactions might overcome the repulsive forces, promoting the bacterial adhesion.

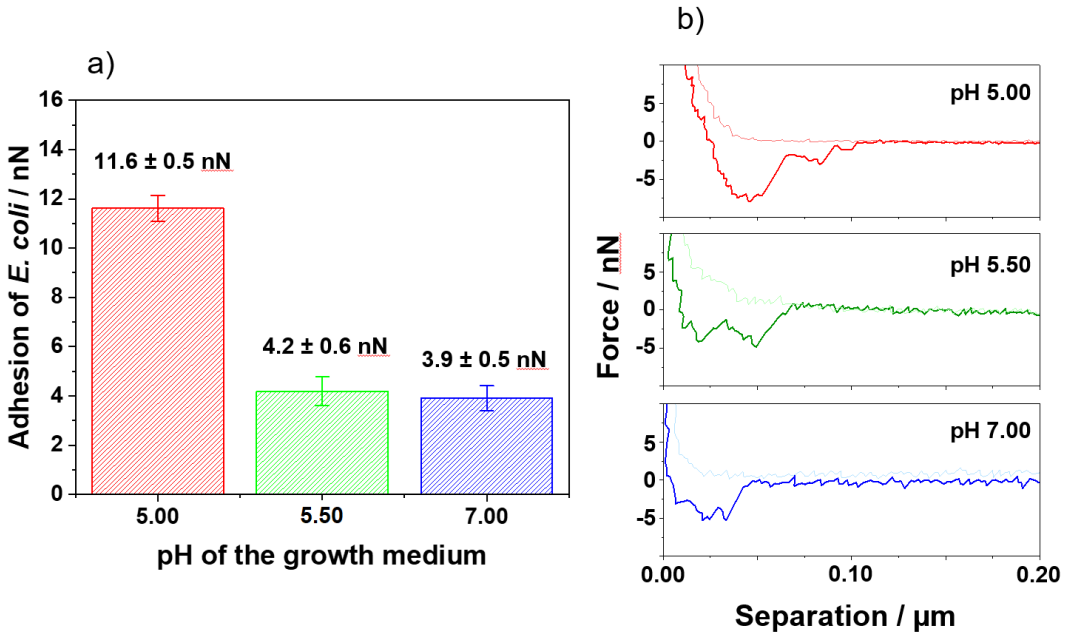

Figure 3.9. (a) Bar chart of the measured adhesion forces of *E. coli* grown on e-PDA at different pH values (error bars reflect the measurements of at least 4 cells and 300 force curves). (b) Exemplary force curves recorded in solution on *E. coli* grown at pH 5.00 (positive e-PDA, red curve), pH 5.50 (neutral e-PDA, green line), and pH 7.00 (negative e-PDA, blue line).

Similar bacterial behavior has been observed in the ATR-FTIR studies. The IR spectra depicted in Figure 3.10 shows a qualitative comparison of the formation of bacterial biofilms at each e-PDA surface. Three different spectral regions were evaluated: (*i*) the amide I band in the range of 1750 – 1600 cm^{-1}, (*ii*) the amide II band in the range of 1600 – 1500 cm^{-1}, and (*iii*) the EPS[a] bands in the range of 1140 – 1000 cm^{-1}.

Amide I and amide II bands reflect, respectively, the C=O vibration and out-of-phase N-H and C-N vibrations, which are characteristic of α-helix and β-sheet protein

[a] The EPS band is also known as the „biofilm indicator band" since it reflects the presence of polysaccharides secreted by the bacteria during the formation of a biofilm [323].

conformations present in the bacterial cell membrane. Hence, the appearance of these two bands is indicative of the presence of bacteria. The spectra shown in Figure 3.10, reveal that on positive (red line) and neutral (green line) e-PDA samples, bacteria were present apparent *via* the presence of both amide I and amide II bands. On the negative e-PDA (blue line), the amide II band is absent, whereas amine I and EPS bands are still clearly visible. The decrease or absence of the amide bands without variations in the EPS band has been already reported, as a consequence of the loss of bacterial proteins due to a hostile environment [44], which can be correlated to a bacteria detachment from the surface.

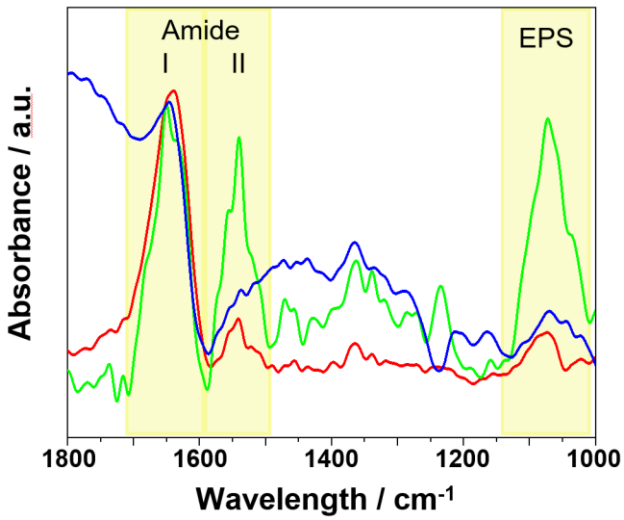

Figure 3.10. ATR-FTIR spectra of *E. coli* biofilms grown at positively (red), neutral (green), and negatively (blue) charged e-PDA films.

The formation of a biofilm, and thus the appearance of the EPS bands at the negative e-PDA surface might be favored by hydrophobic interactions between the cells and the surface, as shown in the AFM force measurements. However, the electrostatic repulsions, a consequence of the negatively charged polymer, may favor an early detachment of the bacterial cells from the surface and thus a decrease of the amide II band [193].

3.3.3. Conclusions

The application of AFM force spectroscopy and force titration gave for the first time insight into the relation of the adhesion of pulsed-deposited e-PDA in dependence of the pH that follows a double Boltzmann sigmoidal relationship. Derived from these measurements, the acidic dissociation constants of the polymer have been derived. The first dissociation constant (pK_a = 6.3 ± 0.2) is in accordance with the generally accepted

structure of e-PDA that considers the presence of indole-quinone and indoline-quinone functional groups, whose pK_a is approx. 5.5. The second dissociation constant (pK_a = 8.7 ± 0.6) is correlated to the amine groups of open-chain dopamine residues and the ionization of quinone-like functional groups, whose dissociation constants are pK_a = 9.27 and pK_a = 8.98, respectively. The surface charge density of e-PDA has been also evaluated using AFM force spectroscopy using the DLVO theory. The PZC was found to be equal to 5.37 ± 0.06. Finally, the antibiofouling properties of e-PDA have been investigated against *E. coli*, using AFM force spectroscopy and ATR-FTIR. *E. coli* grown on positively charged e-PDA exhibit higher adhesion in comparison to bacteria grown on neutral and negatively charged e-PDA. The spectroscopic studies suggest a more pronounced proliferation of bacteria at the positively charged polymer surface.

4 SILVER NANOPARTICLES: A WEAPON AGAINST BACTERIA

Ionic silver has been known for its antibacterial and antiseptic properties for centuries and there is anecdotal evidence for the use of silver formulations for medical purposes already in ancient Egypt and Rome [194]. Nano-silver as an agent for pharmaceutical applications, however, started over 120 years ago, when in 1889 M.C. Lea reported the synthesis of citrate-stabilized colloids [195] that were used as active biocide in medical products named *Collargol*. Nowadays 53% of biocidal silver products contain AgNPs as the active agent [196,197], including products for topical treatment, such as AgNPs-based gels for treating burn wounds; for medical applications, like bone implants and vascular catheters; personal care products and domestic products, such as air purifiers and food storage containers [198].

This chapter gives an introduction to the antimicrobial mechanisms of AgNPs, their method of synthesis (**Section 4.1**), and the experimental results obtained throughout this thesis, with respect to the antimicrobial properties of two different AgNPs formulations (**Section 4.2** and **Section 4.3**).

4.1. AgNPs: synthesis and antimicrobial mechanisms

4.1.1. Synthesis of AgNPs

The biocide activity of AgNPs is influenced by different factors including surface chemistry, shape and size distribution, morphology, presence of capping agents, dissolution rate, and efficiency in ion release [199]. These physicochemical properties determine the bioavailability [200] and the therapeutic effect of the AgNPs since these properties affect the cellular uptake and the penetration of the NPs into biological barriers, such as the bacterial cell membrane [201]. Therefore, the fabrication of the AgNPs is an important step that must be optimized to obtain controlled nanostructures, uniform in size, morphology, and functionalities.

There are two strategies to synthesize AgNPs, and in general for the fabrication of nanomaterials: the *top-down* approach and the *bottom-up* approach (Figure 4.1) [202–204]. The *top-down* method involves the breaking down of bulk material into nanosized structures/objects without atomic-level control, and the subsequent stabilization of the NPs using, *e.g.*, colloidal agents or polymeric matrices. The most common *top-down* techniques include mechanical milling [205,206], thermal or laser ablation [207], and ion-beam sputtering [208].

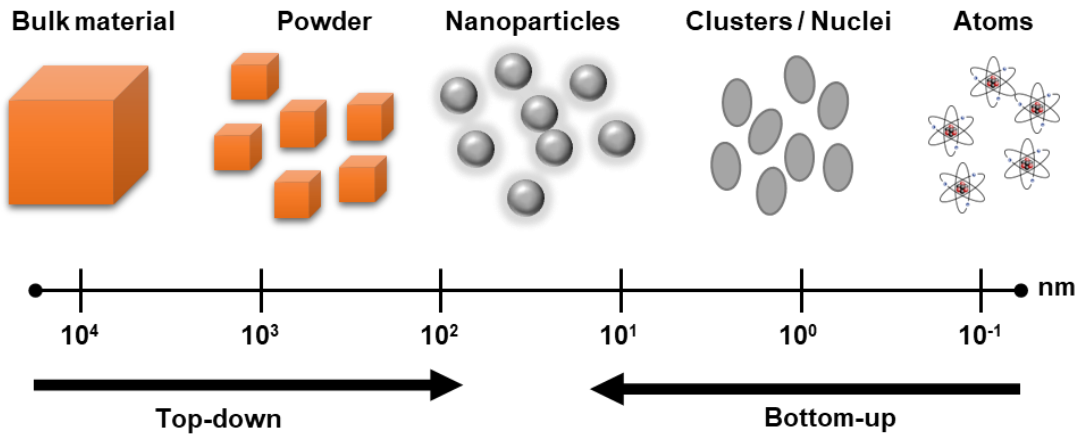

Figure 4.1. Schematics of the *top-down* and *bottom-up* processes for the synthesis of nanomaterials.

In *bottom-up* methods, the atoms are self-assembled to form nuclei which grow into nanosized particles. The forces driving the formation and growth of nuclei are either chemically [209–213], biologically [214–217], or electrochemically [218] driven. Chemical methods consist of the chemical reduction of the metal precursor (usually silver(I) ions in a soluble salt form) using reducing agents (commonly, citrate, ethylene glycol, and

borohydride) and the subsequent stabilization of the NPs using capping agents (*e.g.*, polyvinylpyrrolidone, PVP) [209,219,220]. Biological methods involve the intracellular biosynthesis of AgNPs: the precursor (usually $AgNO_3$ in its ionic form) penetrates the bacterial cell and the catalytic reduction of silver(I) to metallic silver takes place due to the presence of nitrate ions that activate the NADH-dependent nitrate reductase system. The catalytic activation of this system promotes the oxidation of NADH to NAD^+ and the electrons generated are utilized to reduce the silver(I) [215]. The electrochemical routes for the synthesis of AgNPs are usually performed from electrolytic $AgNO_3$ solution and consist of the electrochemical reduction of silver(I) to generate metallic AgNPs. The most important method used is cyclic voltammetry [221], but also galvanostatic methods [222], and double-potentiostatic methods [223,224] are employed.

The *top-down* ion-beam sputtering technique and the *bottom-up* electrochemical double-potentiostatic pulse approach have been used for the preparation of the AgNPs substrates investigated in **Sections 4.2** and **4.3**, respectively, thus in the following, the two approaches are described in more detail.

Ion-beam sputtering of NPs. Ion beam sputtering (IBS) is a non-thermal vaporization process that uses an ion source to sputter or deposit a target material (metallic or dielectric) onto a substrate to form thin films or nanostructures [225]. The typical configuration of an IBS system consists of a vacuum system with an ion source (ion gun), the target material, and the substrate, however more complex configurations may also include a second gridded ion source (Figure 4.2) to provide ion-assisted deposition or a second target material to generate co-deposited composites (as employed in the work presented in **Section 4.2**).

When a high voltage (2-10 kV) is applied to the ion gun, an electrostatic field is generated inside the ion source and electrons are confined in the center of the ion gun. Argon gas is then injected to the ion source and ionized by the high electric field. The argon ions are accelerated to the exit aperture of the ion gun, and a collimated ion beam is produced. The resulting ion beam strikes the surface of the target material(s) and atomic-sized particles are ejected and sputtered onto the substrate [226,227].

Due to the operational mode of IBS, it is possible to control the deposition of the ejected atoms to the substrate, therefore, the nucleation and growth processes of the nanoparticle can be controlled and tuned.

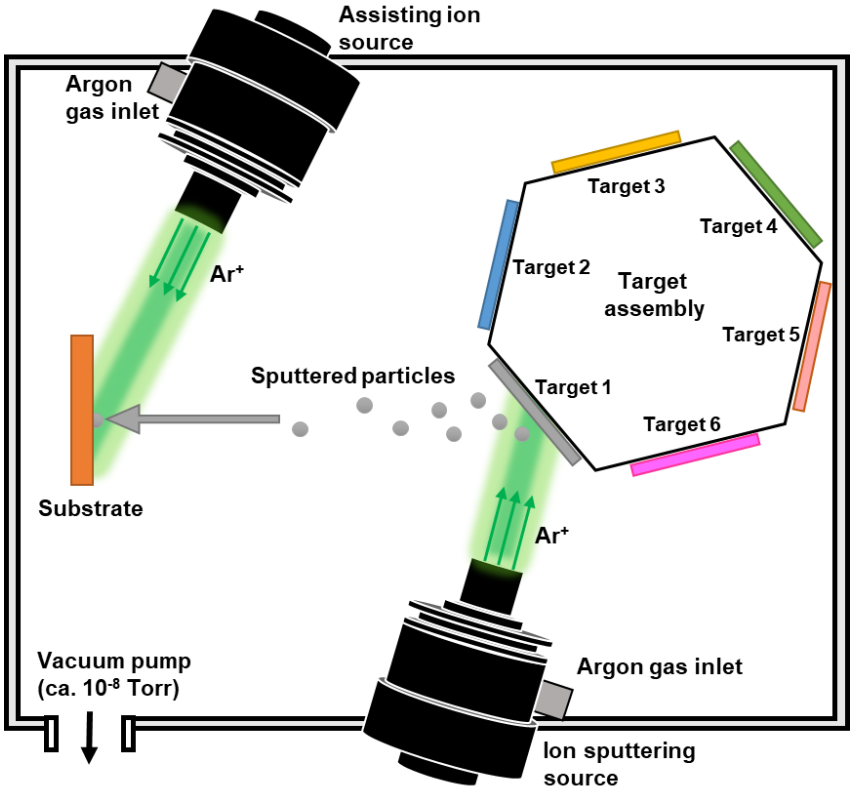

Figure 4.2. Schematic illustration of the ion beam sputtering setup, including a second gridded ion source focused on the substrate.

Electrochemical deposition NPs. AgNPs and, in general, metallic nanostructures, can be deposited onto a conductive substrate by electrochemical methods. The most common electrochemical technique for electro-deposition is cyclic voltammetry [218,228,229]. However, the double-potentiostatic method, even though not widely employed for the synthesis of NPs, has advantages in comparison to cyclic voltammetry. For instance, it allows excellent control of the particle size and shape by varying the deposition parameters (potential values and time) and using dilute precursor solutions (below the mmol L^{-1} range). The double-potentiostatic method consists of two steps: (*i*) the nucleation step where a high cathodic overpotential is applied for a short time (usually in the millisecond range) and (*ii*) the growth step, in which a smaller overpotential, close to the reduction potential of the metal, is applied for longer times (few second up to minutes).

From a mechanistic point of view, at high overpotentials, the metallic cations are reduced at the surface-electrolyte interface, producing atoms adsorbed onto the surface (adatoms) that start to aggregate and form clusters with low surface tension. When the clusters reach a critical size (nuclei), their surface energy is low enough that their dissolution is thermodynamically not favorable.

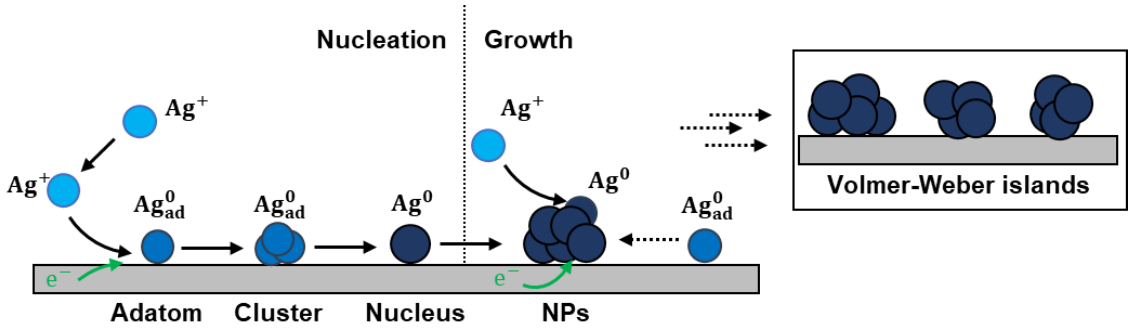

Figure 4.3. Mechanism of the electrochemical growth of NPs following the Volmer-Weber model.

When the formation rate of the nuclei is fast enough (condition achievable at high overpotential), the generation of nuclei is not influenced by the local environment of neighboring nuclei and the nucleation follows a complete spatial randomness (CSR) distribution, *i.e.*, all occurrences are independent and follow a Poisson distribution[a] [230]. The application of a following lower overpotential leads to the growth of nuclei. This process can occur through two different mechanisms: (*i*) indirectly, through the formation of adatoms on the surface and the subsequent diffusion to the nucleus (lateral growth), and (*ii*) through direct electrochemical reduction of the cations onto the growing nucleus (vertical growth) [230]. The growth of the nuclei described and depicted in Figure 4.3 follows the Volmer-Weber mechanism, in which separated NPs grow randomly dispersed on the surface [230,231].

4.1.2. Mechanism of action of AgNPs: a synergistic activity

Numerous studies evidenced that the toxicity of AgNPs is not only due to the antimicrobial activity of the AgNPs themselves, but also due to the presence of released silver(I) ions. The minimal inhibitory concentration (MIC) is in the range of nmol L^{-1} for AgNPs and µmol L^{-1} for the silver(I) ions [232–235]. The release kinetics of silver(I) ions depends on the conditions, how the NPs have been synthesized. For example, the release kinetics can be regulated by modifying the particle surface with specific capping agents that favor the oxidative dissolution of the AgNPs (Figure 4.4a). AgNPs coordinated with citrate as a capping ligand, for example, exhibited a higher ion release ratio and enhanced antimicrobial activity in comparison to AgNPs capped with other common ligands using the same experimental conditions [236,237].

[a] The Poisson distribution is defined by $f(n) = (\mu^n e^{-\mu})/n!$, where n is the number of occurrences (*e.g.*, nucleation), μ is the number of particles (nuclei) per unit area and time, and e is the Euler´s number ($\sim$ 2.71828). The Possion distribution assumes that occurrences take place random in space and time (ref: [324]).

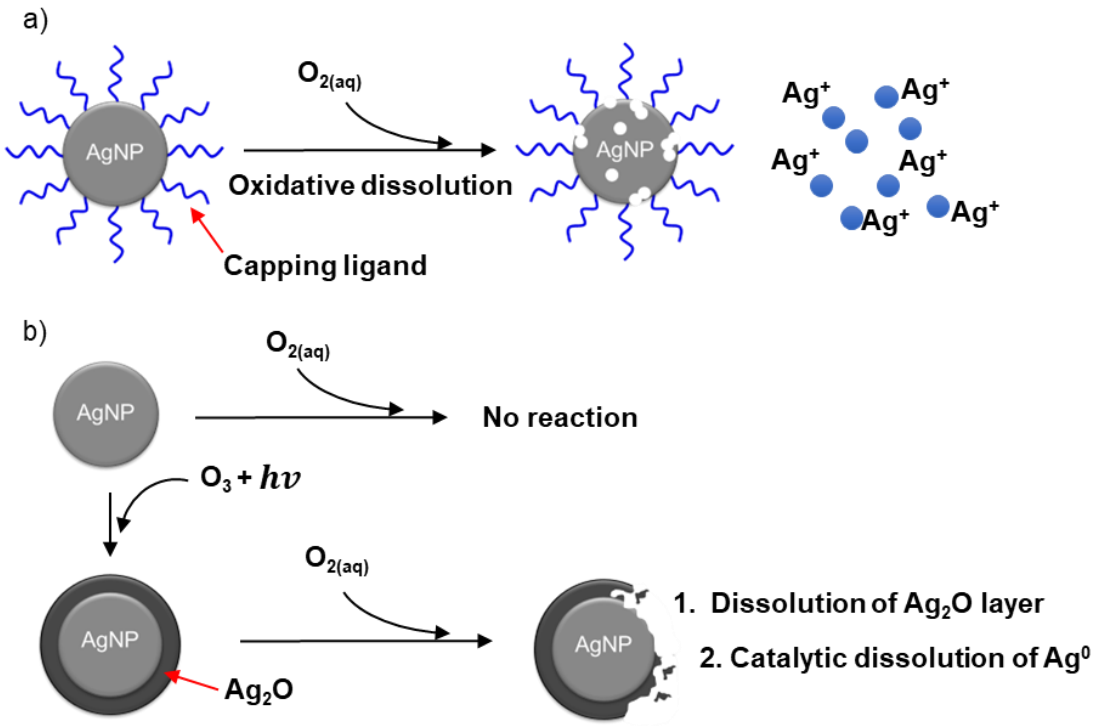

Figure 4.4. Silver(I) release mechanism. (**a**) Oxidative dissolution of the AgNP regulated by capping agents. (**b**) Formation of a "core-shell" AgNP through the treatment of metallic AgNPs with UV-ozone and consequent dissolution of the oxide outer shell and the catalytic dissolution of the metallic silver core. The dissolution of pure metallic silver cores is not thermodynamically favored.

AgNPs synthesized *via* electrochemical methods usually lack capping agents and oxidative dissolution is not thermodynamically favored, since the dominant state of the NPs is metallic silver [238]. To overcome this problem, AgNPs synthesized by electrochemical methods can be oxidized by, *e.g.,* UV-ozone treatments, to obtain a metallic silver core coated by a surface oxide layer as the outer shell [239]. The presence of the oxidized outer shell favors the first dissolution of the silver oxide and the subsequent oxidative corrosion of metallic silver [239], as shown in Figure 4.4b.

Even though the mechanism of action of AgNPs and silver(I) ions is still under debate, it is accepted that the antimicrobial activity is based on three possible pathways: (*i*) damage of bacterial cell membrane, (*ii*) inhibition of cellular functions and metabolism, and (*iii*) generation of reactive oxygen species (ROS) [240].

Damage of bacterial cell membrane. The interaction of AgNPs and silver(I) ions with the surface of the bacteria might be the primary and most important mechanism of action of these antimicrobials. The bacterial envelope is a complex multilayer structure that protects bacteria from the environment and allows the uptake of nutrients to maintain cellular growth. In general, there are two classes of bacteria, classified by the composition

of the cellular envelope: gram-negative and gram-positive bacteria. Gram-negative bacteria are surrounded by a cell wall composed of peptidoglycans and covered by a layer of lipopolysaccharides that form the so-called outer membrane (Figure 4.5a). Gram-positive bacteria lack the outer membrane but exhibit a thinker layer of peptidoglycans [241]. In addition to the lipid components, the envelope of both classes of bacteria contains membrane proteins (Figure 4.5b). When AgNPs and silver(I) ions get in contact with the bacterial envelope several interactions can occur, which are mainly based on the affinity of the silver with proteins and lipids.

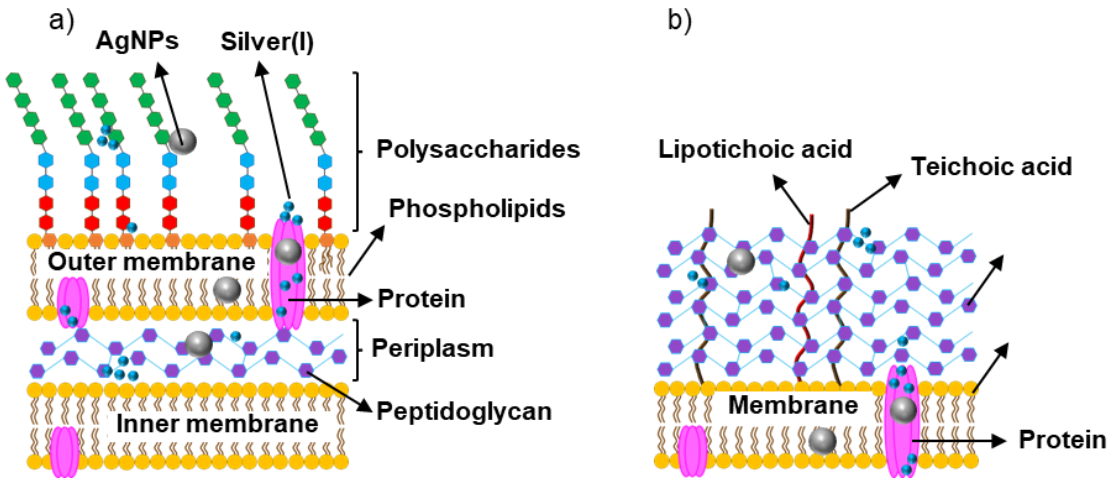

Figure 4.5. Schematic structure of (**a**) gram-negative bacterial cell envelope and (**b**) gram-positive bacterial cell envelope. AgNPs (grey particles) and silver(I) ions (blue particles) can interact with polysaccharides, phospholipids, proteins, and peptidoglycans, leading to cell envelope damage.

The first mechanism involves the interaction of silver(I) ions with electron donor groups such as sulfhydryl, imidazole, amino, and phosphate groups that are extensively present in the membrane proteins. Silver(I) ions can interact and bind to thiol groups and form stable S-Ag bonds that lead to the inactivation of membrane proteins. The second mechanism, in which both AgNPs and silver(I) ions are active, is the *cis*-to-*trans* isomerization of the lipidic part of the cell membrane, mostly formed by unsaturated fatty acids. This isomerization leads to a modification of the membrane composition and thus to a change in the membrane structure and fluidity, which can increase the overall permeability and culminate in membrane damage [232,236]. The effects of the AgNPs and silver(I) ions have been extensively studied using imaging techniques like SEM and AFM, showing that the presence of AgNPs and silver(I) ions produces the formation of pits, increase of cell rugosity, and leads to membrane fragmentation [242–248]. These structural abnormalities have been investigated in the course of this thesis and will be described in detail in **Section 4.2** and **Section 4.3**.

Inhibition of cellular functions. AgNPs and, especially silver(I) ions can penetrate the bacterial cell and once they are in the cytoplasm, they interact with cellular structures like nucleic acids and proteins, leading to the inhibition of basic cellular functions, such as DNA transcription, protein synthesis, and metabolic pathways. In particular, the interaction of silver(I) ions with the electron-donor groups of proteins can interfere with the respiratory chain, impair the transport and release of potassium ions and inhibit the synthesis of adenosine triphosphate (ATP) [236].

Generation of ROS. Electron spin spectroscopy (ESR) studies revealed that the generation of ROS species is induced by AgNPs. The ROS formation could be correlated to the antimicrobial activity of AgNPs [249]. However, the antimicrobial effect of AgNPs is not only due to the catalytic activity of the NPs for the generation of ROS but also due to the direct disruption of the free radicals scavenger systems that maintain the levels of ROS at low concentrations [250,251]. The accumulation of intracellular ROS leads to direct damage and hyper-oxidation of the mitochondrial membrane, cell membrane, DNA, and proteins [252,253].

Figure 4.6 summarizes the main antimicrobial mechanism and interaction of AgNPs and silver(I) ions.

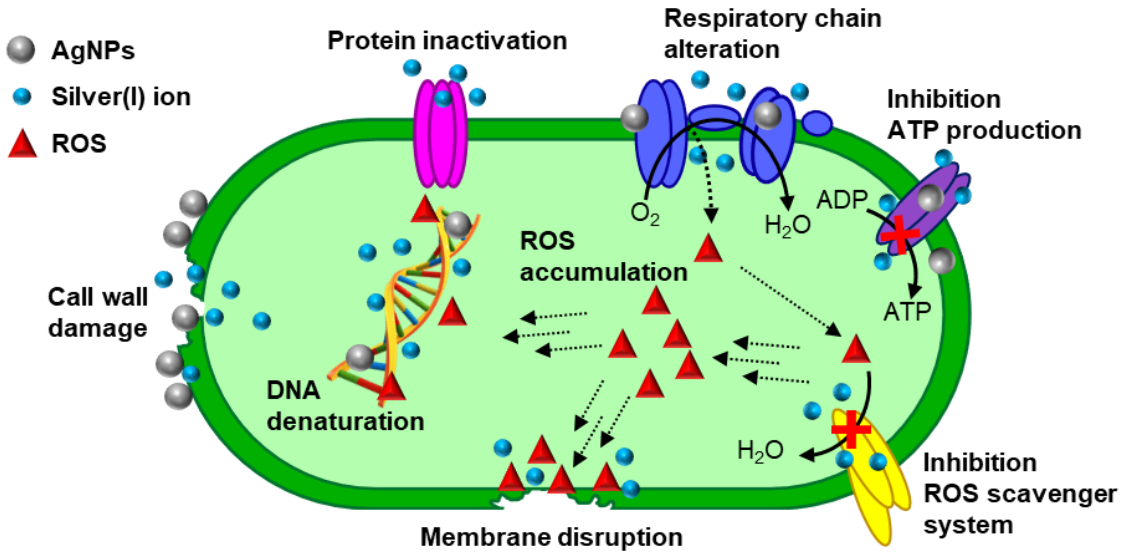

Figure 4.6. General mechanism for the antimicrobial action of AgNPs and silver(I) ions.

4.2. Silver-fluoropolymer (Ag-CFX) films: Kinetic study of silver release, and spectroscopic-microscopic insight into the inhibition of P. fluorescens biofilm formation

Parts of this section have been already published and are reprinted from the following article: **Caniglia, G.**; Sportelli, M. C.; Heinzmann, A.; Picca, R. A.; Valentini, A.; Barth, H.; Mizaikoff, B.; Cioffi, N.; Kranz, C. Silver-Fluoropolymer (Ag-CFX) Films: Kinetic Study of Silver Release, and Spectroscopic-Microscopic Insight into the Inhibition of P. Fluorescens Biofilm Formation. *Anal. Chim. Acta* **2022**, *1212*, 339892. https://doi.org/10.1016/j.aca.2022.339892. Copyright © 2022, The Authors. Published by Elsevier B.V.

Declaration of contribution: Giada Caniglia performed the presented SECM and AFM studies, including the kinetic studies of silver(I) release. Maria Chiara Sportelli performed the IBS, XPS, and ETAAS experiments. Anna Heinzmann, Rosaria A. Picca, Antonio Valentini: data curation. Holger Barth: resources. Boris Mizaikoff, Nicola Cioffi and Christine Kranz: supervision-review and editing.

4.2.1. Introduction

AgNPs have received significant attention due to their antimicrobial activity and relative biocompatibility, being nowadays employed in numerous applications, such as food storage, medical devices, and the manufacturing industry [197,249,254,255]. It has been shown that the antimicrobial effectiveness of AgNPs arises from the activity of the NPs themselves and the silver(I) ions released from the NPs, in which the AgNPs play the role of drug carriers. The application of AgNPs often requires the formulation of integrated chemical systems, which are mostly based on the implementation of polymer-supported NPs. Among others, Teflon-like polymers (CF_X) are a class of fluoropolymers with high scientific and industrial interest, due to their chemical stability, resistance to corrosion, high surface resistivity, and hydrophobicity [256] that make them suitable NPs platforms for the application in a variety of fields, such as anti-stain coatings, optoelectronics, and nano-antimicrobials [257–260].

To date, the Ag-CF_X system has been still barely investigated regarding both the preparation and antimicrobial activity [257–259,261–263]. Recently in their work, Sportelli et al. [264] showed that the deposition of Ag-CF_X, with excellent control of the film thickness, particle size, and distribution, can be achieved by ion beam co-sputtering (IBS). The authors also described the Ag-CF_X system as a promising coating with attractive antimicrobial properties, since the polymeric matrix not only stabilizes the

AgNPs but also allows a controlled release of the antimicrobial over time. The swelling behavior of the CF_X matrix is supposed to be the main mechanism that controls the release of silver(I) ions, however further studies are needed to confirm this hypothesis. Herein, the kinetics and mechanism of the silver(I) ion release has been investigated *via* scanning electrochemical microcopy (SECM) [33,56,57] combined with anodic square voltammetry (ASV) [33,72], and *via* electrothermal atomic absorption spectroscopy (ETAAS). The antimicrobial activity of the Ag-CF_X films against *P. fluorescens* was investigated using AFM in terms of bacterial coverage and cell morphology, correlating these results with the silver(I) ions release and swelling of the polymeric matrix.

4.2.2. Results and discussion

4.2.2.1 Characterization of Ag-CF_X samples

The TEM image depicted in Figure 4.7a shows a homogenous spatial distribution of the AgNPs co-sputtered within the PTFE, revealing an average particle size of 8.4 ± 0.2 nm (n = 243), as can be seen in the histogram in Figure 4.7b. The chemical state of the AgNPs was determined by the position of the peaks associated with the binding energy of the emitted photoelectrons in the XPS spectrum, which was recorded in the range from 380 eV to 364 eV.

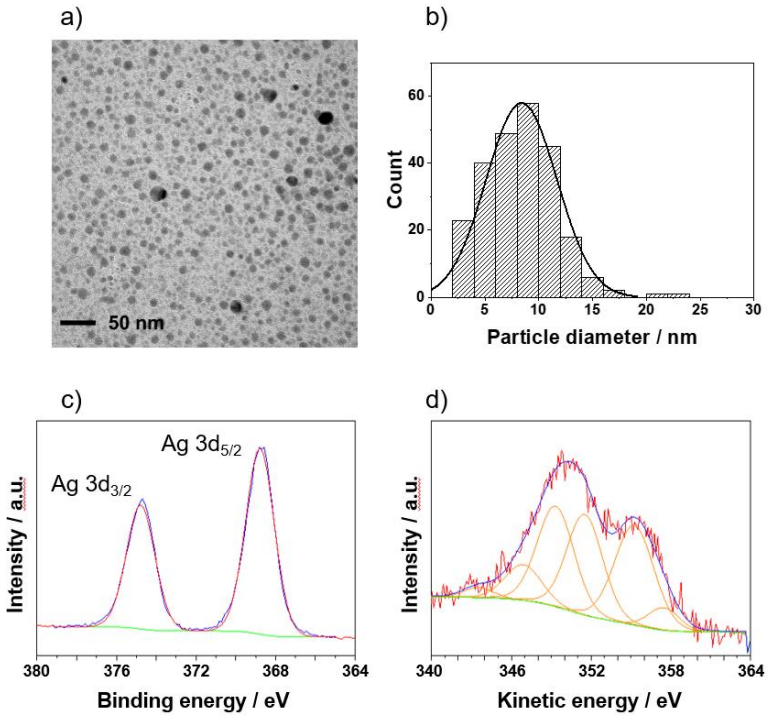

Figure 4.7. (**a**) TEM image and (**b**) particle size distribution (n = 243) of the AgNPs in the Ag-CF_X film. (**c**) XPS high-resolution spectra of Ag $3d_{3/2}$ and Ag $3d_{5/2}$ from the Ag-CF_X films. (**d**) Auger Ag(MNN) transition lines.

As shown in the XPS spectra depicted in Figure 4.7c, the peaks at 374.75 eV (Ag $3d_{3/2}$) and 368.70 eV (Ag $3d_{5/2}$) reveal that the dominant state of the AgNPs is metallic [265]. However, a small portion of the AgNPs are found to be in their oxidized state, as confirmed by the Auger parameter, α' = 724.0 eV, obtained from the Ag(MNN) transition lines (Figure 4.7d), which is close to the Auger parameters observed in Ag_2O (724.3 eV) and AgO (724.2 eV) [264–266]. The presence of oxidized silver species might be due to partial surface oxidation of the elemental silver nanophases, induced by exposure to air of the Ag-CF_X films [264].

4.2.2.2 SECM analysis

Calibration and electrochemical behavior of silver. The quantification of silver(I) ions has been performed by combining SECM and ASV-SWV, which consists of an electro-deposition step of silver onto the UME and then an anodic stripping step where the silver is re-oxidized. The current response, evaluated *via* the area under the peak in the square wave voltammogram, is proportional to the concentration of silver(I) ions. The stripping step, in which the metallic silver is oxidized, may result in the formation of different states of silver(I) and silver(II) and, therefore, generate the corresponding anodic peaks shown in Figure 4.8. Three different anodic peaks have been observed during the stripping process, which can appear or not, depending on the concentration of silver(I) ions. At lower concentrations (from 311 up to 1200 µm L^{-1}), the most pronounced peaks appear at + 0.37 V and +0.56 V, while at increased concentrations of silver(I) ions, a third sharp peak appears at +0.24 V. All the potential are shown *versus* Ag/AgCl, KCl (sat.) reference electrode. Figure 4.8 shows a representative square voltammogram recorded at a concentration of silver(I) ions equal to 2735 µm L^{-1} in which the three anodic peaks are observed.

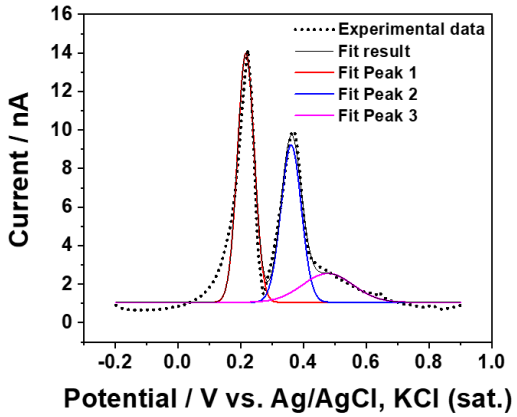

Figure 4.8. Peak deconvolution of an exemplary square wave voltammogram (silver(I) concentration in solution equals 2735 µg L^{-1}).

According to the literature, the peaks at + 0.37 V and + 0.56 V correspond to the formation of silver(I) oxide and silver(II) oxide, according to the reactions depicted in equations 4.1 and 4.2 [267]. The peak at + 0.24 V is associated with the electro-dissolution of metallic silver to form a dihydroxosilverate(I) complex [268] that is stable in a dilute alkaline solution and is formed by the equilibrium between silver(I) oxide and silver(II) oxide (equation 4.3) [269].

$$2Ag + H_2O \rightarrow Ag_2O + 2H^+ + 2e^- \quad (4.1)$$

$$Ag_2O + H_2O \rightarrow 2AgO + 2H^+ + 2e^- \quad (4.2)$$

$$2Ag + 2OH^- \rightarrow [Ag(OH)_2]^- + 2e^- \quad (4.3)$$

As evident in the reactions abovementioned, the direct dissolution of metallic silver during the stripping arises from equations 4.1 and 4.3, while the reaction in equation 4.2 describes the oxidation of silver(I) oxide already formed from the stripping of metallic silver. Therefore, for the quantification of silver(I) ions only the areas under the peaks at 0.24 V and 0.37 V are considered. Figure 4.9a shows the representative square wave voltammograms at different silver(I) concentrations and the appearance of the different peaks depending on the concentration can be seen. The calibration curve (Figure 4.9b) for the quantification of silver(I) ions has been constructed in the range of 211 to 1947 µg L^{-1} and a linear correlation (R^2 = 0.99112) was obtained, achieving a LOD and LOQ of, respectively, 74 µg L^{-1} and 245 µg L^{-1}.

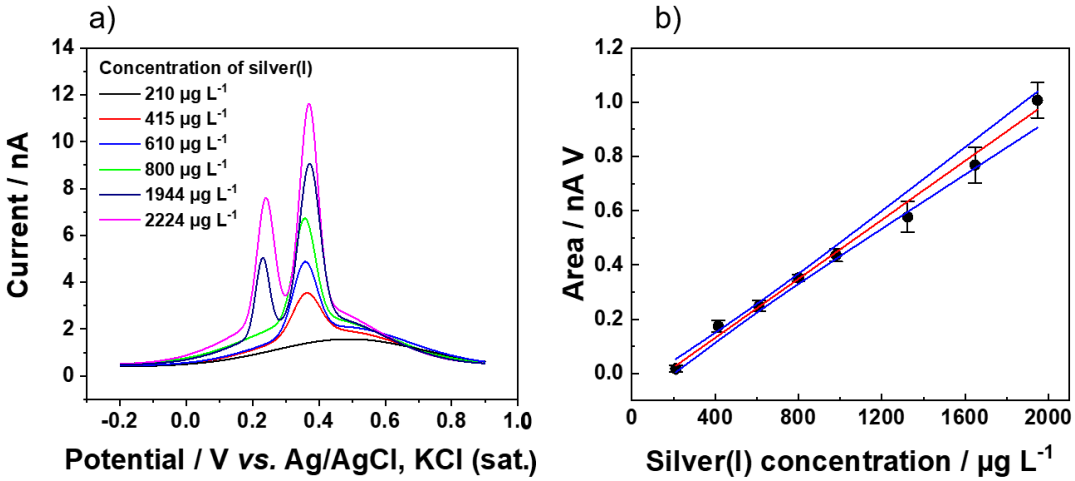

Figure 4.9. (**a**) Square wave voltammograms at different $AgNO_3$ concentrations measured in the bulk solution with a Pt UME (radius: 12.5 µm and RG = 9). (**b**) Calibration curve (red line) of silver(I) recorded at the Pt UME with increasing $AgNO_3$ concentrations. The blue lines denote the uncertainty range, and the error bars reflect three repetitive measurements. Electrolyte: 0.5 M KNO_3.

Kinetics of silver release via SECM-SWV. For the silver(I) release measurements, the Pt UME was first positioned at a distance of 79 µm above the Ag-CF_X surface. Feedback SECM mode was used to position the UME, which was biased at – 0.80 V resulting in a diffusion-limiting current of the dissolved oxygen reduction (equation 4.4), as shown in the voltammogram depicted in Figure 4.10a. The current response was recorded as a function of the tip-surface distance, as shown in Figure 4.10b. Since Ag-CFx is electrically insulating due to the presence of the Teflon-based polymer, negative feedback was expected, which is reflected by the decrease of the normalized current with the decrease of the tip-surface distance, due to the partial blockage of the oxygen diffusion toward the UME.

$$O_2 + 2H_2O + 2e^- \rightarrow H_2O_2 + 2OH^- \qquad (4.4)$$

The experimental approach curve (black line in Figure 4.10) was fitted using the Cornut and Lefrou equation [270] for a UME with a radius equal to 12.5 µm and a RG of 10.

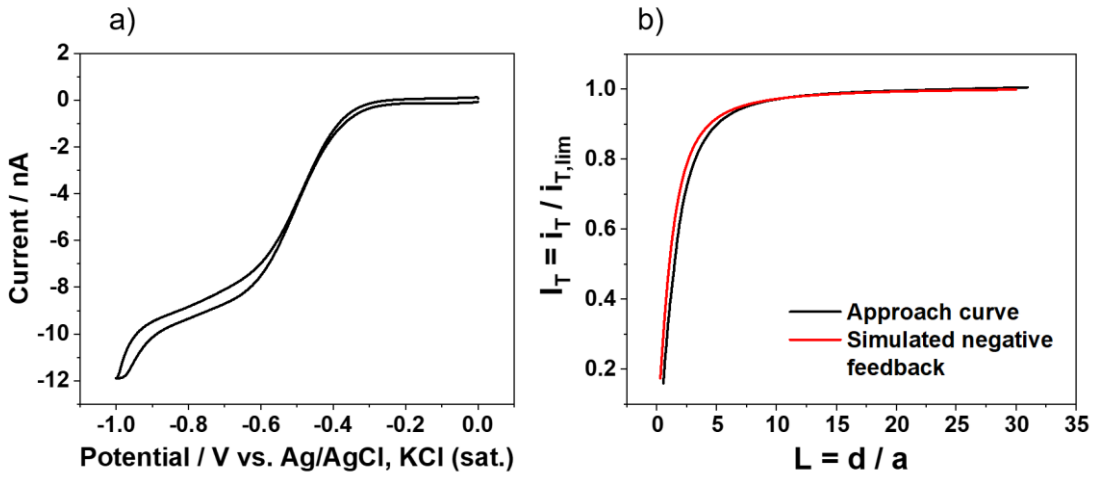

Figure 4.10. (a) Cyclic voltammogram for the reduction of dissolved oxygen measured with a 12.5 µm-diameter Pt UME in 0.1 mol L^{-1} KNO_3. (b) Approach curve (black line) recorded at the Ag-CF_X surface using oxygen as the redox active species. The red line represents the simulated approach curve obtained using the fit introduced by Cornut and Lefrou [270].

Once the UME was positioned at a distance of 79 µm above the Ag-CF_X surface, ASV-SWV experiments were conducted in 0.1 mol L^{-1} KNO_3 over time up to 27 h of immersion. The silver(I) ion concentration profile, shown in Figure 4.11a, follows a pseudo-first-order kinetic, according to the relation $[Ag]_t = [Ag]_\infty(1 - e^{-kt})$, from which the values of the rate constant (k = 0.113 ± 0.008 h^{-1}) and the plateau concentration of released silver(I) ($[Ag]_\infty$ = 1310 ± 50 µg L^{-1}) could be extracted.

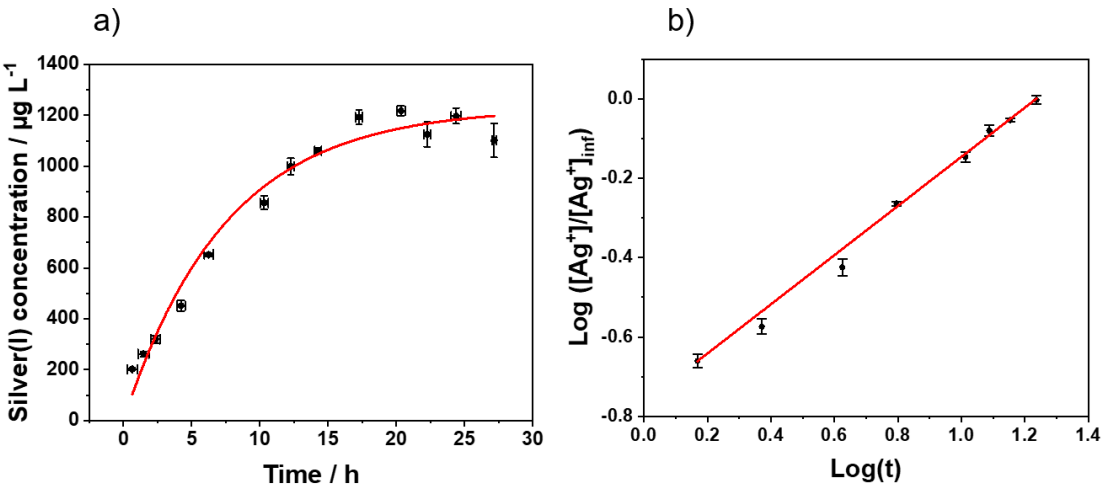

Figure 4.11. (a) First-order kinetic model of silver(I) release obtained by SECM-SWV at a distance of 79.0 µm above Ag-CF_X surface. (b) $Log([Ag^+]_t/[Ag^+]_\infty)$ vs. $log(t)$ graph according to the Korsmeyer-Peppas kinetic model of silver(I). The error bars reflect the measurement of three different samples.

To investigate the silver(I) release and the influence of the swelling of the polymer on the ion release, the data obtained within the first 14 h of immersion were evaluated using the Korsmeyer-Peppas (KP) model [271]. The KP model describes the mechanism of drug release from polymeric systems, considering the diffusion of water into the matrix, the swelling of the polymer, and the dissolution of the matrix. Within this model, the drug release mechanism can be classified as (*i*) the *Fickian model*, where the release is controlled only by diffusional processes of the drug, since the drug release is governed by thermodynamic forces, such as concentration gradients and the diffusion rate of the solvent is higher than the polymeric chain relaxation processes; (ii) *non-Fickian model*, where drug release is controlled by other physical-chemical processes arising from the matrix, such as swelling and polymeric relaxation, and (iii) *anomalous transport,* in which the drug release is controlled by diffusion and matrix relaxation [272].

The KP model is expressed by equation 4.5 [273] or by its linearized form as shown in equation 4.6; the type of mechanism is described by the n-exponent, also called release exponent. When the geometry of the substrate is a slab or a thin film, such as the Ag-CF_X samples, the two limiting cases are the diffusion-controlled release (n = 0.5, *i.e.*, *Fickian model*) and the swelling-controlled release (n = 1.0, *i.e.*, *non-Fickian model*). Values between 0.5 and 1.0 describe the superposition of both limiting cases (*anomalous transport*).

$$\frac{\mathrm{M_t}}{M_\infty} = kt^n \quad (4.5)$$

$$\mathrm{Log}\frac{\mathrm{M_t}}{\mathrm{M_\infty}} = \mathrm{Log}(k) + \mathrm{nLog}(t) \quad (4.6)$$

Here, M_t/M_{inf} is the fraction of drug released in time t, k is the kinetic rate constant and n is the release exponent, which describes the mechanism of the drug release.

The log-log plot of $[\mathrm{Ag^+}]_\mathrm{t}/[\mathrm{Ag^+}]_\infty$ versus time (Figure 4.11b) fits quite nicely to the Korsmeyer-Peppas model (R^2 = 0.99973), where the n-exponent value (0.6420 ± 0.0003, n = 3) suggests that the silver(I) release was mainly controlled by the swelling of the Ag-CF_X matrix. This aspect is in accordance with the literature [274–276] since the inherent mechanism of silver(I) release from the fluoropolymer can be described by, firstly, the diffusion of the water into the polymer matrix leading to subsequent swelling of the film and the oxidation of the AgNPs to silver(I) ions, which diffuse into the solution. Swelling studies described in the **Section 3.2.4.3** confirms this behavior.

Comparison with ETAAS bulk experiments. Bulk experiments performed through ETAAS confirm the tendency of the silver(I) ion release to follow pseudo-first-order kinetics (R^2 = 0.95265) during the first 24 h of immersion (*data not shown*). ETAAS studies show a release rate equal to 1.6 ± 0.7 h^{-1} (n = 3) and a silver(I) plateau concentration of 116 ± 7 µg L^{-1} (n = 3). Interestingly, there is a significant difference in the plateau concentration obtained from SECM experiments ($[Ag]_\infty$ = 1310 ± 50 µg L^{-1}) and the concentration obtained by ETAAS measurements ($[Ag]_\infty$ = 113 ± 7 µg L^{-1}); the latter is more than one order of magnitude lower. This difference arises from the nature of the techniques used and the size of the investigated area. We decided, thus, to compare the two techniques by normalizing the concentration of silver(I) in terms of mass of silver(I) ion released per unit area.

In bulk ETAAS experiments, the liquid-sample contact area arises from the 500 µL-droplet used during the measurements with an approx. diameter of 2 cm, and thus a contact area of ca. 3.14 cm^2 ($A = \pi r^2$), as shown schematically in Figure 4.12a. Considering a concentration of silver(I) equal to $[Ag]_\infty$ = 113 µg L^{-1} in a volume of V = 500 µL, the total amount of silver(I) released per unit area in ETAAS experiments is then: ρ_{ETAAS} = 0.0186 µg cm^{-2} ($\rho_{ETAAS} = [Ag]_\infty V/A$).

In SECM experiments the total volume cannot be exactly estimated, thus the mass of silver(I) released is estimated using Faraday´s law (equation 4.7), through the charge obtained from the anodic peak area of the voltammograms.

$$m = q\frac{M}{F\,z} = \frac{A_{peak}}{v}\frac{M}{F\,z} \qquad (4.7)$$

Here, q is the electric charge in Coulomb, M the atomic mass of silver in g mol^{-1}, F is the Faraday constant, z the valency of the ion, and v the stripping scan rate (equal to 0.05 V s^{-1}). The total mass of silver(I) was determined to be equal to 1.3 10^{-5} ± 0.1 10^{-5} µg (n = 3). The area of the sample investigated by SECM can be roughly approximated considering the total UME diameter (which equals the electroactive diameter and the diameter of the surrounding glass shielding) as shown in Figure 4.12b. Considering an average radius of 145 µm, obtained by optical microscopy, the total area investigated was approx. 7.45·10^{-4} cm^2, thus the amount of silver per unit area was ρ_{SECM} = 0.0174 µg cm^{-2}.

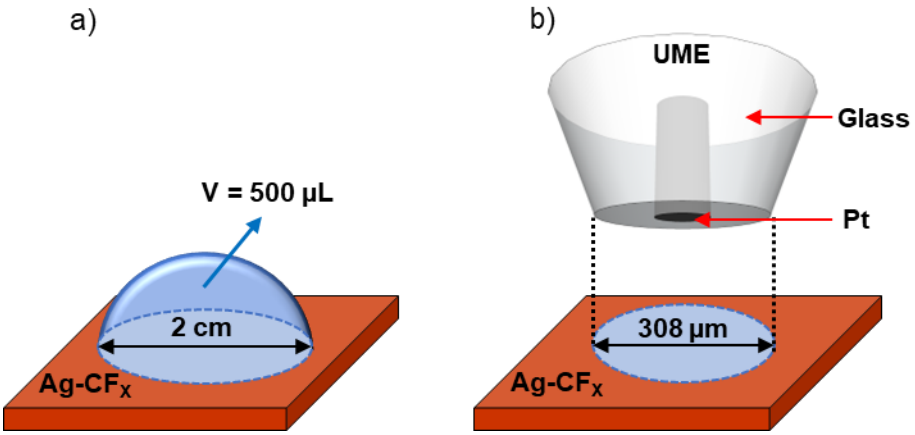

Figure 4.12. (**a**) Schematics of the probed area by ETAAS. (**b**) Geometry of an SECM tip positioned at 79 µm to the surface and the estimated diffusion layer of silver(I).

Hence, considering the amount of silver(I) released per unit area, the comparison of the performed experiments (SECM and ETAAS) revealed an excellent agreement with a relative error lower than 2.5%.

4.2.2.3Swelling studies

The swelling behavior of the Ag-CF$_X$ samples was investigated over time in both, FIB-milled and scratched Ag-CF$_X$ surfaces, immersed in either water or PBS. Figure 4.13a and b show the AFM images recorded in air (immersion time $t = 0$) of a Ag-CF$_X$ film with two FIB-milled patterns (removal of the film) and a mechanically scratched film, respectively. The heights of the film were obtained *via* cross-sectional AFM line-scans at the patterns/scratches (Figure 4.13c and d). The swelling was calculated as the difference between the depths of the pattern/scratch in the swollen, $\mathrm{D_s}$, and the dry, $\mathrm{D_d}$, state: $Swelling = \mathrm{D_s} - \mathrm{D_d}$.

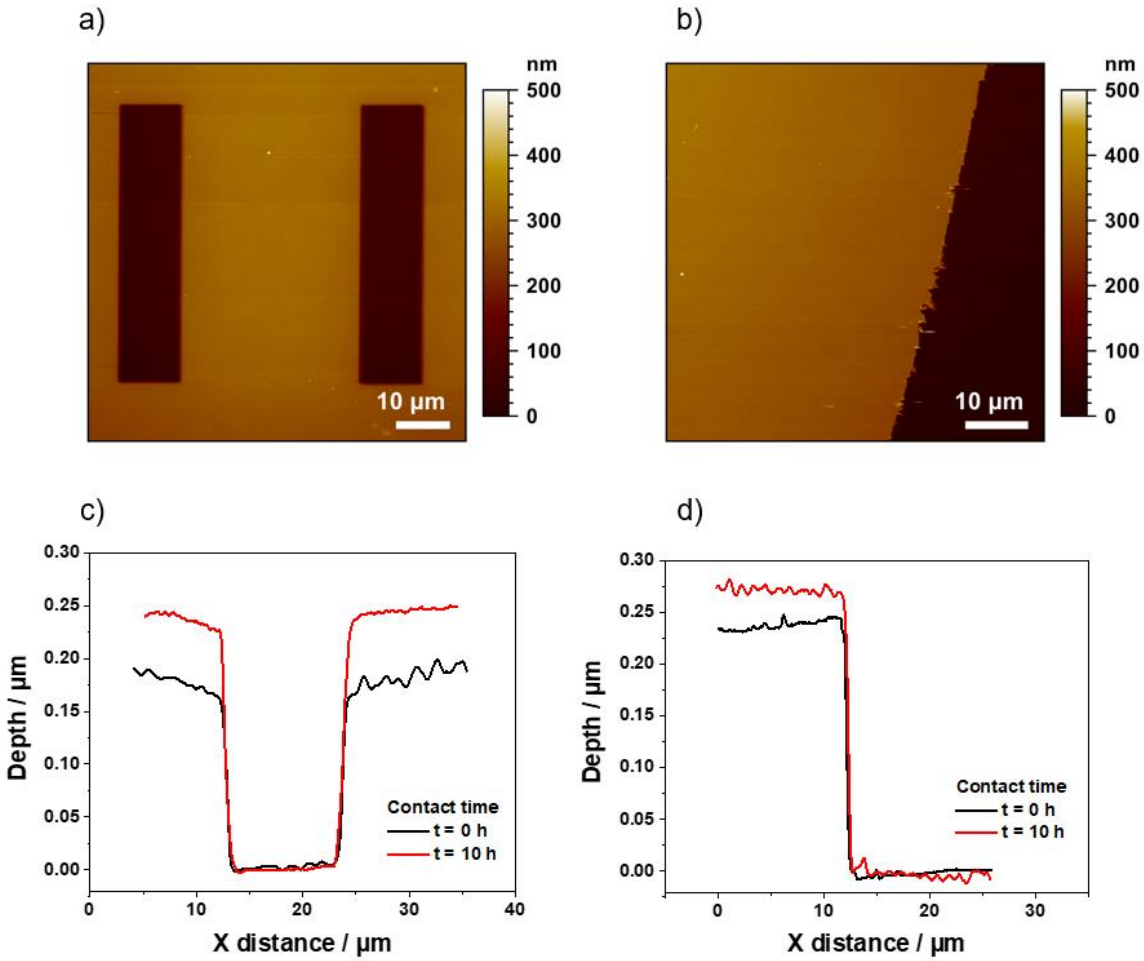

Figure 4.13. (**a, b**) AFM image in air of the (**a**) patterned Ag-CF_X film on a silicon substrate and (**b**) scratched Ag-CF_X film on a silicon substrate. (**c, d**) Line scans display the depth profile before the immersion and after the immersion in water for 10 h; (**c**) the patterned Ag-CF_X sample and (**d**) the scratched Ag-CF_X sample.

As expected from the kinetic study of the silver(I) ion release, the fluoropolymeric matrix of the Ag-CF_X films exhibits swelling behavior when the film is in contact either with water (Figure 4.14a and b) or a PBS solution (Figure 4.14c). A total swelling of 128 ± 5 nm (n = 3) was observed after 14 h of immersion in water and at that time also a plateau is reached. When the sample was immersed in PBS solution, the swelling behavior is slightly reduced by ca. 30 nm and the plateau is reached after 12 h of immersion (Figure 4.14c).

The experiments performed with mechanical scratches arise from the assumption that the treatment with FIB-milling might change the composition of the fluoropolymer and favor crosslinking [277–280], which might influence the swelling behavior of the film. However, Figure 4.14b clearly shows that possible crosslinking due to exposure of the film to the Ga ion beam does not significantly affect the swelling behavior of the fluoropolymer within the first 14 hours of immersion in MilliQ water.

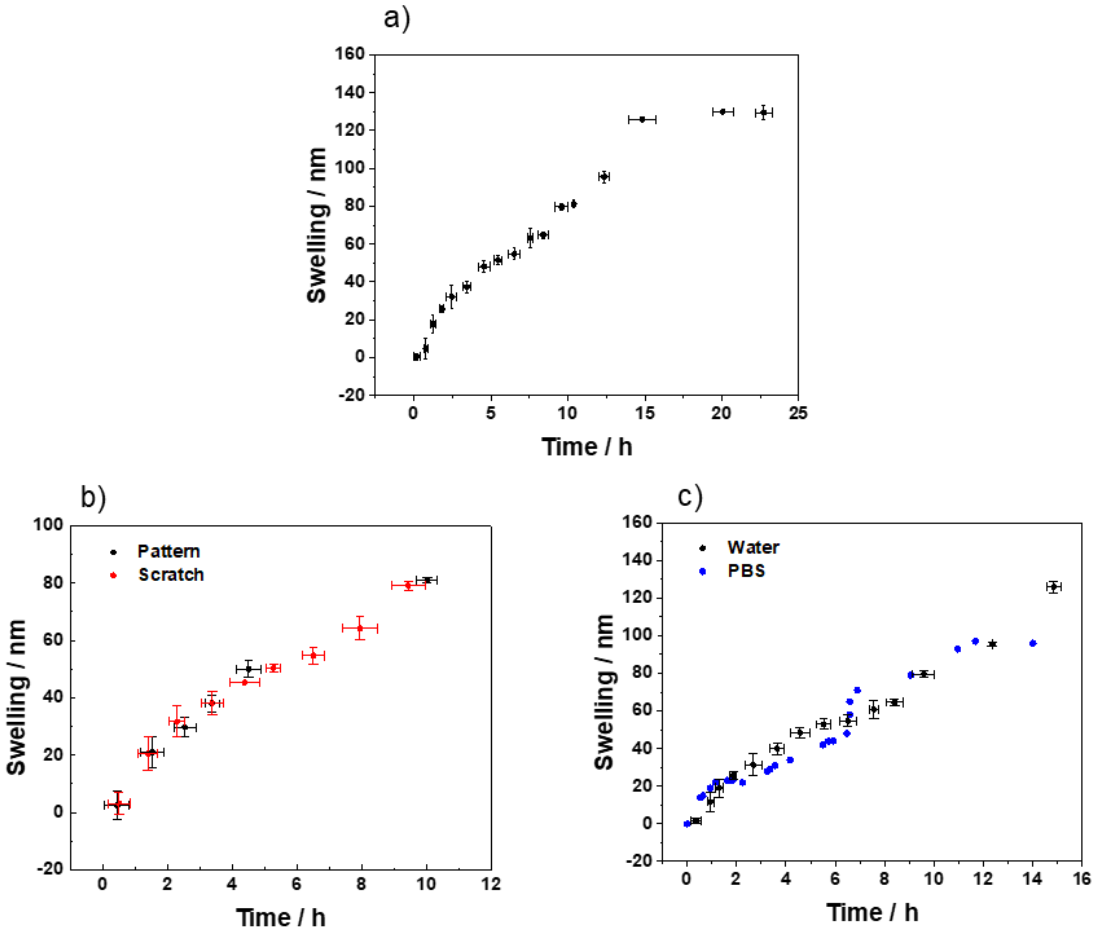

Figure 4.14. (**a**) Swelling behavior of patterned Ag-CF_X film monitored in water over a time of 24h. (**b**) Swelling behavior of patterned (black) and scratched (red) Ag-CF_X samples in MilliQ water monitored for 10 h. (**c**) Swelling behavior of patterned Ag-CF_X film monitored in water (black) and PBS (blue) over a time of 15 h. The error bars reflect the measurement of three different samples.

4.2.2.4 Morphological studies of *P. fluorescens*

For a more comprehensive understanding of the role of the AgNPs and silver(I) release from the Ag-CF_X samples, the growth of *P. fluorescens* on pristine and previously swollen Ag-CF_X samples was investigated in terms of bacterial coverage and cell morphology. The swollen Ag-CF_X was prepared by immersing a pristine sample in MilliQ water for 30 h to trigger silver(I) release.

To this end, a culture of *P. fluorescens* was incubated on pristine and swollen samples under the same experimental conditions (the same time, temperature, and growth medium). The resulting inoculated samples were then investigated *via* AFM. Figure 4.15a and b show representative AFM images of the bacteria grown on the pristine and the swollen Ag-CF_X samples, respectively. For the swollen sample, a lower concentration of AgNPs was assumed due to the previously release of silver(I) ions. The

sample exhibits a higher density of bacteria and the formation of biofilms (Figure 4.15b) with a surface coverage equal to 41.5 ± 0.7 % (n = 3, from 60 x 60 μm^2 areas). In contrast to the pristine sample, where silver(I) ions are released during the incubation of the bacteria, that results in a more pronounced antimicrobial effect visible with a lower density of bacteria, attenuated formation of biofilms (Figure 4.15a), and total coverage of 24.1 ± 0.5 % (n = 3), as shown in the histogram depicted in Figure 4.15c.

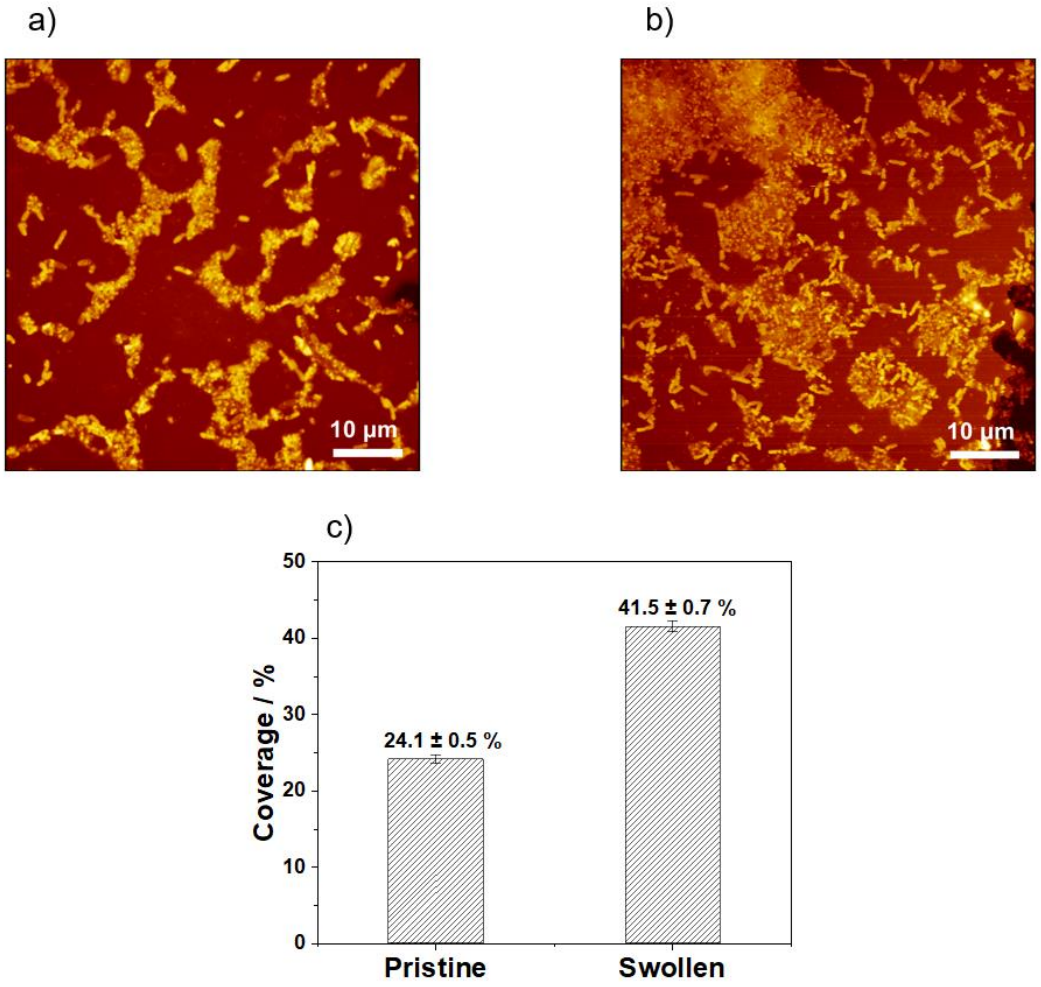

Figure 4.15. (**a, b**) Contact mode AFM topography image recorded in air of *P. fluorescens* after 30 h of incubation on the (**a**) pristine and (**b**) swollen surface Ag-CF_X. (**c**) Bar chart of the measured coverage. Error bars reflect the measurements of three different samples.

The antimicrobial effect of the pristine Ag-CF_X samples is also visible from the significant change in morphology and size of the bacteria. Indeed, as shown in Figure 4.16a, for the originally pristine samples, a layer of coccoidal round-shaped bacteria is surrounded by smaller rod-shaped cells, while in the swollen samples (Figure 4.16b), *P. fluorescens* cells exhibit the expected rod-shape form, characteristic of this bacterial strain grown in absence of external stress. The shape of the bacteria can be evaluated in terms

of circularity, which is defined as the roundness of an object, which is described by equation 4.7. According to this definition, coccoid-shaped cells are expected to exhibit circularity close to 1.0*, i.e.*, with a length-to-width ratio of 1.0, while values of circularity below 0.7 are more characteristic of rod-shaped bacteria (length-to-width ratio higher than 2.4) [281]. The shape of the bacteria was then statistically evaluated in terms of circularity, from three AFM images (area: 20 x 20 μm^2) recorded at different areas of the same sample. Non-parametric Mann-Whitney U t with a level of significance, α, of 0.05 was used, which reveals that the circularity, *i.e.,* the shape, of the bacteria grown on the pristine ($\mathcal{C}$ = 0.68 ± 0.04, n = 300) and the swollen samples ($\mathcal{C}$ = 0.91 ± 0.04, n = 300) is statistically different.

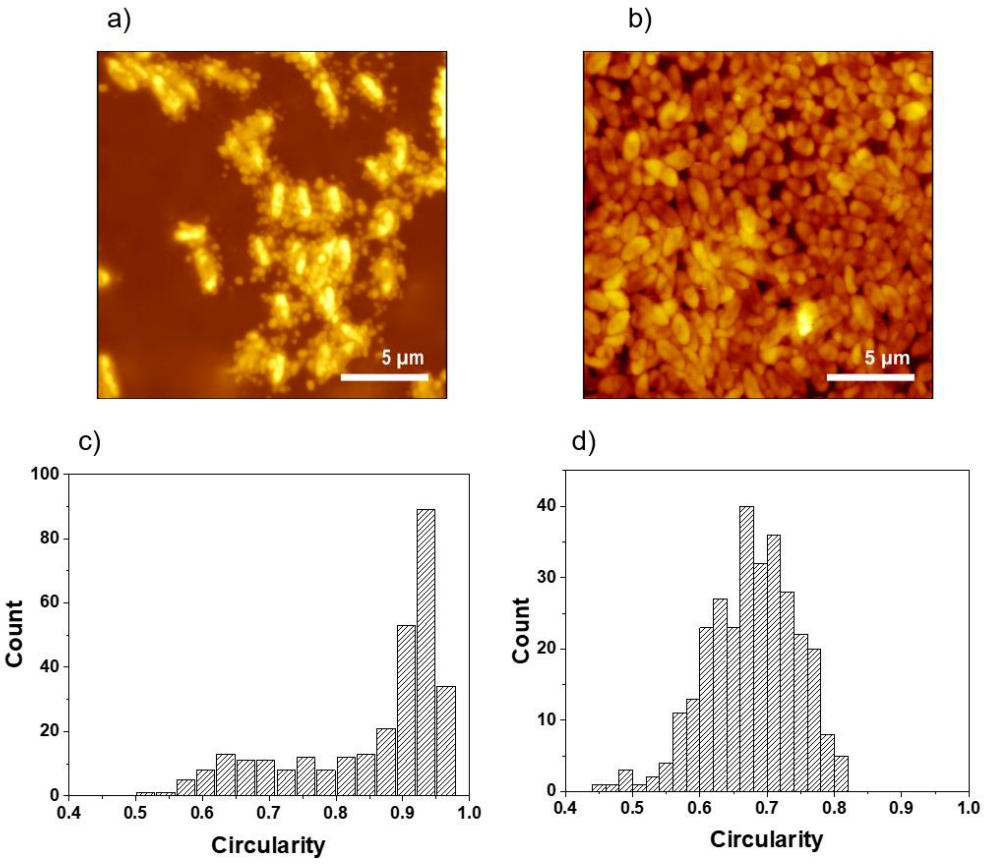

Figure 4.16. (**a, b**) Contact mode AFM topography image of *P. fluorescens* after 30 h of incubation on (**a**) a pristine sample and (**b**) a previously swollen film. Images were recorded in air. (**c, d**) Frequency counts of bacteria circularity of *P. fluorescens* after 30 h of incubation on (**c**) a pristine sample and (**d**) a pre-swollen film.

The alteration of the shape and size of bacteria is a well-known cellular response when bacteria populations are under environmental stress, such as nutritional starvation, extreme pH, and the presence of antimicrobials, and react to adapt the cell physiology to adverse conditions. For instance, it has been shown that when rod bacteria converse to

coccoidal-shaped cells, cells exhibit higher resilience against antibiotics, oxidative stress, and reducing agents [282].

The structural modification might be due to different mechanisms related to reduced energy requirements, including (*i*) alteration or partial loss of the outer membrane, (*ii*) reduction of the cell envelope, and (*iii*) alteration of the intracellular material density [283]. Hence, we assume that the morphological change of the cells grown on the pristine Ag-CF_X samples is a cellular response against the antimicrobial activity of silver(I) ions released from the Ag-CF_X film and that the presence of a layer of coccoidal cells may limit the adverse effect of the silver(I) release that allow the growing of a new layer of rod-shaped bacteria in a less hostile environment.

4.2.3. Conclusions

SECM in combination with ASV has been used to investigate the kinetics of the silver(I) ion release from a second-generation of antimicrobial nanomaterials based on AgNPs embedded in a Teflon-like matrix, Ag-CF_X. Kinetic results were correlated using the Korsmeyer-Peppas model with a *non-Fickian* transport of the silver(I) ions, influenced by the polymeric relaxation and swelling of the CF_X matrix. Data were confirmed by AFM studies in which the swelling of the fluoropolymer was quantitatively evaluated. Antimicrobial studies against *P. fluorescens* demonstrated the importance of the release of silver(I) ions as biocide active agents, associated with a higher density of bacteria and the formation of biofilms at pristine samples, in comparison to attenuated biofilm formation at pre-swollen Ag-CF_X films.

A statistical study on the shape variation of the bacterial cell was also performed, showing a transition from rod-shaped cells to smaller coccoidal-like cells when bacteria were exposed to pristine samples, where silver(I) ions release occurs during the incubation time. According to the literature, we correlate the variation of the cellular size and shape in pristine samples to the presence of the silver(I) ions and their antimicrobial effects, in comparison to swollen samples where a smaller concentration of silver(I) ions is expected and bacteria exhibit characteristic shapes and sizes of *P. fluorescens* grown in a natural non-hostile environment.

4.3. Electro-deposition of antimicrobial silver nanoparticles on polydopamine films by scanning electrochemical cell microscopy

This section describes part of collaborative studies that will be published soon as follows: Caniglia, G.; Valavanis, D.; Tezcan, G.; Barth, H.; Unwin, R. P.; Kranz, C., Electro-deposition of antimicrobial silver nanoparticles onto polydopamine films by scanning electrochemical cell microscopy (publication in preparation, 2022).

4.3.1. Introduction

Multidrug-resistant (MDR) bacteria and biofilms represent nowadays a clinical problem since conventional antibiotics and disinfectants are no longer effective to combat their proliferation at the surface of human tissues and medical implants [284–286]. The demand for the formulation of novel composites to overcome this issue has increased over the last decades and novel therapies have been employed, such as the application of antimicrobial polymers (AMPs) [141] and the implementation of engineered metallic NPs. Indeed, NPs exhibit synergistic effects due to the antimicrobial activity of the particle themselves and the antimicrobial ions released [178,232,236,287]. Recent efforts have been focused on systems, in which NPs have been conjugated with AMPs in order to enhance their antimicrobial properties. For example, AgNPs have been embedded in a variety of polymeric matrices, such as fluoropolymers [178], chitosan [288,289], textiles [290], and catecholamine-based polymers [291,292], showing promising antibacterial activity. PDA, a catecholamine-base polymer, has been presented as suitable antimicrobial films [292]. The versatility of PDA is not only due to the inherent antibiofouling activity of the polymer [162] but also to the synergistic effects of the AgNPs-PDA system in terms of antimicrobial activity [292]. Indeed, AgNPs can be easily formed *in situ* by immersing the PDA film in a dilute solution of $AgNO_3$. Due to the reductive properties of PDA that arise from the catechol groups, AgNPs can be formed through the reduction of silver(I) ions [293–295]. Even though this method has been extensively used to produce either thin film of colloidal particles of AgNPs-PDA, it is worth mentioning that this strategy can be time-consuming (12 to 24 hours) and the control of the particle size and shape might be difficult to achieve without the additional use of common reduction agents, such as $NaBH_4$ [296]. Electrochemical methods, and in particular the double-potentiostatic method, are well-established strategies that lead to a reproducible, fast, and eco-friendly synthesis of AgNPs at different conductive or semi-conductive materials. According to the literature, most of the electro-deposition of AgNPs has been performed at metallic substrates (gold and platinum) [297,298] and conducting oxides (indium tin

oxide and aluminum doped zinc oxide) [224,299,300]. However, the electrochemical deposition of AgNPs using polymeric substrates is a field still poorly explored [228,301–303]. For the fast preparation, optimization, and execution of screening experiments, AgNPs micro-spot arrays have been electrodeposited onto PDA using SECCM (see **Section 2.3**). The main advantages of SECCM arise from the possibility of forming a micro-confined electrochemical cell, which permits the study of electrochemical single events, like *e.g.,* the formation and growth of NPs. The possibility to generate also arrays of tens of spots, using SECCM hopping mode, allows the acquirement and study of large datasets in a short time. SECCM was, thus, explored in this thesis to optimize the electrochemical deposition of AgNPs on PDA thin films. Furthermore, morphological, nanomechanical, and antimicrobial characterization of the PDA-AgNPs films was obtained *via* AFM force spectroscopy.

4.3.2. Results and discussion

4.3.2.1 Electrochemical deposition of AgNPs: mechanistic investigation

A schematic of the SECCM configuration and the steps for the AgNPs electrodeposition are depicted in Figure 4.17. AgNPs have been electrodeposited on PDA with different thickness: PDA_{25} and PDA_{50} refer to PDA pulsed-deposited on gold using 25 and 50 cycles, respectively, with a potential pulse sequence of + 0.5 V / 2 s; 0.0 V / 2 s; – 0.3 V / 2 s; 0.0 V / 3 s.

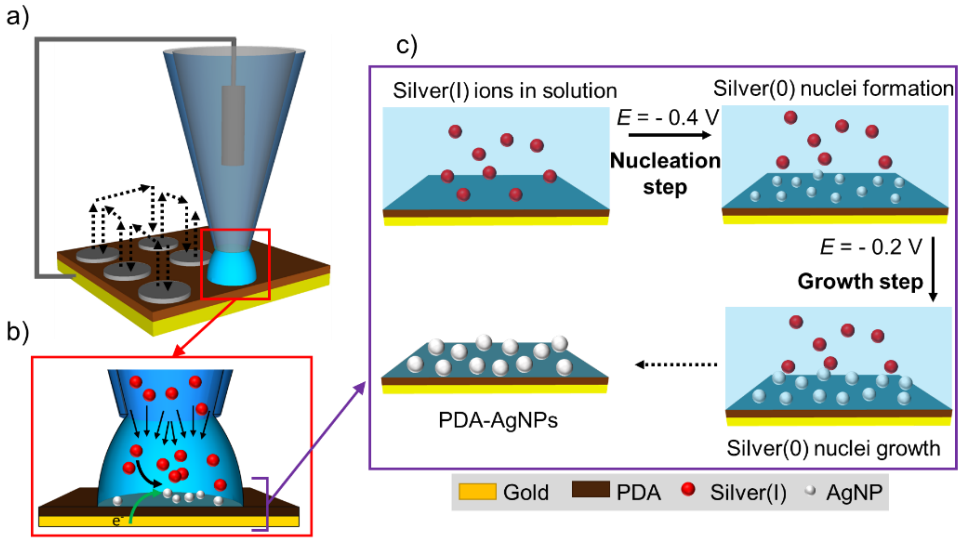

Figure 4.17. (**a**) Schematic of the SECCM setup for the AgNPs electro-deposition on PDA using a single-barrel pipette. The arrows indicate the movement of the probe across the substrate (working electrode). (**b**) Detail of the confined electrochemical cell when the pipette approaches the surface and forms a contact meniscus. (**c**) Schematic of the steps for the electro-deposition of AgNPs *via* the double-potentiostatic method.

Mechanistic analysis on the electro-deposition of AgNPs on PDA-gold substrates, and in particular on the growth of Ag-nuclei, was performed *via* the chronoamperometric transients obtained during the electro-deposition of the AgNPs on PDA_{25} starting from an $AgNO_3$ concentration equal to 5.0 mmol L^{-1}.

It is commonly accepted that the electrochemical growth of nuclei at high overpotentials is a diffusion-limited process, *i.e.,* it is limited by the diffusion of the silver(I) ions toward the electrode [304,305]. Although, recent works based on numerical modeling and theoretical simulations have revealed that the initial growth of the nuclei is always limited by the kinetics of the electrochemical reactions despite high overpotentials [231,306]. Figure 4.18a shows an exemplary chronoamperometric transient obtained during the growth of the nuclei, formed after a cathodic pulse of – 0.4 V for 0.5 s. All experiments were performed using the localized electrochemical cell formed by the contact droplet at the PDA_{25}-gold electrode.

The chronoamperometric transient depicted in Figure 4.18a can be divided into three different regions: the nuclei grow under either kinetic, mixed, or diffusion-controlled regimes. Initially, the transient follows a parabolic trend (R^2 = 0.98039), which can be observed by plotting the current respond *versus* the square root of time, as shown in Figure 4.18b, suggesting that the nuclei growth occurs under kinetic control [231]. At intermediate times, the transient follows a lineal dependency with time (Figure 4.18a, blue dotted line, R^2 = 0.98042), switching to a mixed regime growth, in which the growth of the nuclei is controlled by two events: the electroreduction of silver(I) to metallic silver and with that the deposition onto the PDA_{25}-gold substrate and the diffusion of the silver(I) ions to the surface of the PDA_{25}-gold substrate. At longer times, the transient changes to a square root relationship with time (Figure 4.18a, red dotted line, R^2 = 0.97289), which is characteristic of a diffusion-controlled regime. The transition time from mixed to diffusion controlled was equal to 630 ms, which has been derived from the intersection of the linear function with the square root function [306,307]. The obtained value of transition time is in reasonable agreement with values reported in the literature under the same experimental conditions like applied potential and silver(I) ion concentration. It reveals the presence of nuclei with starting radii of *ca.* 5 nm [231,306].

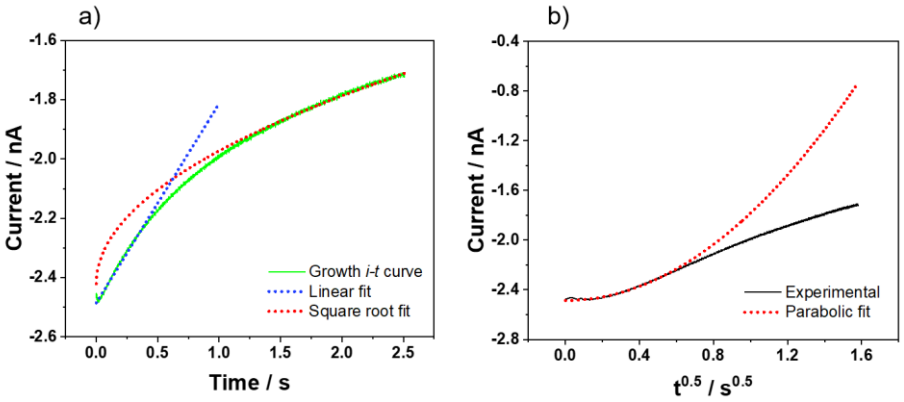

Figure 4.18. (**a**) Experimental current-time transient curve of the growth of silver nuclei (green line), linear fitting (blue dotted line), and square root fitting (red dotted line). (**b**) Experimental current-time transient of the growth of silver nuclei (black line) and parabolic fitting (red dotted line). Nuclei growth conditions: $AgNO_3$ concentration = 5.0 mmol L^{-1}, potential = – 0.2 V vs Ag/AgCl, substrate = PDA_{25}-gold.

A more detailed study of the mixed and diffusional regions of the chronoamperometric transients was performed to obtain semi-quantitative information on the nucleation and growth processes. Particularly, the diffusional process of silver(I) ions during the electrochemical deposition in relation to the geometry of the used SECCM pipette was investigated.

Since the diffusional behavior of the electrochemically active species in the SECCM configuration is similar to disk-shaped UMEs, the experimental transients have been fitted with the modified Cottrell equation for a disk UME (equation 4.8), as shown in Figure 4.19a and b [66].

$$I(t) = nFAC^*(D/\pi t)^{0.5} + 4nFAC^*D/\pi r \quad (4.8)$$

Here, A and r are the effective area and radius of the UME, respectively; D is the diffusion coefficient of silver(I) ions (1.7 x 10^{-9} m^2 s^{-1} [308]) and C^* is the concentration of silver(I) in bulk solution. For the analysis, the effective area, A, and the steady-state mass transport coefficient, $m = 4D/\pi r$, were used as fitting parameters. For the nucleation process (Figure 4.19a), the obtained effective area was equal to A = 15.0 ± 0.7 μm^2 (n = 10) and for the growth process, A = 17.6 ± 0.6 μm^2 (n = 10), which correspond to diameters of a = 4.4 ± 0.1 µm (n = 10) and a = 4.73 ± 0.08 µm (n = 10), respectively. These values are in accordance with the orifice diameter of the pipettes used (*ca.* 5 µm) for the electrodeposition. The steady-state mass transport coefficient obtained from the fitting (*ca.* 0.003 cm s^{-1} for both processes) was approximately one order of magnitude lower than expected from a pipette with a radius equal to 5 µm; this value corresponds to

a characteristic inner pipette half-cone angle of 8° [309,310]. The conical geometry of the SECCM pipette suggests a trend of the system to follow a mixed diffusion between a semi-infinitive linear diffusion (given by the first term of equation 4.8) and a hemispherical diffusion. This behavior is also visible by plotting the normalized current (I/I_{ss} where $I_{ss} = 4nFDC^{*}r$ for a disk UME [311]) *vs* the dimensionless time parameter defined as $\tau = 4Dt/r^2$ and comparing the experimental curve with the current that would be observed by the Cottrell relation.

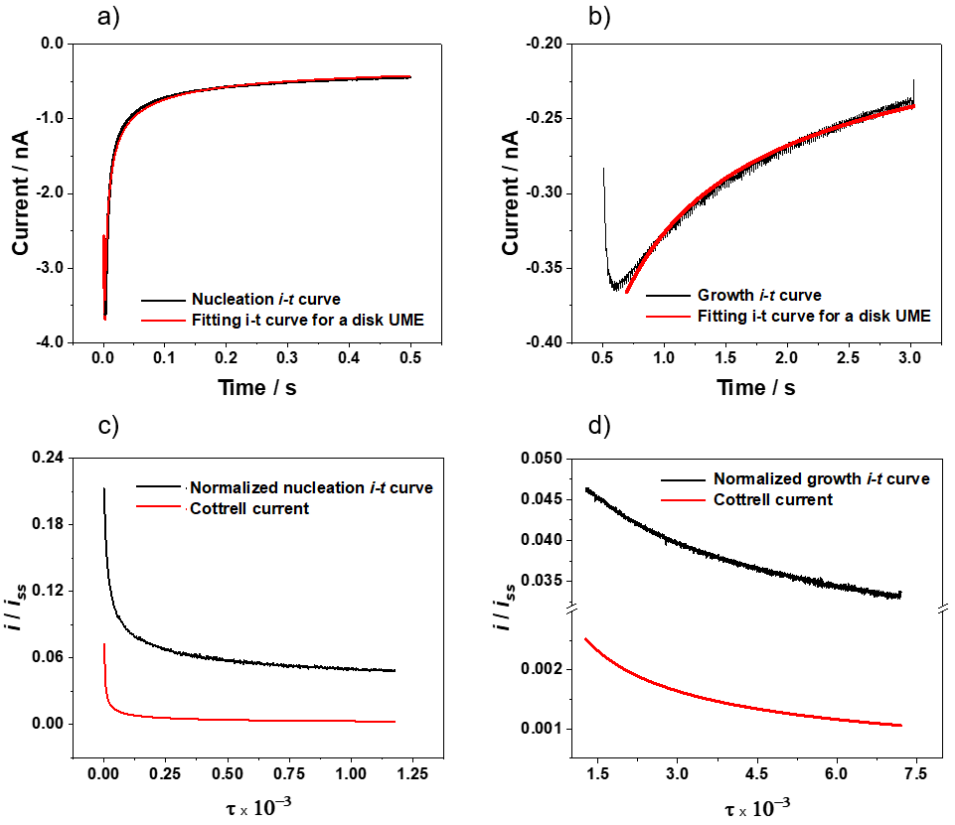

Figure 4.19. (**a, b**) Current transient (red line) and fitted curve using equation 4.8 (black line) for the (**a**) nucleation step and (**b**) growth step of the AgNPs on PDA_{25}-gold substrates. (**c, d**) Normalized current transient (red line) and corresponding Cottrell current (black line) for (**c**) the nucleation step and (**d**) the growth step of the AgNPs on PDA_{25}-gold substrates. Current is expressed as i/i_{ss} and time as τ.

As shown in Figure 4.19c and d, the diffusion of the silver(I) ions during the SECCM experiments is not purely semi-infinitive linear, since the experimental transient exhibits a larger normalized current in comparison to a pure Cottrell current. These findings suggest that the diffusion of the silver(I) ion during the electro-deposition of the AgNPs exhibits a quasi-radial character [81]. This diffusional model assumes that the concentration of silver(I) species is higher in the center of the electrochemical cell formed

by the micropipette and lower at the boundaries, with the consequent formation of smaller AgNPs at the edges of the electrochemical cell. Indeed, a statistical ANOVA study (α = 0.05) based on the measurement of more than 150 NPs in the center and at the edge of the spot (Figure 4.20a) shows a significant difference in diameter. Particles grown on the edge exhibit an averaged diameter equal to 47 ± 2 nm and AgNPs grown in the center present an averaged diameter of 64 ± 4 nm, as shown in the distribution plot depicted in Figure 4.20b and the bar chart in Figure 4.20c.

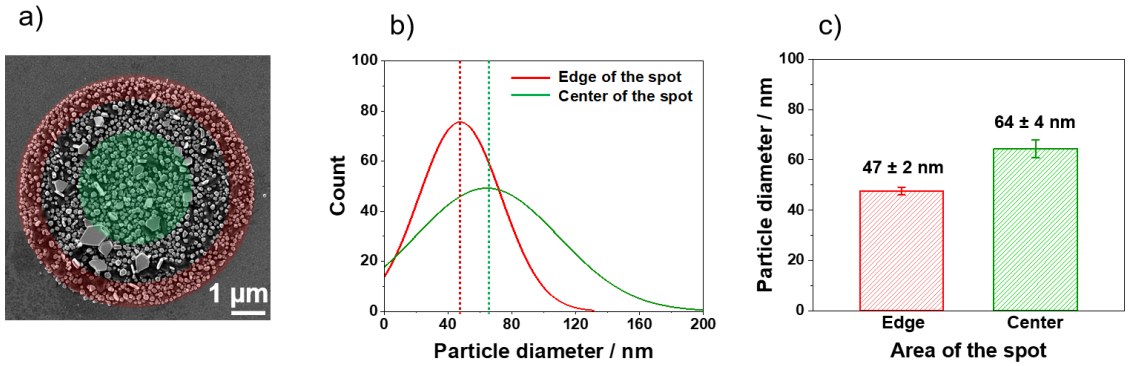

Figure 4.20. (**a**) SEM images (false color image) of an AgNPs spot obtained by electrochemical deposition using 0.05 mmol L^{-1} $AgNO_3$, a nucleation potential of – 0.4 V (for 0.5 s), and growth potential of – 0.2 V (for 2.5 s). The AgNPs at the edge and the center of the spot are highlighted in red and green. (**b**) Size distribution of the AgNPs grown at the edge (red line) and the center (green line) of the localized microelectrochemical cell. (**c**) Bar chart of the AgNPs diameter. Error bars reflect the measurement of at least 150 NPs.

4.3.2.2 Electrochemical deposition of AgNPs: optimization

SECCM is highly suitable to optimize the electro-deposition of AgNPs on PDA with respect to the experimental factors (or variables) that could influence the size and shape distribution of the NPs, as arrays of AgNPs using different parameters can be deposited at the same sample. By this approach, the time for optimization can be significantly reduced and uncertainties related to variations of the substrate (*i.e.*, PDA deposition) can be eliminated. Optimization variables include nucleation and growth potential, nucleation and growth time, promoter concentration, and polymer thickness. Since the optimization of the applied potentials has been already performed in previous works [224,299], the nucleation potential at t_n = – 0.4 V and the growth potential at t_g = – 0.2 V were fixed for all presented experiments. The optimization of the AgNPs electro-deposition involves a two-factor/three-levels factorial design, *i.e.,* three different precursor concentrations ($AgNO_3$ 5.00 mmol L^{-1}, 0.50 mmol L^{-1}, and 0.05 mmol L^{-1}) and three different deposition times (being t_n x t_g: 0.0 x 4.0 s; 0.5 x 3.5 s, and 0.5 x 2.5 s) were investigated. Table 4.1

summarizes the parameters used for the electro-deposition of AgNPs and the obtained corresponding averaged particle diameter, while Figure 4.21 shows representative SEM images of the AgNPs spots electrodeposited by varying the different parameters.

Table 4.1. Average particle diameter as a function of the $AgNO_3$ concentration, nucleation time, and growth time. Nucleation and growth potentials have been kept constant (– 0.4 V and – 0.2 V, respectively).

$AgNO_3$ Concentration mmol L^{-1}	**Nucleation time s**	**Growth time s**	**AgNPs diameter nm [a]**
5.00	0.0	4.0	171 ± 4 [b]
5.00	0.5	3.5	77 ± 2
5.00	0.5	2.5	55 ± 1
0.50	0.0	4.0	159 ± 11 [c]
0.50	0.5	3.5	25.5 ± 0.3
0.50	0.5	2.5	18.5 ± 0.2
0.05	0.0	4.0	22.4 ± 0.7
0.05	0.5	3.5	17.6 ± 0.4
0.05	0.5	2.5	8.74 ± 0.08

[a] n > 650 AgNPs
[b] n = 100 AgNPs
[c] n = 135 AgNPs

Figure 4.21a displays an SEM image of the AgNPs electrodeposited without the application of a nucleation potential (t_n = 0 s) and with a concentration of $AgNO_3$ equal to 5.0 mmol L^{-1}. The NPs exhibit multiple shapes (truncated tetrahedral, dendritic, octahedral, and truncated tetrahedral) and an averaged particle size of 171 ± 4 nm (n = 100). The particle size was evaluated without considering the largest truncated tetrahedral-shaped particles (double-hexagon apothem = 455 ± 1 nm, n = 40). The AgNPs obtained without a nucleation pulse were compared with the AgNPs depicted in Figure 4.21b, where the total electro-deposition time was equal to the time of AgNP deposition depicted in Figure 4.21a (t_{dep} = 4.0 s), but split into a nucleation pulse of 0.5 s and a growth pulse for 3.5 s. It is evident that a short nucleation pulse results in more uniform particle sizes and distribution. Indeed, the particles shown in Figure 4.21b grew more homogenously over the entire surface. However, the relatively long growth potential also favors the formation of larger truncated twinned tetrahedral AgNPs with an average size equal to 429 ± 0.06 nm (calculated as the double apothem of the hexagonal particle, n = 9). The (111) facets of the truncated tetrahedra are highlighted in red in Figure 4.21b. By maintaining a constant precursor concentration of 5.0 mmol L^{-1} and a nucleation pulse of 0.4 s, the particle size decreases significantly from 77 ± 2 nm (n = 501) to 55 ± 1 (n = 492) when decreasing the growth time to 1 s (Figure 4.21b and c).

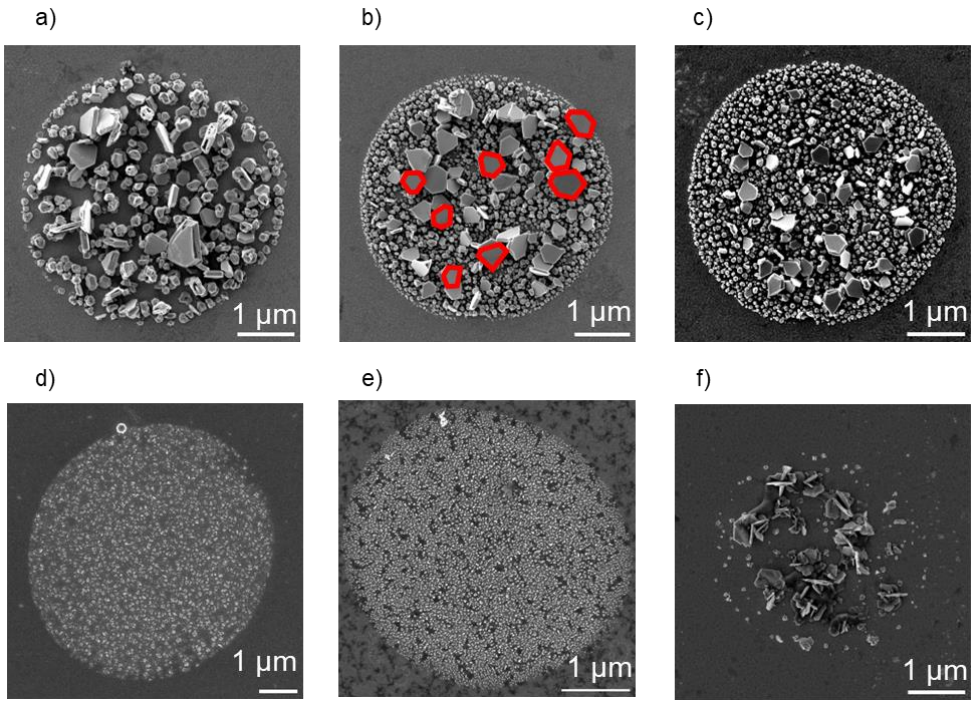

Figure 4.21. Representative SEM images of AgNP spots obtained *via* SECCM using pipettes with a diameter of *ca*. 5 µm. Nucleation and growth potential were kept constant (E_n = – 0.4 V and E_g = – 0.2 V vs. Ag/AgCl). (**a**) [$AgNO_3$] = 5.0 mmol L^{-1}, t_n = 0 s, t_g = 4.0 s; substrate PDA_{25}; (**b**) [$AgNO_3$] = 5.0 mmol L^{-1}, t_n = 0.5 s, t_g = 3.5 s; substrate PDA_{25}; (**c**) [$AgNO_3$] = 5.0 mmol L^{-1}, t_n = 0.5 s, t_g = 2.5 s; substrate PDA_{25}; (**d**) [$AgNO_3$] = 0.5 mmol L^{-1}, t_n = 0.5 s, t_g = 2.5 s; substrate PDA_{25}; (**e**) [$AgNO_3$] = 0.05 mmol L^{-1}, t_n = 0.5 s, t_g = 2.5 s; substrate PDA_{25}; (**f**) [$AgNO_3$] = 5.0 mmol L^{-1}, t_n = 0.5 s, t_g = 2.5 s; substrate PDA_{50}.

At lower silver(I) ion concentrations, *i.e.,* 0.50 mmol L^{-1} (Figure 4.21d) and 0.05 mmol L^{-1} (Figure 4.21e), the particle size decreases, and AgNPs grew homogeneously in size and shape, due to the lower concentration of electroactive species. As shown in Table 4.1, the particle size distribution at different $AgNO_3$ concentrations drops to 18.5 ± 0.02 nm (0.5 mmol L^{-1}, n = 1012) and 8.7 ± 8 nm (0.05 mmol L^{-1}, n = 1748). These depositions were carried out at a nucleation and growth time of 0.5 s and 2.5 s, respectively.

The influence of the thickness of PDA on the electro-deposition of AgNPs was also investigated by electro-depositing AgNPs on PDA_{25} and PDA_{50}. Figure 4.21c and f show the electro-deposition of AgNPs on PDA_{25} (~1 nm thickness) and PDA_{50} (~3 nm thickness) [154], respectively, keeping all the other experimental conditions constant, *i.e.*, $AgNO_3$ concentration 5.0 mmol L^{-1}; nucleation time 0.5 s (– 0.4 V); growth time 2.5 s (– 0.2 V). As shown in Figure 4.21f, the electro-deposition of AgNPs onto a thicker polymeric layer (PDA_{50}) was not favorable, with the formation of small dispersed nuclei and larger

polyhedral and dendritic-shaped AgNPs. The imperfect electro-deposition of AgNPs onto PDA_{50} might be due to a decreased electron transfer rate, as reported by Kund et al. [154] *via* SECM measurements.

4.3.2.3 Antimicrobial study of the PDA-AgNPs system

To investigate the antimicrobial properties of the synthesized AgNPs-PDA microstructured surface, the behavior of the bacteria *E. coli* in the early stage of cell attachment was studied in terms of cell morphology, adhesion forces, and elasticity using AFM and AFM-based force spectroscopy. The advantage of using AFM-based techniques for the investigation of the bacterial behavior is the possibility to perform studies down to the single-cell level on bacteria exposed to different conditions, *i.e*., at a different distance from the source of antimicrobials (AgNPs spots). Since a single bacterial culture batch has been used in these studies, heterogeneities, and uncertainties due to different inoculation cultures have been avoided.

Since the AgNPs have been deposited *via* an electrochemical method in electrolytic solutions without any capping agent, it is expected that the AgNPs are nuclei of metallic silver forming stable complexes with the quinone functional groups of PDA [312]. However, the coordination with PDA might not be enough to favor the spontaneous oxidative dissolution of the AgNPs to release silver(I) ions, which antimicrobial effects increase synergistically the activity of the NPs themselves [313]. To overcome this drawback, the PDA_{25}-AgNPs samples were treated with UV-ozone for 30 min to oxidize the metallic silver to silver oxide. It has been demonstrated that the presence of a layer of silver oxide around the metallic AgNPs generates the thermodynamically favorable dissolution of the oxide with the release of the silver(I) ions and, at the same time, it triggers the dissolution of the metallic NPs [239,314].

The antimicrobial activity of the AgNPs was tested using the particles obtained with the following parameters: (*i*) concentration of $AgNO_3$ of 0.5 mmol L^{-1}; (*ii*) nucleation potential equal to – 0.4 V vs. Ag/AgCl applied for 0.5 s, and (*iii*) growth potential equal to – 0.2 V vs. Ag/AgCl applied for 2.5 s. Under these conditions, a particle size (before the UV-ozone treatment) of 18.5 ± 0.02 nm (n = 1012) was obtained. This size of AgNPs fits the optimal range since it has been demonstrated that AgNPs between 10 and 50 nm exhibit increased stability, biocompatibility, and enhanced antimicrobial activity [201]. As shown in Figure 4.22, due to the formation of a thin oxide layer around the NPs after the UV-ozone treatment, the size of the particles increased, reaching a diameter more than 45% larger (see Figure 4.22d and d) in comparison with the untreated particles.

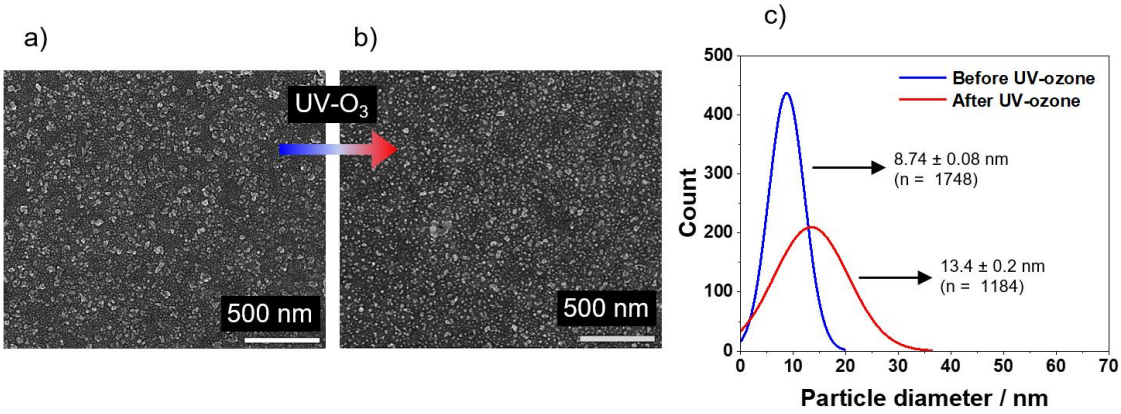

Figure 4.22. Representative SEM images of AgNPs (**a**) before and (**b**) after UV-ozone treatment. (**c**) Size distribution of the AgNPs before (blue line) and after (red line) the treatment with UV-ozone. The NPs were deposited on PDA_{25} with the following parameters: E_n = – 0.4 V, E_g = – 0.2 V vs. Ag/AgCl, t_n = 0.5 s, t_g = 2.5 s, and [$AgNO_3$] = 0.5 mmol L^{-1}.

To understand the effect of the oxidized AgNPs, morphological and nanomechanical studies *via* AFM and AFM-based force spectroscopy were performed on single bacterial cells of *E. coli* inoculated on the UV-ozone treated (for 30 min) AgNPs-PDA_{25} samples. As shown in Figure 4.23a and b, isolated bacteria can attach in the proximity of the AgNPs spot (distance of a few µm), while at larger distances from the AgNPs, where the concentration of silver(I) ions released is expected at a lower rate, bacteria grow as small communities of tens of cells.

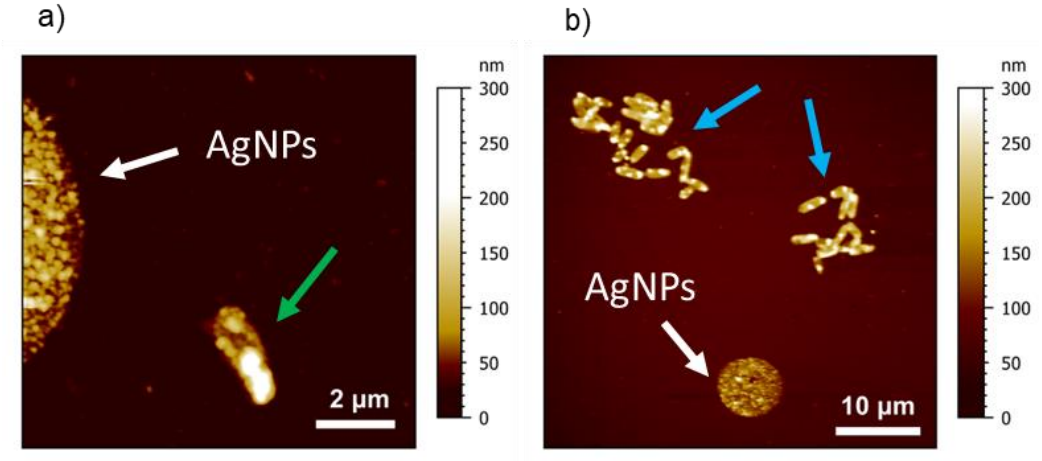

Figure 4.23. AFM topography images recorded in air of *E. coli* inoculated at the PDA_{25}-AgNP spot. (**a**) Single-cell (green arrow) attached in the proximity of the AgNPs spot. (**b**) Overview of small communities of bacteria (blue arrow) attached at more than 20 µm from the AgNPs spot.

High-resolution AFM images displayed in Figure 4.24a and c, however, clearly show that bacteria attached at a short distance from the AgNPs spot, exhibit changes in

their morphology with reduced cell size. This behavior has been already observed in other gram-negative bacterial strains in contact with silver(I) ions [178] or hostile environments [283]. Figure 4.24c also reveals the appearance of corrugations and grooves on the cell surface, which can be correlated to the disruption of the outer membrane (OM) due to the exposure to silver(I) ions released from the AgNPs spot. The cell membrane deformation is also exemplarily represented by the transverse and longitudinal cross-sections of a *healthy* bacterium (Figure 4.24b) and an *ill* bacterium (Figure 4.24d).

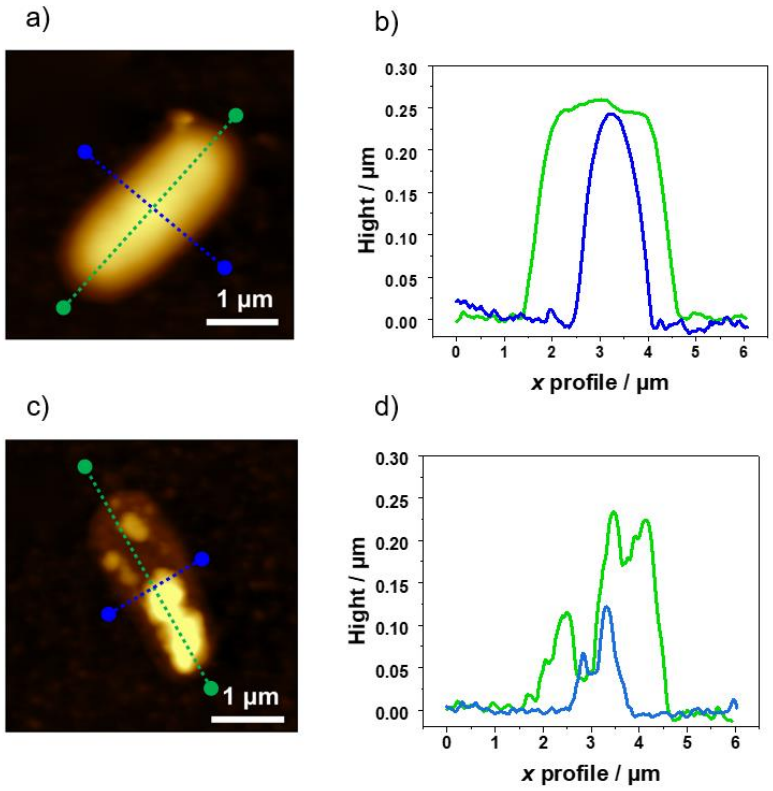

Figure 4.24. (**a-c**) AFM topography images recorded in air of *E. coli* (**a**) attached more than 20 µm from the AgNPs spot and (**c**) attached in the proximity (*ca*. 2 µm) of the AgNPs spot. (**b-d**) Longitudinal (green line) and transversal (blue line) cross-sections of *E. coli* corresponding to (**b**) Figure 4.24a and (**d**) Figure 4.24c.

The deformation of the OM due to the activity of the silver(I) ions and AgNPs might change also the nanomechanical properties of the bacterial cell. It is well-known that one of the antimicrobial pathways of the AgNPs and silver(I) ions derives from the high affinity of silver with sulfur-containing proteins [201]. Two of the most important sulfur-containing protein of *E. coli* are the so-called RcsF and Nlpe [315]. These are OM-lipoproteins which main function is to preserve the integrity of the OM. Even though the interaction mechanism of AgNPs with RcsF and Nlpe is still not well studied, it has been shown that

the inactivation or alteration of these lipoproteins *e.g.*, by antimicrobials, leads to the inhibition of the peptidoglycan synthesis and production of capsular oligosaccharides that results in the deformation or disruption of the OM. These changes in the conformation and composition of the OM, might affect both the hydrophobicity and the stiffness of the bacterial OM. To prove this hypothesis, the adhesion force and Young´s modulus of bacteria grown at tens of micrometers away (Figure 4.23a) and in proximity (Figure 4.23b) of the AgNPs spots were investigated.

Force-distance curves recorded on cells attached in the proximity of the AgNPs spots revealed lower adhesions forces (0.41 ± 0.03 nN, n = 450) in comparison to cells grown at a distance larger than 20 µm from the spots (1.2 ± 0.1 nN, n = 430), as shown in Figure 4.25a. This change in adhesion is attributed to an increase in the hydrophilicity of the cellular OM for cells in close proximity to the AgNPs. This behavior might be due to the change in the OM composition produced by the AgNPs and the silver(I) ions released from the NPs. It is generally accepted that the hydrophilicity of *E. coli* arises from the contribution of the hydrophilic C-O and C-N functional groups associated with polysaccharides and the C-C and C-H hydrophobic functional groups of hydrocarbons [316]. However, when AgNPs and silver(I) ions interact with the OM of *E. coli*, they might affect sulfur-containing membrane lipoproteins that control the integrity of the outer membrane [201,315]. When perturbed, these lipoproteins modulate the formation of higher amounts of capsular oligosaccharides to stabilize the cell membrane [315]. Due to the presence of a higher concentration of oligosaccharides with hydrophilic character, an increase in the hydrophilicity of the bacterial cell is expected, which is clearly visible as a drop in adhesion forces.

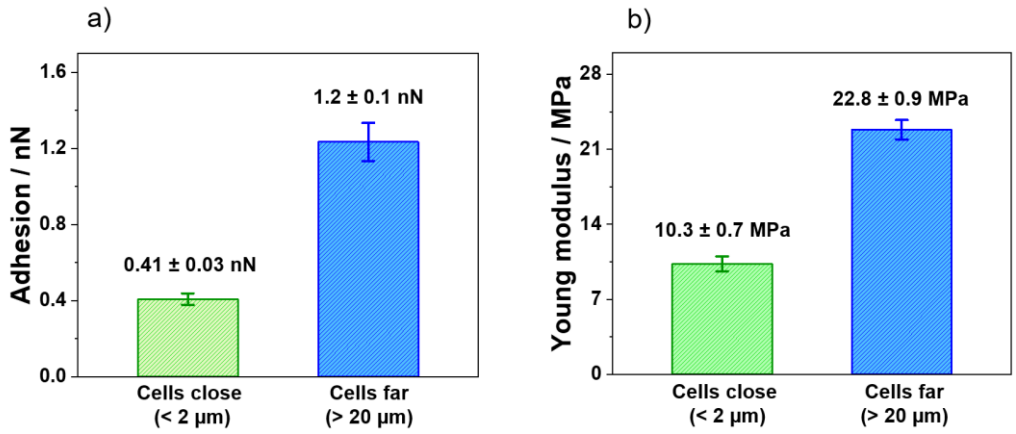

Figure 4.25. Bar charts of the measured (**a**) adhesion forces and (**b**) Young´s modulus. Error bars reflect the measurements of at least 9 cells and 430 force curves.

The results correlated to the elasticity (Figure 4.25b) of the bacteria are in accordance with the assumption that the cells directly exposed to AgNPs experience an alteration and disruption of the OM. The elasticity was correlated to Young´s modulus (E_S), calculated from the force-distance curves, using the Hertz model for fitting [61,109]. The cells close to the AgNPs are less stiff (E_S = 10.3 ± 0.7 MPa, n = 454) than the cells away from the spots by more than 20 µm (E_S = 22.8 ± 0.9 MPa, n = 448). Recent studies [317] showed that bacteria grown in healthy conditions exhibit stiff OM due to the presence of structural molecules such as lipopolysaccharides and that the integrity and rigidity of the membrane are directly correlated to the cell mechano-sensitivity: *i.e.,* a tension sensor that plays an important role in the osmoregulation of the bacteria. Accordingly, it has been proposed [318,319] that one of the contributions of the OM stiffness is due to the ionic bonds between lipopolysaccharides and that the interaction of their negatively charged moieties with cationic ions disrupts these bonds, leading to an alteration of the lipid packing and thus a decrease in stiffness [320]. A loss of rigidity in cells exposed to AgNPs and silver(I) ions might be related to the interaction and chelation of silver with the lipopolysaccharides and the consequent rupture of the lipidic ionic bonds, OM corrugation, and cell lysis.

4.3.3. Conclusions

SECCM was employed for the deposition of antimicrobial AgNPs on PDA using a double-potentiostatic method. A mechanistic study on the AgNPs growth has been conducted, suggesting that the growth of metallic silver nuclei depends, in the early stages, on the kinetics of the reduction reaction from silver(I) ion to metallic silver and that it is not only a diffusion-controlled process. To test the microstructured AgNPs-PDA films as antimicrobial films, the electro-deposition of AgNPs has been optimized to obtain reproducible AgNPs with sizes and shapes suitable for achieving a high antimicrobial effect. The influence of parameters such as nucleation time, growth time, and $AgNO_3$ concentration have been investigated. For this purpose, SECCM has been employed as it enables the fast acquisition of large data sets, due to the possibility of generating arrays of tens of spots in different experimental conditions. The optimized protocol leads to a particle size of 18.5 ± 0.02 nm (n = 1000), by applying a nucleation potential of – 0.4 V (*vs* Ag/AgCl) for 0.5 s, a growth potential of – 0.2 V (*vs* Ag/AgCl) and using a concentration of $AgNO_3$ equal to 0.5 mmol L^{-1}. The antimicrobial activity of the ozone-treated AgNPs-PDA system has been evaluated against *E. coli* in terms of adhesion and elasticity properties, revealing that the envelope of *E. coli* exhibits enhanced hydrophilicity and lose of stiffness when bacteria are in close proximity to the AgNPs.

5 EXPERIMENTAL SECTION

5.1. Atomic force microscopy and infrared spectroscopic studies on the role of surface charge for the anti-biofouling properties of polydopamine films: Chapter 3.3

5.1.1. Materials and chemicals

All solutions were freshly prepared in ultrapure water from a Millipore Milli-Q system (resistivity: 18.0 MΩ cm at 25°C). Ferrocene-methanol, sodium hydrogen phosphate (Na_2HPO_4), sodium dihydrogen phosphate (NaH_2PO_4), sodium chloride (NaCl), potassium chloride (KCl), hydrochloric acid (HCl), sodium hydroxide (NaOH), and potassium hydroxide (KOH) were purchased from Merck (Germany). Luria-Bertani (LB) culture medium was purchased from VWR International GmbH (Germany) and dopamine hydrochloride was purchased from Sigma-Aldrich (Germany). 2 cm x 2 cm gold substrates were prepared by sputter coating on silicon wafers and cleaned in acetone, isopropanol, and deionized water, prior to use.

5.1.2. Electrochemical deposition of polydopamine

The electrochemical deposition of e-PDA was performed using a CHI842B bipotentiostat (CH Instruments, USA) in a three-electrode cell with an Ag/AgCl/KCl (sat.)

reference electrode, a platinum counter electrode, and the gold-coated substrate as a working electrode. All the potentials in this section are reported *vs* the Ag/AgCl/KCl (sat.) reference electrode. The deposition was conducted *via* electrochemical pulsed-deposition [153,154] by applying 100 pulse cycles at the gold working electrode with a potential pulse sequence of + 0.5 V / 2 s; 0.0 V / 2 s; – 0.3 V / 2 s; 0.0 V / 3 s in an oxygen-free (purged with N_2 for 15 min) electrolytic solution containing 5.3 mmol L^{-1} dopamine hypochlorite in 10 mmol L^{-1} PBS (pH 7.4). After the deposition, the e-PDA was electro-oxidized by applying a potential of + 0.5 V for 300 s in a solution of 10 mmol L^{-1} PBS.

5.1.3. Bacterial culture conditions

Cultures of E. coli DH5-α were prepared by inoculating in 25 g L^{-1} sterile LB medium at 37 ± 1 °C until reaching an optical density of OD_{600} = 0.9, which correspond to a concentration of 10^8 CFU mL^{-1}. The OD600 was monitored using a UV-VIS spectrometer (Thermo Scientific NanoDrop One, Massachusetts, USA). The bacteria suspension was then harvested and resuspended in 0.5 g L^{-1} LB medium with different pH, in a range of pH 5 to 7. The pH of the LB medium was adjusted by adding dilute HCl or NaOH and determined using a pH meter (827 pH Lab, Metrohm, Switzerland). The bacterial culture was then seeded on the e-PDA substrates by immersing them into the bacterial solution and incubating at 37 ± 1 ºC for 16 h, using a shaking incubator (KS 4000ic control, Keison Products, United Kingdom).

5.1.4. AFM and AFM force spectroscopy experiments

All the AFM experiments were performed using a 5500 AFM/SPM instrument (Keysight Technologies, AZ, USA) equipped with a close-loop scanner. AFM contact mode images were acquired in air at a scan rate of 0.64 ln s^{-1} using silicon nitride probes (MLCT, Bruker AFM probes, CA, USA; nominal spring constant of 0.1 N m^{-1}). For the imaging experiments, the inoculated e-PDA samples were rinsed twice with LB medium, MilliQ water, and air-dried. AFM force spectroscopy was conducted in solution using silicon nitride probes (MLCT, Bruker AFM probes, CA, USA; tip radius of 20 nm and nominal constant of 0.1 or 0.6 N m^{-1}, respectively) with a leading force of 200 nN. A sweep rate of 1.0 µm s^{-1} was applied to minimize hydrodynamic effects. The force constants of the cantilevers were determined using the thermal noise method [321]. The inoculated samples studied by AFM force spectroscopy were rinsed with LB medium, and MilliQ water, prior to the force-curves being recorded in 10 mmol L^{-1} PBS solution (pH = 7.4). For the surface charge density measurements, the AFM probes were treated with UV-ozone, prior to each experiment. Statistical analyses are based on the Student t-test

assuming unequal variance. Data evaluation was performed using MoutainSPIP v. 9 (Digital Surf, France) and OriginPro 2021 software, v 9.8.0.200 (Origin Lab Corporation).

5.1.5. ATR-FTIR experiments

ATR-FTIR experiments were conducted with a Fourier-transform infrared (FTIR) spectrometer (Alpha II, Bruker Optics GmbH, Germany) equipped with an ATR assembly (Platinum ATR, Bruker Optics GmbH, Germany) which provides a single-bounce diamond crystal serving as an internal reflecting element (IRE). All the inoculated e-PDA samples were rinsed twice with LB medium and MiliQ-water. For each e-PDA sample inoculated, a corresponding pristine e-PDA sample only immersed in LB medium was recorded as the background spectrum. The IR-spectra were recorded at a spectral resolution of 2 cm^{-1} averaging 64 scans using the OPUS software package (Bruker Optics GmbH, Germany). Data evaluation was performed using a 7-point FFT filter (Origin 2019b, OriginLab) and no baseline correction was applied.

5.2. Silver-fluoropolymer (Ag-CFX) films: Kinetic study of silver release, and spectroscopic-microscopic insight into the inhibition of P. fluorescens biofilm formation: Chapter 4.2

5.2.1. Materials and chemicals

All solutions were freshly prepared with deionized water (18.0 MΩ cm, Elga Labwater; VWR Deutschland, Germany). PBS solution (0.1 mol L^{-1}, pH 6.8) and nitric acid (HNO_3) were purchased from Sigma-Aldrich (Germany). Potassium nitrate (KNO_3), silver nitrate ($AgNO_3$), and ferrocene methanol were purchased from Merck (Germany), and Luria-Bertami (LB) culture medium from VWR International GmbH (Germany). The PTFE and silver targets (purity 99.999%) for the ion beam sputtering deposition were purchased, respectively from GoodFellow LTD (Germany) and Gambetti-CERAC (Italy), and the silicon substrates (<110> 300 µm, undoped, single-side polished) from Silicon Materials (SiMat, Germany).

5.2.2. Synthesis and characterization of Ag-CF_X films

The Ag-CF_X nanocomposite was deposited on silicon substrates by co-sputtering a PTFE target and a pure silver target with argon ion beams, at room temperatures and a pressure of 10^{-2} Pa. The deposition was assisted with a second low-energy ion beam focused on the silicon substrate, fluxing O_2 at 3 cm^3_{STP} min^{-1}. The silver leading fraction was maintained at φ = 0.25. NPs size distribution and the Ag-CF_X morphology were investigated by transmission electron microscopy (TEM), using an FEI Tecnai T12

microscope (Eindhoven, The Netherlands) applying a voltage of 120 kV. For TEM analysis, the AgNPs films were previously deposited on 300 mesh carbon-coated copper grids. X-ray photoelectron spectroscopy (XPS) analysis was performed using a PHI Versaprobe II spectrometer (Chanhassen, Minnesota, USA), with monochromatized Al-Kα radiation (1486.6 eV). Spectra were recorded in constant analyzer energy mode using a pass energy of 150 eV for a survey and 100 eV for high-resolution regions (F1s, C1s, O1s, Ag3d, and AgMNN). Calibration of the binding energy (BE) scale was performed by taking as reference the C1s signal of the CF2 component, related to the polymer backbone (BE = 291.8 eV). Data analysis and curve-fit procedures were performed using Avantage v. 4.75 (Thermo Fisher).

5.2.3. Kinetics of silver(I) ion release

The quantification and kinetics of silver(I) ion released from the Ag-CF_X samples was investigated using bulk methods (electrochemical atomic absorption) and local methods (SECM).

Electrochemical atomic absorption (ETAAS). Bulk measurements of silver(I) release were performed by immersing a 2 cm x 2 cm Ag-CF_X sample in 500 µL of PBS buffer (0.1 mol L^{-1}, pH 6.8) for defined sampling times up to 48 h. For the ETAAS analysis, 50-µL aliquots of the solution in contact with the Ag-CF_X substrate were sampled at different times, diluted with 0.2% HNO_3, and analyzed in a PerkinElmer PinnAAcle AS 900Z double-beam spectrometer (PerkinElmer, Milan, Italy), equipped with a silver hollow cathode lamp, a longitudinal Zeeman system, and a transversely heated graphite tube. Prior to the release study, calibration curves were performed analyzing dilutions of a silver standard with a concentration of 1000 µg mL^{-1} in 0%.2 HNO_3. Data analysis and processing were performed by OriginPro 2016 software V 9.3 (Origin Lab Corporation).

Scanning electrochemical microscopy (SECM). Spatially resolved experiments were performed using a home-built SECM setup equipped with a CHI842B potentiostat (CH Instruments, Austin, TX, USA). The electrochemical cell consists of a three-electrode setup with a platinum (Pt) counter electrode (CE), an Ag/AgCl/KCl (sat.) reference electrode (RE), and a Pt disk UME with a nominal radius of 12.5 µm serving as working electrode (WE). Pt UMEs used in this work were fabricated according to well-established procedures [322], sealing a 12.5 µm radius Pt wire (Goodfellow, Bad Nauheim, Germany) in a borosilicate glass capillary (Hilgenberg GmbH, Mansfeld, Germany). UMEs with RG ratios in the range of 10^{-12} were characterized by cyclic voltammetry in 1 mmol L^{-1} ferrocene methanol / 0.1 M KCl. The Pt UME was placed above the Ag-CF_X substrate, and all the experiments were performed in a 0.1 KNO_3 solution and at a tip-surface

distance equal to 79 µm. The tip-surface distance was determined *via* feedback mode SECM approach curves, using oxygen as electroactive species. ASV/SWV was used to determine the concentration of silver(I) ions released over time. The ASV pre-concentration step consisted of a pulse at – 0.2 V *vs* Ag/AgCl/KCl (sat.) applied for 120 s to reduce and deposit silver(I) ions onto the UME surface. The stripping ASWV step was performed at a frequency of 25 Hz, 2 mV increments, and 25 mV amplitude, resulting in a scan rate equal to 0.05 V s^{-1}. The concentration of the silver(I) was obtained from the area of the peaks in the potential range of – 0.2 to 0.9 V. Prior to silver(I) ions release studies, calibration curves were recorded in $AgNO_3$ standard solutions (stock solution 100 µM) using 0.1 M KNO_3 as electrolyte. The limits of the detection (LOD) and quantification (LOQ) were calculated based on the standard deviation of the response (S_y) of the calibration curve and the slope (S), according to the following formulas: $\mathrm{LOD} = 3\,(S_y/S)$ and $\mathrm{LOQ} = 10\,(S_y/S)$. Data evaluation was performed using Mira software (G. Wittstock, University Oldenburg, Oldenburg, Germany) and OriginPro 2019b software, V 9.6.5.169 (Origin Lab Corporation).

5.2.4. Swelling study *via* AFM

Swelling studies of the Ag-CF_X samples were performed by monitoring the changing in height of the polymeric film. For this end, the film was removed using two different approaches: (*i*) by patterning the sample *via* focused ion beam (FIB) milling (DualBeam Helios Nanolab 600, ThermoFisher Scientific, Eindhoven, NL) using an acceleration voltage of 30.0 kV and a milling current of 0.3 nA and (*ii*) by mechanically removing the film (forming a scratch). The patterned/scratched Ag-CF_X samples were then placed in a liquid cell of the AFM setup, immersed in either MilliQ water or PBS solution (0.1 mol L^{-1}, pH 6.8), and imaged at different immersion times at the same location. Images were acquired using a Keysight AFM system Model 5500 (Keysight Technologies, AZ, USA) in contact mode AFM with a scan rate of 0.75 ln s^{-1}. Silicon nitride probes (ORC8, Bruker AFM probes, CA, USA; nominal spring constant of 0.05 N m^{-1}) were used. Data were processed using Pico Image Basic software, V 5.1.1.5944 (Keysight Technologies).

5.2.5. Bacterial culture conditions and morphological study

Non-pathogenic *P. fluorescens* cultures (DMS 50090) were prepared by inoculating 25 g L^{-1} sterile LB medium at 30 ± 1°C up to a concentration of 10^9 CFU mL^{-1}, which corresponds to an optical density (OD_{600}) equal to 1.6. The bacteria suspension was then harvested and resuspended in dilute LB medium (0.5 g L^{-1}) and seeded on the

Ag-CF_X samples by immersing them into the bacterial solution and incubating at 30 ± 1 ºC, using a shaking incubator (KS 4000ic control, Keison Products, United Kingdom) for 40 h. The inoculated samples were then rinsed twice with LB medium and MilliQ water and air-dried for the AFM experiments. AFM images were recorded in air, in contact mode AFM with a scan rate of 0.62 ln s^{-1} and using silicon nitride probes (MLCT, Bruker AFM probes, CA, USA; nominal spring constant of 0.06 N m^{-1}). In order to investigate the effect of the AgNPs in the Ag-CF_X samples, the bacteria culture was incubated onto two different Ag-CF_X samples: an Ag-CF_X film prior to its exposure for 30 h to MilliQ water (swollen film) and a pristine Ag-CF_X sample. Statistical data evaluation was performed using ImageJ 1.53e software and IBM SPSS Statistics V 27.0 (Armonk, NY: IBM Corp).

5.3. Electro-deposition of antimicrobial silver nanoparticles on polydopamine films by scanning electrochemical cell microscopy: Chapter 4.3

5.3.1. Materials and chemicals

All solutions were freshly prepared in ultrapure water from a Millipore Milli-Q system (resistivity: 18.0 MΩ cm at 25°C). Dopamine hydrochloride, silver nitrate ($AgNO_3$), and potassium nitrate (KNO_3) were purchased from Sigma-Aldrich (Germany) and Luria-Bertani (LB) culture medium from VWR International GmbH (Germany). Ferrocene-methanol, sodium hydrogen phosphate (Na_2HPO_4), sodium dihydrogen phosphate (NaH_2PO_4), and sodium chloride (NaCl) were purchased from Merck (Germany). 2 cm x 2 cm gold substrates were prepared by sputter coating on silicon wafers and cleaned in acetone, isopropanol, and deionized water, prior to use.

5.3.2. Electrochemical deposition of polydopamine

PDA was deposited on a 2 cm x 2 cm gold substrate *via* electrochemical pulsed-deposition as described elsewhere [153,154,167]. Briefly, the electrochemical deposition was performed using a CHI842B bipotentiostat (CHI Instruments, USA) in a three-electrode cell with the gold-coated silicon substrate serving as the working electrode, a platinum wire as counter electrode and an Ag/AgCl/KCl, (sat.) reference electrode. All the potentials used in this section are *versus* this reference electrode. The pulsed-deposition was performed by applying at the gold working electrode either 25 (PDA_{25}) or 50 (PDA_{50}) cycles with a potential pulse sequence of + 0.5 V / 2 s; 0.0 V / 2 s; – 0.3 V / 2 s; 0.0 V / 3 s. A N_2-purged solution of 5.3 mmol L^{-1} dopamine hypochlorite in 10 mmol L^{-1} PBS (pH 7.4) was used for the electro-deposition. To ensure the complete oxidation of PDA and avoid

spontaneous chemical reduction of silver(I), the PDA film was electro-oxidized in a 10 mmol L^{-1} PBS solution after the deposition, by applying a potential of + 0.5 V for 300 s.

5.3.3. Electro-deposition of AgNPs micro-spots

The electro-deposition of AgNPs on PDA was performed *via* SECCM. All SECCM experiments were performed using a home-built setup, already described elsewhere [59,60,77,78]. The SECCM apparatus is controlled by LabVIEW 2016 software (National Instruments, Austin, USA) assisted *via* a FPGA card (PCIe 7851, National Instruments, Austin, USA). The programmed LabVIEW software is part of the publicly available Warwick Electrochemical Scanning Probe Microscopy (WEC-SPM) software. A lock-in amplifier (SR830, Stanford Research System, United Kingdom) was used to record the currents. Nanopipettes were prepared by pulling quartz capillaries (1.00 mm OD, 0.5 mm ID, Sutter Instruments, Novato, USA) using a laser pipette puller (P-2000, Sutter Instruments, USA) to obtain two pipettes with an orifice of ~ 5 µm. The micropipettes were back-filled with 0.05 mmol L^{-1} to 5.0 mmol L^{-1} $AgNO_3$ in 50 mmol L^{-1} KNO_3 solutions and a AgCl-coated Ag wire was inserted in the back opening of the pipette, serving as a quasi-reference counter electrode (QRCE). The micropipette was mounted on a z-piezo positioner (P-753.3CD, Physics Instruments, Karlsruhe, Germany), perpendicular to the PDA modified sample, serving as a working electrode, which was mounted on an x-y piezo positioner (P-625.2CD, Physics Instruments, Karlsruhe, Germany). A micro-positioner, assisted by a digital camera (PL-B776U, PixeLink, Ottawa, Canada) and a cold light source (MI-150, Edmund Optics, Mainz, Germany), was used for the manual positioning of the pipette at a distance of ca. 50 µm above the PDA sample. An automated software-controlled approach was performed by applying a potential of + 0.2 V vs Ag/AgCl between the QRCE and the sample and moving the pipette with a rate of 1 µm s^{-1} until the droplet contact was formed, indicated by the steep increase in ion current. Upon contact, the micropipette was kept for 0.01 s at the PDA surface (waiting time) before starting the potentiostatic experiments to electrodeposit AgNPs. AgNPs were formed using a double-potentiostatic method, *i.e.*, by applying first a large overpotential (E_n = – 0.4 V vs Ag/AgCl) during 0.5 s (t_n) and subsequently a low overpotential (E_g = – 0.2 vs Ag/AgCl) during a longer period of time (t_g = 1.5 s; 2.5 s; 3.5 s and 4.0 s). Experiments without the application of a nucleation potential (t_n = 0 s) were also performed to investigate the influence of the nucleation step on the size and distribution of the AgNPs. After each deposition step, the pipette was retracted and moved automatically to the next deposition site *via* hopping mode SECCM (see **Section 2.3.1**) and a hopping distance of 50 µm, *i.e.*, with a distance

between each spot equal to 50 µm. Data analysis was processed by using Matlab R2021a (Mathworks, USA) and OriginPro® 2021 software, v 9.8.0.200 (Origin Lab Corporation).

5.3.4. Scanning electron microscopy (SEM)

SEM images were acquired using either a Helios Nanolab 600 FIB/SEM (ThermoFisher, the Netherlands) or a Zeiss SUPRA 55 FE-SEM instrument (Zeiss, Germany), at an acceleration voltage of 5.00 kV and a beam current of 86 pA. Data evaluation was performed using MoutainSPIP® v. 9 (Digital Surf, France) and ImageJ v 1.53q (National Institutes of Health, USA).

5.3.5. Bacterial culture conditions

Cultures of *E. coli* DH5-α were inoculated in 25 g L^{-1} sterile LB medium at 37 ± 1 °C overnight. The bacterial suspension was harvested and resuspended in 0.5 g L^{-1} LB medium and incubated at 37 ± 7 °C until reaching an optical density, OD_{600} = 0.9 (concentration of 7 x 10^8 CFU mL^{-1}). The OD_{600} was monitored using a UV-VIS spectrometer (Thermo Scientific NanoDrop One, Massachusetts, USA). The bacterial culture was then seeded onto the PDA-AgNPs substrates by immersing them into the bacterial solution and incubating at 37 ± 1 ºC for 20 h.

5.3.6. AFM and AFM force spectroscopy experiments

AFM imaging and force spectroscopy experiments were conducted using a 5500 AFM/SPM system from Keysight (Keysight Technologies, AZ, USA) equipped with a close-loop scanner. AFM images were acquired in air in contact mode using silicon nitride probes (MLCT, Bruker AFM probes, CA, USA; nominal spring constant of 0.1 N m^{-1}) and a scan rate of 0.52 ln s^{-1}. Prior to AFM imaging, the inoculated PDA-AgNPs samples were rinsed twice with LB medium, MilliQ water, and afterward air-dried. Force-distance curves were recorded in solution using silicon nitride probes (MLCT, Bruker AFM probes, CA, USA; tip radius of 20 nm and nominal spring constant of 0.1 N m^{-1}) with a leading force of 200 nN. A sweep rate of 1.0 µm s^{-1} was applied to minimize hydrodynamic effects. The force constants of the cantilevers were determined using the thermal noise method [321]. The inoculated samples studied by AFM force spectroscopy were also rinsed with LB medium, and MilliQ water and then immersed in 10 mmol L^{-1} PBS solution (pH = 7.4). Statistical analyses are based on the Student t-test assuming unequal variance. Data evaluation was performed using MoutainSPIP® v. 9 (Digital Surf, France) and OriginPro® 2021 software, v 9.8.0.200 (Origin Lab Corporation).

REFERENCES

[1] T.R. Garrett, M. Bhakoo, Z. Zhang, Bacterial adhesion and biofilms on surfaces, Prog Nat Sci. 18 (2008) 1049–1056. https://doi.org/10.1016/j.pnsc.2008.04.001.

[2] J. Costerton, Introduction to biofilm, Int J Antimicrob Agents. 11 (1999) 217–221. https://doi.org/10.1016/S0924-8579(99)00018-7.

[3] O. Ciofu, C. Moser, P.Ø. Jensen, N. Høiby, Tolerance and resistance of microbial biofilms, Nat Rev Microbiol. 20 (2022) 621–635. https://doi.org/10.1038/s41579-022-00682-4.

[4] J.W. Costerton, K.J. Cheng, G.G. Geesey, T.I. Ladd, J.C. Nickel, M. Dasgupta, T.J. Marrie, Bacterial Biofilms in Nature and Disease, Annu Rev Microbiol. 41 (1987) 435–464. https://doi.org/10.1146/annurev.mi.41.100187.002251.

[5] X. Xu, W. Liu, S. Tian, W. Wang, Q. Qi, P. Jiang, X. Gao, F. Li, H. Li, H. Yu, Petroleum Hydrocarbon-Degrading Bacteria for the Remediation of Oil Pollution Under Aerobic Conditions: A Perspective Analysis, Front Microbiol. 9 (2018). https://doi.org/10.3389/fmicb.2018.02885.

[6] C.-H. Kang, Y.-J. Kwon, J.-S. So, Bioremediation of heavy metals by using bacterial mixtures, Ecol Eng. 89 (2016) 64–69. https://doi.org/10.1016/j.ecoleng.2016.01.023.

[7] T.B. Rasmussen, M. Givskov, Quorum-sensing inhibitors as anti-pathogenic drugs, International J Med Microbiol. 296 (2006) 149–161. https://doi.org/10.1016/j.ijmm.2006.02.005.

[8] M. Cámara, W. Green, C.E. MacPhee, P.D. Rakowska, R. Raval, M.C. Richardson, J. Slater-Jefferies, K. Steventon, J.S. Webb, Economic significance of biofilms: a multidisciplinary and cross-sectoral challenge, NPJ Biofilms Microbiomes. 8 (2022) 42. https://doi.org/10.1038/s41522-022-00306-y.

[9] H.-C. Flemming, J. Wingender, U. Szewzyk, P. Steinberg, S.A. Rice, S. Kjelleberg, Biofilms: an emergent form of bacterial life, Nat Rev Microbiol. 14 (2016) 563–575. https://doi.org/10.1038/nrmicro.2016.94.

[10] J.W. Costerton, P.S. Stewart, E.P. Greenberg, Bacterial Biofilms: A Common Cause of Persistent Infections, Science (1979). 284 (1999) 1318–1322. https://doi.org/10.1126/science.284.5418.1318.

[11] M. Krsmanovic, D. Biswas, H. Ali, A. Kumar, R. Ghosh, A.K. Dickerson, Hydrodynamics and surface properties influence biofilm proliferation, Adv Colloid Interface Sci. 288 (2021) 102336. https://doi.org/10.1016/j.cis.2020.102336.

[12] T. Muthukrishnan, M. al Khaburi, R.M.M. Abed, Fouling Microbial Communities on Plastics Compared with Wood and Steel: Are They Substrate- or Location-Specific?, Microb Ecol. 78 (2019) 361–374. https://doi.org/10.1007/s00248-018-1303-0.

[13] J.A. Roberts, Inhibition and enhancement of microbial surface colonization: the role of silicate composition, Chem Geol. 212 (2004) 313–327. https://doi.org/10.1016/j.chemgeo.2004.08.021.

[14] S. Zheng, M. Bawazir, A. Dhall, H.-E. Kim, L. He, J. Heo, G. Hwang, Implication of Surface Properties, Bacterial Motility, and Hydrodynamic Conditions on Bacterial Surface Sensing and Their Initial Adhesion, Front Bioeng Biotechnol. 9 (2021). https://doi.org/10.3389/fbioe.2021.643722.

[15] O. Rzhepishevska, S. Hakobyan, R. Ruhal, J. Gautrot, D. Barbero, M. Ramstedt, The surface charge of anti-bacterial coatings alters motility and biofilm architecture, Biomater Sci. 1 (2013) 589. https://doi.org/10.1039/c3bm00197k.

[16] A.D. Verderosa, M. Totsika, K.E. Fairfull-Smith, Bacterial Biofilm Eradication Agents: A Current Review, Front Chem. 7 (2019). https://doi.org/10.3389/fchem.2019.00824.

[17] L. Hochvaldová, R. Večeřová, M. Kolář, R. Prucek, L. Kvítek, L. Lapčík, A. Panáček, Antibacterial nanomaterials: Upcoming hope to overcome antibiotic

resistance crisis, Nanotechnol Rev. 11 (2022) 1115–1142. https://doi.org/10.1515/ntrev-2022-0059.

[18] Y.Y. Loo, Y. Rukayadi, M.-A.-R. Nor-Khaizura, C.H. Kuan, B.W. Chieng, M. Nishibuchi, S. Radu, In Vitro Antimicrobial Activity of Green Synthesized Silver Nanoparticles Against Selected Gram-negative Foodborne Pathogens, Front Microbiol. 9 (2018). https://doi.org/10.3389/fmicb.2018.01555.

[19] E.D. Cavassin, L.F.P. de Figueiredo, J.P. Otoch, M.M. Seckler, R.A. de Oliveira, F.F. Franco, V.S. Marangoni, V. Zucolotto, A.S.S. Levin, S.F. Costa, Comparison of methods to detect the in vitro activity of silver nanoparticles (AgNP) against multidrug resistant bacteria, J Nanobiotechnology. 13 (2015) 64. https://doi.org/10.1186/s12951-015-0120-6.

[20] H. Palza, Antimicrobial Polymers with Metal Nanoparticles, Int J Mol Sci. 16 (2015) 2099–2116. https://doi.org/10.3390/ijms16012099.

[21] R. Yañez-Macías, A. Muñoz-Bonilla, M.A. de Jesús-Tellez, H. Maldonado-Textle, C. Guerrero-Sánchez, U.S. Schubert, R. Guerrero-Santos, Combinations of Antimicrobial Polymers with Nanomaterials and Bioactives to Improve Biocidal Therapies, Polymers (Basel). 11 (2019) 1789. https://doi.org/10.3390/polym11111789.

[22] I.I. Niyonshuti, V.R. Krishnamurthi, D. Okyere, L. Song, M. Benamara, X. Tong, Y. Wang, J. Chen, Polydopamine Surface Coating Synergizes the Antimicrobial Activity of Silver Nanoparticles, ACS Appl Mater Interfaces. 12 (2020) 40067–40077. https://doi.org/10.1021/acsami.0c10517.

[23] A. Jain, L.S. Duvvuri, S. Farah, N. Beyth, A.J. Domb, W. Khan, Antimicrobial Polymers, Adv Healthc Mater. 3 (2014) 1969–1985. https://doi.org/10.1002/adhm.201400418.

[24] J. Donné, S. Dewilde, The Challenging World of Biofilm Physiology, in: Adv Microb Physiol, 2015: pp. 235–292. https://doi.org/10.1016/bs.ampbs.2015.09.003.

[25] M. Pousti, M.P. Zarabadi, M. Abbaszadeh Amirdehi, F. Paquet-Mercier, J. Greener, Microfluidic bioanalytical flow cells for biofilm studies: a review, Analyst. 144 (2019) 68–86. https://doi.org/10.1039/C8AN01526K.

[26] G. Binnig, C.F. Quate, Ch. Gerber, Atomic Force Microscope, Phys Rev Lett. 56 (1986) 930–933. https://doi.org/10.1103/PhysRevLett.56.930.

[27] A. Viljoen, M. Mathelié-Guinlet, A. Ray, N. Strohmeyer, Y.J. Oh, P. Hinterdorfer, D.J. Müller, D. Alsteens, Y.F. Dufrêne, Force spectroscopy of single cells using atomic force microscopy, Nat Rev Methods Primers. 1 (2021) 63. https://doi.org/10.1038/s43586-021-00062-x.

[28] A. Beaussart, S. El-Kirat-Chatel, Microbial adhesion and ultrastructure from the single-molecule to the single-cell levels by Atomic Force Microscopy, Cell Surf. 5 (2019) 100031. https://doi.org/10.1016/j.tcsw.2019.100031.

[29] A.J. Bard, M. v. Mirkin, Scanning Electrochemical Microscopy, 3rd ed., CRC Press, New York, 2022. https://www.taylorfrancis.com/books/9781439831137/chapters/10.1201/b11850-16.

[30] X. Liu, M.M. Ramsey, X. Chen, D. Koley, M. Whiteley, A.J. Bard, Real-time mapping of a hydrogen peroxide concentration profile across a polymicrobial bacterial biofilm using scanning electrochemical microscopy, Proc Natl Acad Sci. 108 (2011) 2668–2673. https://doi.org/10.1073/pnas.1018391108.

[31] N.M. Jayathilake, D. Koley, Glucose Microsensor with Covalently Immobilized Glucose Oxidase for Probing Bacterial Glucose Uptake by Scanning Electrochemical Microscopy, Anal Chem. 92 (2020) 3589–3597. https://doi.org/10.1021/acs.analchem.9b04284.

[32] G. Pecchielan, D. Battistel, S. Daniele, Scanning Electrochemical Microscopy and Voltammetric Investigation of Silver Nanoparticles Embedded within a Nafion Membrane, ChemElectroChem. 3 (2016) 2297–2304. https://doi.org/10.1002/celc.201600483.

[33] D. Battistel, F. Baldi, M. Gallo, C. Faleri, S. Daniele, Characterisation of biosynthesised silver nanoparticles by scanning electrochemical microscopy (SECM) and voltammetry, Talanta. 132 (2015) 294–300. https://doi.org/10.1016/j.talanta.2014.09.023.

[34] N. Ebejer, M. Schnippering, A.W. Colburn, M.A. Edwards, P.R. Unwin, Localized High Resolution Electrochemistry and Multifunctional Imaging: Scanning Electrochemical Cell Microscopy, Anal Chem. 82 (2010) 9141–9145. https://doi.org/10.1021/ac102191u.

[35] S.C.S. Lai, R.A. Lazenby, P.M. Kirkman, P.R. Unwin, Nucleation, aggregative growth and detachment of metal nanoparticles during electrodeposition at electrode surfaces, Chem Sci. 6 (2015) 1126–1138. https://doi.org/10.1039/C4SC02792B.

[36] D. Valavanis, P. Ciocci, G.N. Meloni, P. Morris, J.-F. Lemineur, I.J. McPherson, F. Kanoufi, P.R. Unwin, Hybrid scanning electrochemical cell microscopy-interference reflection microscopy (SECCM-IRM): tracking phase formation on surfaces in small volumes, Faraday Discuss. 233 (2022) 122–148. https://doi.org/10.1039/D1FD00063B.

[37] E. Oswald, A. Gaus, J. Kund, M. Küllmer, J. Romer, S. Weizenegger, T. Ullrich, A.K. Mengele, L. Petermann, R. Leiter, P.R. Unwin, U. Kaiser, S. Rau, A. Kahnt, A. Turchanin, M. Delius, C. Kranz, Cobaloxime Complex Salts: Synthesis, Patterning on Carbon Nanomembranes and Heterogeneous Hydrogen Evolution Studies, Eur J Chem. 27 (2021) 16896–16903. https://doi.org/10.1002/chem.202102778.

[38] J. Hengsteler, B. Mandal, C. van Nisselroy, G.P.S. Lau, T. Schlotter, T. Zambelli, D. Momotenko, Bringing Electrochemical Three-Dimensional Printing to the Nanoscale, Nano Lett. 21 (2021) 9093–9101. https://doi.org/10.1021/acs.nanolett.1c02847.

[39] S. Pandit, S. Sarode, K. Chandrasekhar, Fundamentals of Bacterial Biofilm: Present State of Art, in: Quorum Sensing and Its Biotechnological Applications, Springer Singapore, Singapore, 2018: pp. 43–60. https://doi.org/10.1007/978-981-13-0848-2_3.

[40] B. Virdis, F. Harnisch, D.J. Batstone, K. Rabaey, B.C. Donose, Non-invasive characterization of electrochemically active microbial biofilms using confocal Raman microscopy, Energy Environ Sci. 5 (2012) 7017. https://doi.org/10.1039/c2ee03374g.

[41] P. Stenclova, S. Freisinger, H. Barth, A. Kromka, B. Mizaikoff, Cyclic Changes in the Amide Bands Within Escherichia coli Biofilms Monitored Using Real-Time Infrared Attenuated Total Reflection Spectroscopy (IR-ATR), Appl Spectrosc. 73 (2019) 424–432. https://doi.org/10.1177/0003702819829081.

[42] F. Humbert, F. Quilès, A. Delille, In situ assessment of drinking water biostability using nascent reference biofilm ATR-FTIR fingerprint, in: Current Research Topics in Applied Microbiology and Microbial Biotechnology, World Scientific, 2009: pp. 268–272. https://doi.org/10.1142/9789812837554_0056.

[43] T.R. Neu, J.R. Lawrence, Advanced Techniques for In Situ Analysis of the Biofilm Matrix (Structure, Composition, Dynamics), in: Means of Laser Scanning Microscopy, 2014: pp. 43–64. https://doi.org/10.1007/978-1-4939-0467-9_4.

[44] P. Stenclova, S. Freisinger, H. Barth, A. Kromka, B. Mizaikoff, Cyclic Changes in the Amide Bands Within Escherichia coli Biofilms Monitored Using Real-Time Infrared Attenuated Total Reflection Spectroscopy (IR-ATR), Appl Spectrosc. 73 (2019) 424–432. https://doi.org/10.1177/0003702819829081.

[45] G. Pavanello, M. Faimali, M. Pittore, A. Mollica, A. Mollica, A. Mollica, Exploiting a new electrochemical sensor for biofilm monitoring and water treatment optimization, Water Res. 45 (2011) 1651–1658. https://doi.org/10.1016/j.watres.2010.12.003.

[46] Y. Yi, T. Zhao, B. Xie, Y. Zang, H. Liu, Dual detection of biochemical oxygen demand and nitrate in water based on bidirectional Shewanella loihica electron transfer, Bioresour Technol. 309 (2020) 123402. https://doi.org/10.1016/j.biortech.2020.123402.

[47] D. Harris, J.G. Ummadi, A.R. Thurber, Y. Allau, C. Verba, F. Colwell, M.E. Torres, D. Koley, Real-time monitoring of calcification process by Sporosarcina pasteurii biofilm, Analyst. 141 (2016) 2887–2895. https://doi.org/10.1039/C6AN00007J.

[48] R. Funari, A.Q. Shen, Detection and Characterization of Bacterial Biofilms and Biofilm-Based Sensors, ACS Sens. 7 (2022) 347–357. https://doi.org/10.1021/acssensors.1c02722.

[49] G.; Binnig, H. Rohrer, Scanning tunneling microscopy, Helv Chim Acta. 55 (1982) 726–735. https://doi.org/10.5169/seals-115309.

[50] D. Alsteens, D.J. Müller, Y.F. Dufrêne, Multiparametric Atomic Force Microscopy Imaging of Biomolecular and Cellular Systems, Acc Chem Res. 50 (2017) 924–931. https://doi.org/10.1021/acs.accounts.6b00638.

[51] S. Aguayo, N. Donos, D. Spratt, L. Bozec, Single-bacterium nanomechanics in biomedicine: unravelling the dynamics of bacterial cells, Nanotechnology. 26 (2015) 062001. https://doi.org/10.1088/0957-4484/26/6/062001.

[52] I. Gammoudi, M. Mathelie-guinlet, F. Morote, L. Beven, D. Moynet, C. Grauby-heywang, T. Cohen-bouhacina, Morphological and nanostructural surface changes in Escherichia coli over time, monitored by atomic force microscopy, Colloids Surf B Biointerfaces. 141 (2016) 355–364. https://doi.org/10.1016/j.colsurfb.2016.02.006.

[53] S. Darvishi, H. Pick, E. Oveisi, H.H. Girault, A. Lesch, Soft-probe-scanning electrochemical microscopy reveals electrochemical surface reactivity of E. coli biofilms, Sens Actuators B Chem. 334 (2021) 129669. https://doi.org/10.1016/j.snb.2021.129669.

[54] A.J. Bard, F.R.F. Fan, Juhyoun. Kwak, Ovadia. Lev, Scanning electrochemical microscopy. Introduction and principles, Anal Chem. 61 (1989) 132–138. https://doi.org/10.1021/ac00177a011.

[55] R.C. Engstrom, C.M. Pharr, Scanning electrochemical microscopy, Anal Chem. 61 (1989) 1099A-1104A. https://doi.org/10.1021/ac00194a002.

[56] D. Polcari, P. Dauphin-Ducharme, J. Mauzeroll, Scanning Electrochemical Microscopy: A Comprehensive Review of Experimental Parameters from 1989 to 2015, Chem Rev. 116 (2016) 13234–13278. https://doi.org/10.1021/acs.chemrev.6b00067.

[57] A.J. Bard, M. v. Mirkin, Scanning Electrochemical Microscopy, CRC Press, Boca Raton, 2022. https://doi.org/10.1201/9781003004592.

[58] S. Amemiya, A.J. Bard, F.-R.F. Fan, M. v. Mirkin, P.R. Unwin, Scanning Electrochemical Microscopy, Annu Rev Anal Chem. 1 (2008) 95–131. https://doi.org/10.1146/annurev.anchem.1.031207.112938.

[59] C.L. Bentley, M. Kang, P.R. Unwin, Scanning electrochemical cell microscopy: New perspectives on electrode processes in action, Curr Opin Electrochem. 6 (2017) 23–30. https://doi.org/10.1016/j.coelec.2017.06.011.

[60] N. Ebejer, A.G. Güell, S.C.S. Lai, K. McKelvey, M.E. Snowden, P.R. Unwin, Scanning Electrochemical Cell Microscopy: A Versatile Technique for Nanoscale Electrochemistry and Functional Imaging, Annu Rev Anal Chem. 6 (2013) 329–351. https://doi.org/10.1146/annurev-anchem-062012-092650.

[61] J.L. Alonso, W.H. Goldmann, Feeling the forces: atomic force microscopy in cell biology, Life Sci. 72 (2003) 2553–2560. https://doi.org/10.1016/S0024-3205(03)00165-6.

[62] G. Binnig, C.F. Quate, Ch. Gerber, Atomic Force Microscope, Phys Rev Lett. 56 (1986) 930–933. https://doi.org/10.1103/PhysRevLett.56.930.

[63] H.-J. Butt, B. Cappella, M. Kappl, Force measurements with the atomic force microscope: Technique, interpretation and applications, Surf Sci Rep. 59 (2005) 1–152. https://doi.org/10.1016/j.surfrep.2005.08.003.

[64] B.B. Katemann, W. Schuhmann, Fabrication and Characterization of Needle-Type, Electroanalysis. 14 (2002) 22–28. https://doi.org/10.1002/1521-4109(200201)14:1<22::AID-ELAN22>3.0.CO;2-F.

[65] P. Sun, M. v. Mirkin, Kinetics of Electron-Transfer Reactions at Nanoelectrodes, Anal Chem. 78 (2006) 6526–6534. https://doi.org/10.1021/ac060924q.

[66] A.J. Bard, L.R. Faulkner, Electrochemical Methods: Fundamentals and Applications, 2nd ed., New York, 2000. https://doi.org/10.1023/A:1021637209564.

[67] D. Shoup, A. Szabo, Chronoamperometry at an ensemble of microdisk electrodes, J Electroanal Chem Interfacial Electrochem. 160 (1984) 19–26. https://doi.org/10.1016/S0022-0728(84)80111-4.

[68] J.L. Amphlett, G. Denuault, Scanning Electrochemical Microscopy (SECM): An Investigation of the Effects of Tip Geometry on Amperometric Tip Response, J Phys Chem B. 102 (1998) 9946–9951. https://doi.org/10.1021/jp982829u.

[69] R. Cornut, C. Lefrou, New analytical approximation of feedback approach curves with a microdisk SECM tip and irreversible kinetic reaction at the substrate, J

Electroanal Chem. 621 (2008) 178–184. https://doi.org/10.1016/j.jelechem.2007.09.021.

[70] G. Pecchielan, D. Battistel, S. Daniele, Scanning Electrochemical Microscopy and Voltammetric Investigation of Silver Nanoparticles Embedded within a Nafion Membrane, ChemElectroChem. 3 (2016) 2297–2304. https://doi.org/10.1002/celc.201600483.

[71] D.A. Skoog, F.J. Holler, S.R. Crouch, D.M. West, C. Learning, Voltammetry, in: Fundamentals of Analytical Chemistry, 7th ed., Andover Hants: Cengage Learning, 2014.

[72] K.B. Holt, A.J. Bard, Interaction of Silver(I) Ions with the Respiratory Chain of Escherichia coli : An Electrochemical and Scanning Electrochemical Microscopy Study of the Antimicrobial Mechanism of Micromolar Ag+, Biochemistry. 44 (2005) 13214–13223. https://doi.org/10.1021/bi0508542.

[73] D. Battistel, F. Baldi, M. Gallo, C. Faleri, S. Daniele, Characterisation of biosynthesised silver nanoparticles by scanning electrochemical microscopy (SECM) and voltammetry, Talanta. 132 (2015) 294–300. https://doi.org/10.1016/j.talanta.2014.09.023.

[74] Controlled-Potential Techniques, in: Analytical Electrochemistry, John Wiley & Sons, Inc., Hoboken, NJ, USA, 2006: pp. 67–114. https://doi.org/10.1002/0471790303.ch3.

[75] D.P. Whelan, J.J. O'Dea, J. Osteryoung, K. Aoki, Square wave voltammetry at small disk electrodes, J Electroanal Chem Interfacial Electrochem. 202 (1986) 23–36. https://doi.org/10.1016/0022-0728(86)90105-1.

[76] L.C. Yule, C.L. Bentley, G. West, B.A. Shollock, P.R. Unwin, Scanning electrochemical cell microscopy: A versatile method for highly localised corrosion related measurements on metal surfaces, Electrochim Acta. 298 (2019) 80–88. https://doi.org/10.1016/j.electacta.2018.12.054.

[77] L.C. Yule, V. Shkirskiy, J. Aarons, G. West, C.L. Bentley, B.A. Shollock, P.R. Unwin, Nanoscale Active Sites for the Hydrogen Evolution Reaction on Low Carbon Steel, J Phys Chem C. 123 (2019) 24146–24155. https://doi.org/10.1021/acs.jpcc.9b07216.

[78] C.L. Bentley, P.R. Unwin, Nanoscale electrochemical movies and synchronous topographical mapping of electrocatalytic materials, Faraday Discuss. 210 (2018) 365–379. https://doi.org/10.1039/C8FD00028J.

[79] K. McKelvey, S.L. Kinnear, D. Perry, D. Momotenko, P.R. Unwin, Surface Charge Mapping with a Nanopipette, J Am Chem Soc. 136 (2014) 13735–13744. https://doi.org/10.1021/ja506139u.

[80] E. Oswald, A. Gaus, J. Kund, M. Küllmer, J. Romer, S. Weizenegger, T. Ullrich, A.K. Mengele, L. Petermann, R. Leiter, P.R. Unwin, U. Kaiser, S. Rau, A. Kahnt, A. Turchanin, M. Delius, C. Kranz, Cobaloxime Complex Salts: Synthesis, Patterning on Carbon Nanomembranes and Heterogeneous Hydrogen Evolution Studies, Eur J Chem. 28 (2022). https://doi.org/10.1002/chem.202200889.

[81] S.C.S. Lai, R.A. Lazenby, P.M. Kirkman, P.R. Unwin, Nucleation, aggregative growth and detachment of metal nanoparticles during electrodeposition at electrode surfaces, Chem Sci. 6 (2015) 1126–1138. https://doi.org/10.1039/C4SC02792B.

[82] C.B. Volle, M.A. Ferguson, K.E. Aidala, E.M. Spain, M.E. Núñez, Spring constants and adhesive properties of native bacterial biofilm cells measured by atomic force microscopy, Colloids Surf B Biointerfaces. 67 (2008) 32–40. https://doi.org/10.1016/j.colsurfb.2008.07.021.

[83] R.G. Bailey, R.D. Turner, N. Mullin, N. Clarke, S.J. Foster, J.K. Hobbs, The Interplay between Cell Wall Mechanical Properties and the Cell Cycle in Staphylococcus aureus, Biophys J. 107 (2014) 2538–2545. https://doi.org/10.1016/j.bpj.2014.10.036.

[84] F. Ahimou, F.A. Denis, A. Touhami, Y.F. Dufrêne, Probing Microbial Cell Surface Charges by Atomic Force Microscopy, Langmuir. 18 (2002) 9937–9941. https://doi.org/10.1021/la026273k.

[85] H.-J. Butt, Measuring electrostatic, van der Waals, and hydration forces in electrolyte solutions with an atomic force microscope, Biophys J. 60 (1991) 1438–1444. https://doi.org/10.1016/S0006-3495(91)82180-4.

[86] R. Garcia, Nanomechanical mapping of soft materials with the atomic force microscope: methods, theory and applications, Chem Soc Rev. 49 (2020) 5850–5884. https://doi.org/10.1039/D0CS00318B.

[87] A. Alessandrini, P. Facci, AFM: a versatile tool in biophysics, Meas Sci Technol. 16 (2005) R65–R92. https://doi.org/10.1088/0957-0233/16/6/R01.

[88] J. Zhong, J. Yan, Seeing is believing: atomic force microscopy imaging for nanomaterial research, RSC Adv. 6 (2016) 1103–1121. https://doi.org/10.1039/C5RA22186B.

[89] D. Alsteens, H.E. Gaub, R. Newton, M. Pfreundschuh, C. Gerber, D.J. Müller, Atomic force microscopy-based characterization and design of biointerfaces, Nat Rev Mater. 2 (2017) 17008. https://doi.org/10.1038/natrevmats.2017.8.

[90] M. Krieg, G. Fläschner, D. Alsteens, B.M. Gaub, W.H. Roos, G.J.L. Wuite, H.E. Gaub, C. Gerber, Y.F. Dufrêne, D.J. Müller, Atomic force microscopy-based mechanobiology, Nat Rev Phys. 1 (2019) 41–57. https://doi.org/10.1038/s42254-018-0001-7.

[91] N. Jalili, K. Laxminarayana, A review of atomic force microscopy imaging systems: application to molecular metrology and biological sciences, Mechatronics. 14 (2004) 907–945. https://doi.org/10.1016/j.mechatronics.2004.04.005.

[92] T.R. Albrecht, P. Grütter, D. Horne, D. Rugar, Frequency modulation detection using high- Q cantilevers for enhanced force microscope sensitivity, J Appl Phys. 69 (1991) 668–673. https://doi.org/10.1063/1.347347.

[93] J. Lübbe, L. Tröger, S. Torbrügge, R. Bechstein, C. Richter, A. Kühnle, M. Reichling, Achieving high effective Q -factors in ultra-high vacuum dynamic force microscopy, Meas Sci Technol. 21 (2010) 125501. https://doi.org/10.1088/0957-0233/21/12/125501.

[94] T. Fukuma, K. Kobayashi, K. Matsushige, H. Yamada, True atomic resolution in liquid by frequency-modulation atomic force microscopy, Appl Phys Lett. 87 (2005) 034101. https://doi.org/10.1063/1.1999856.

[95] M.J. Higgins, J.E. Sader, S.P. Jarvis, Frequency Modulation Atomic Force Microscopy Reveals Individual Intermediates Associated with each Unfolded I27 Titin Domain, Biophys J. 90 (2006) 640–647. https://doi.org/10.1529/biophysj.105.066571.

[96] T. Fukuma, M.J. Higgins, S.P. Jarvis, Direct Imaging of Individual Intrinsic Hydration Layers on Lipid Bilayers at Ångstrom Resolution, Biophys J. 92 (2007) 3603–3609. https://doi.org/10.1529/biophysj.106.100651.

[97] T. Fukuma, S.P. Jarvis, Biological Applications of FM-AFM in Liquid Environment, in: 2009: pp. 329–345. https://doi.org/10.1007/978-3-642-01495-6_16.

[98] Q. Zhong, D. Inniss, K. Kjoller, V.B. Elings, Fractured polymer/silica fiber surface studied by tapping mode atomic force microscopy, Surf Sci. 290 (1993) L688–L692. https://doi.org/10.1016/0039-6028(93)90582-5.

[99] P.K. Hansma, J.P. Cleveland, M. Radmacher, D.A. Walters, P.E. Hillner, M. Bezanilla, M. Fritz, D. Vie, H.G. Hansma, C.B. Prater, J. Massie, L. Fukunaga, J. Gurley, V. Elings, Tapping mode atomic force microscopy in liquids, Appl Phys Lett. 64 (1994) 1738–1740. https://doi.org/10.1063/1.111795.

[100] P.K. Hansma, J.P. Cleveland, M. Radmacher, D.A. Walters, P.E. Hillner, M. Bezanilla, M. Fritz, D. Vie, H.G. Hansma, C.B. Prater, J. Massie, L. Fukunaga, J. Gurley, V. Elings, Tapping mode atomic force microscopy in liquids, Appl Phys Lett. 64 (1994) 1738–1740. https://doi.org/10.1063/1.111795.

[101] Q. Zhong, D. Inniss, K. Kjoller, V.B. Elings, Fractured polymer/silica fiber surface studied by tapping mode atomic force microscopy, Surf Sci Lett. 290 (1993) L688–L692. https://doi.org/10.1016/0167-2584(93)90906-Y.

[102] H. Hölscher, U.D. Schwarz, Theory of amplitude modulation atomic force microscopy with and without Q-Control, Int J Non Linear Mech. 42 (2007) 608–625. https://doi.org/10.1016/j.ijnonlinmec.2007.01.018.

[103] R. García, Dynamic atomic force microscopy methods, Surf Sci Rep. 47 (2002) 197–301. https://doi.org/10.1016/S0167-5729(02)00077-8.

[104] G. Reiter, G. Castelein, J.-U. Sommer, A. Röttele, T. Thurn-Albrecht, Direct Visualization of Random Crystallization and Melting in Arrays of Nanometer-Size Polymer Crystals, Phys Rev Lett. 87 (2001) 226101. https://doi.org/10.1103/PhysRevLett.87.226101.

[105] A. Janshoff, M. Neitzert, Y. Oberdörfer, H. Fuchs, Force Spectroscopy of Molecular Systems—Single Molecule Spectroscopy of Polymers and Biomolecules, Angewandte Chem. Int Ed. 39 (2000) 3212–3237. https://doi.org/10.1002/1521-3773(20000915)39:18<3212::AID-ANIE3212>3.0.CO;2-X.

[106] J. Drelich, K.L. Mittal, Atomic Force Microscopy in Adhesion Studies, 1st ed., CRC Press, London, 2005. https://doi.org/10.1201/b12164.

[107] B.V. Derjaguin, V.M. Muller, Yu.P. Toporov, Effect of contact deformations on the adhesion of particles, J Colloid Interface Sci. 53 (1975) 314–326. https://doi.org/10.1016/0021-9797(75)90018-1.

[108] I.N. Sneddon, The relation between load and penetration in the axisymmetric boussinesq problem for a punch of arbitrary profile, Int J Eng Sci. 3 (1965) 47–57. https://doi.org/10.1016/0020-7225(65)90019-4.

[109] H. Hertz, Über die Berührung fester elastischer Körper, Für Die Reine Und Angew. Math. (1881) 156–171.

[110] G. Caniglia, G. Tezcan, G.N. Meloni, P.R. Unwin, C. Kranz, Probing and Visualizing Interfacial Charge at Surfaces in Aqueous Solution, Annu Rev Anal Chem. 15 (2022) 247–267. https://doi.org/10.1146/annurev-anchem-121521-122615.

[111] D.R.H. Jones, M.F. Ashby, Elastic Moduli, in: Engineering Materials 1, Elsevier, 2019: pp. 31–47. https://doi.org/10.1016/B978-0-08-102051-7.00003-8.

[112] A. Vinckier, G. Semenza, Measuring elasticity of biological materials by atomic force microscopy, FEBS Lett. 430 (1998) 12–16. https://doi.org/10.1016/S0014-5793(98)00592-4.

[113] J.N. Israelachvili, Intermolecular and Surface Forces, Third Edit, Elsevier, San Diego, 2011. https://doi.org/10.1016/C2011-0-05119-0.

[114] B. Derjaguin, L. Landau, Theory of the stability of strongly charged lyophobic sols and of the adhesion of strongly charged particles in solutions of electrolytes, Prog Surf Sci. 43 (1993) 30–59. https://doi.org/10.1016/0079-6816(93)90013-L.

[115] C. Argento, R.H. French, Parametric tip model and force–distance relation for Hamaker constant determination from atomic force microscopy, J Appl Phys. 80 (1996) 6081–6090. https://doi.org/10.1063/1.363680.

[116] L. Bergström, Hamaker constants of inorganic materials, Adv Colloid Interface Sci. 70 (1997) 125–169. https://doi.org/10.1016/S0001-8686(97)00003-1.

[117] M. Gouy, Sur la constitution de la charge électrique à la surface d'un électrolyte, J Phys Théor Appl. 9 (1910) 457–468. https://doi.org/10.1051/jphystap:019100090045700.

[118] D.L. Chapman, LI. A contribution to the theory of electrocapillarity, Lond, Edinb Dublin Philos Mag J Sci. 25 (1913) 475–481. https://doi.org/10.1080/14786440408634187.

[119] V.S. Bagotsky, Fundamentals of Electrochemistry, 2nd ed., John Wiley & Sons, Inc., 2005.

[120] P. Debye, E. Hückel, Zur Theorie der Elektrolyte. I. Gefrierpunktserniedrigung und verwandte Erscheinungen, Physikalische Zeitschrift. 24 (1923) 305.

[121] V. Steffen, E.A. Silva, L.R. Evangelista, L. Cardozo-Filho, Debye–Hückel approximation for simplification of ions adsorption equilibrium model based on Poisson–Boltzmann equation, Surf Interfaces. 10 (2018) 144–148. https://doi.org/10.1016/j.surfin.2018.01.005.

[122] H.-J. Butt, Electrostatic interaction in scanning probe microscopy when imaging in electrolyte solutions, Nanotechnology. 3 (1992) 60–68. https://doi.org/10.1088/0957-4484/3/2/003.

[123] V.A. Parsegian, D. Gingell, On the Electrostatic Interaction across a Salt Solution between Two Bodies Bearing Unequal Charges, Biophys J. 12 (1972) 1192–1204. https://doi.org/10.1016/S0006-3495(72)86155-1.

[124] H.-C. Flemming, Biofouling in water systems – cases, causes and countermeasures, Appl Microbiol Biotechnol. 59 (2002) 629–640. https://doi.org/10.1007/s00253-002-1066-9.

[125] M.P. Schultz, J.A. Bendick, E.R. Holm, W.M. Hertel, Economic impact of biofouling on a naval surface ship, Biofouling. 27 (2011) 87–98. https://doi.org/10.1080/08927014.2010.542809.

[126] E.R. Silva, O. Ferreira, P.A. Ramalho, N.F. Azevedo, R. Bayón, A. Igartua, J.C. Bordado, M.J. Calhorda, Eco-friendly non-biocide-release coatings for marine biofouling prevention, Sci Total Environ. 650 (2019) 2499–2511. https://doi.org/10.1016/j.scitotenv.2018.10.010.

[127] G.B. Hwang, K. Page, A. Patir, S.P. Nair, E. Allan, I.P. Parkin, The Anti-Biofouling Properties of Superhydrophobic Surfaces are Short-Lived, ACS Nano. 12 (2018) 6050–6058. https://doi.org/10.1021/acsnano.8b02293.

[128] P. Zhang, L. Lin, D. Zang, X. Guo, M. Liu, Designing Bioinspired Anti-Biofouling Surfaces based on a Superwettability Strategy, Small. 13 (2017) 1503334. https://doi.org/10.1002/smll.201503334.

[129] C.S. Ong, P.S. Goh, W.J. Lau, N. Misdan, A.F. Ismail, Nanomaterials for biofouling and scaling mitigation of thin film composite membrane: A review, Desalination. 393 (2016) 2–15. https://doi.org/10.1016/j.desal.2016.01.007.

[130] I. Jiménez-Pardo, L. van der Ven, R. van Benthem, G. de With, A. Esteves, Hydrophilic Self-Replenishing Coatings with Long-Term Water Stability for Anti-Fouling Applications, Coatings. 8 (2018) 184. https://doi.org/10.3390/coatings8050184.

[131] S. BinAhmed, A. Hasane, Z. Wang, A. Mansurov, S. Romero-Vargas Castrillón, Bacterial Adhesion to Ultrafiltration Membranes: Role of Hydrophilicity, Natural Organic Matter, and Cell-Surface Macromolecules, Environ Sci Technol. 52 (2018) 162–172. https://doi.org/10.1021/acs.est.7b03682.

[132] S.E. Rollauer, M.A. Sooreshjani, N. Noinaj, S.K. Buchanan, Outer membrane protein biogenesis in Gram-negative bacteria, Philos Trans R Soc Lond B: Biol Sci. 370 (2015) 20150023. https://doi.org/10.1098/rstb.2015.0023.

[133] G. Gonella, E.H.G. Backus, Y. Nagata, D.J. Bonthuis, P. Loche, A. Schlaich, R.R. Netz, A. Kühnle, I.T. McCrum, M.T.M. Koper, M. Wolf, B. Winter, G. Meijer, R.K. Campen, M. Bonn, Water at charged interfaces, Nat Rev Chem. 5 (2021) 466–485. https://doi.org/10.1038/s41570-021-00293-2.

[134] G. Caniglia, G. Tezcan, G.N. Meloni, P.R. Unwin, C. Kranz, Probing and Visualizing Interfacial Charge at Surfaces in Aqueous Solution, Annu Rev Anal Chem. 15 (2022) 247–267. https://doi.org/10.1146/annurev-anchem-121521-122615.

[135] D.C. Grahame, The Electrical Double Layer and the Theory of Electrocapillarity., Chem Rev. 41 (1947) 441–501. https://doi.org/10.1021/cr60130a002.

[136] G. Gonella, E.H.G. Backus, Y. Nagata, D.J. Bonthuis, P. Loche, A. Schlaich, R.R. Netz, A. Kühnle, I.T. McCrum, M.T.M. Koper, M. Wolf, B. Winter, G. Meijer, R.K. Campen, M. Bonn, Water at charged interfaces, Nat Rev Chem. 5 (2021) 466–485. https://doi.org/10.1038/s41570-021-00293-2.

[137] K. McKelvey, S.L. Kinnear, D. Perry, D. Momotenko, P.R. Unwin, Surface Charge Mapping with a Nanopipette, J Am Chem Soc. 136 (2014) 13735–13744. https://doi.org/10.1021/ja506139u.

[138] Y. Ma, R. Liu, X. Shen, D. Wang, Quantification of Asymmetric Ion Transport in Glass Nanopipettes near Charged Substrates, ChemElectroChem. 8 (2021) 3917–3922. https://doi.org/10.1002/celc.202101180.

[139] A. Guney, F. Kara, O. Ozgen, E.A. Aksoy, V. Hasirci, N. Hasirci, Surface Modification of Polymeric Biomaterials, in: Biomaterials Surface Science, Wiley, 2013: pp. 89–158. https://doi.org/10.1002/9783527649600.ch5.

[140] F. Siedenbiedel, J.C. Tiller, Antimicrobial Polymers in Solution and on Surfaces: Overview and Functional Principles, Polymers (Basel). 4 (2012) 46–71. https://doi.org/10.3390/polym4010046.

[141] A. Jain, L.S. Duvvuri, S. Farah, N. Beyth, A.J. Domb, W. Khan, Antimicrobial Polymers, Adv Healthc Mater. 3 (2014) 1969–1985. https://doi.org/10.1002/adhm.201400418.

[142] V. Ball, Physicochemical perspective on “polydopamine” and “poly(catecholamine)” films for their applications in biomaterial coatings (Review), Biointerphases. 9 (2014) 030801. https://doi.org/10.1116/1.4875115.

[143] I. Singh, G. Dhawan, S. Gupta, P. Kumar, Recent Advances in a Polydopamine-Mediated Antimicrobial Adhesion System, Front Microbiol. 11 (2021). https://doi.org/10.3389/fmicb.2020.607099.

[144] H. Karkhanechi, R. Takagi, H. Matsuyama, Biofouling resistance of reverse osmosis membrane modified with polydopamine, Desalination. 336 (2014) 87–96. https://doi.org/10.1016/j.desal.2013.12.033.

[145] H.M. Hegab, A. ElMekawy, T.G. Barclay, A. Michelmore, L. Zou, C.P. Saint, M. Ginic-Markovic, Effective in-situ chemical surface modification of forward osmosis membranes with polydopamine-induced graphene oxide for biofouling mitigation, Desalination. 385 (2016) 126–137. https://doi.org/10.1016/j.desal.2016.02.021.

[146] H. Lee, J. Rho, P.B. Messersmith, Facile Conjugation of Biomolecules onto Surfaces via Mussel Adhesive Protein Inspired Coatings, Adv Mater. 21 (2009) 431–434. https://doi.org/10.1002/adma.200801222.

[147] Z. Liu, Y. Hu, Sustainable Antibiofouling Properties of Thin Film Composite Forward Osmosis Membrane with Rechargeable Silver Nanoparticles Loading, ACS Appl Mater Interfaces. 8 (2016) 21666–21673. https://doi.org/10.1021/acsami.6b06727.

[148] L. Tang, K.J.T. Livi, K.L. Chen, Polysulfone Membranes Modified with Bioinspired Polydopamine and Silver Nanoparticles Formed in Situ To Mitigate Biofouling, Environ Sci Technol Lett. 2 (2015) 59–65. https://doi.org/10.1021/acs.estlett.5b00008.

[149] F. Binns, J.A.G. King, S.N. Mishra, A. Percival, N.C. Robson, G.A. Swan, A. Waggott, Studies related to the chemistry of melanins. Part XIII. Studies on the structure of dopamine-melanin, J Chem Soc C: Organic. (1970) 2063. https://doi.org/10.1039/j39700002063.

[150] H. Lee, S.M. Dellatore, W.M. Miller, P.B. Messersmith, Mussel-Inspired Surface Chemistry for Multifunctional Coatings, Science (1979). 318 (2007) 426–430. https://doi.org/10.1126/science.1147241.

[151] Y. Li, M. Liu, C. Xiang, Q. Xie, S. Yao, Electrochemical quartz crystal microbalance study on growth and property of the polymer deposit at gold electrodes during oxidation of dopamine in aqueous solutions, Thin Solid Films. 497 (2006) 270–278. https://doi.org/10.1016/j.tsf.2005.10.048.

[152] F. Bernsmann, J.-C. Voegel, V. Ball, Different synthesis methods allow to tune the permeability and permselectivity of dopamine–melanin films to electrochemical probes, Electrochim Acta. 56 (2011) 3914–3919. https://doi.org/10.1016/j.electacta.2011.02.028.

[153] J. Lin, S. Daboss, D. Blaimer, C. Kranz, Micro-Structured Polydopamine Films via Pulsed Electrochemical Deposition, Nanomaterials. 9 (2019) 242. https://doi.org/10.3390/nano9020242.

[154] J. Kund, S. Daboss, T.M. D'Alvise, S. Harvey, C. v. Synatschke, T. Weil, C. Kranz, Physicochemical and Electrochemical Characterization of Electropolymerized Polydopamine Films: Influence of the Deposition Process, Nanomaterials. 11 (2021) 1964. https://doi.org/10.3390/nano11081964.

[155] J.H. Ryu, P.B. Messersmith, H. Lee, Polydopamine Surface Chemistry: A Decade of Discovery, ACS Appl Mater Interfaces. 10 (2018) 7523–7540. https://doi.org/10.1021/acsami.7b19865.

[156] J. Liebscher, Chemistry of Polydopamine – Scope, Variation, and Limitation, European J Org Chem. 2019 (2019) 4976–4994. https://doi.org/10.1002/ejoc.201900445.

[157] J. Wang, B. Li, Z. Li, K. Ren, L. Jin, S. Zhang, H. Chang, Y. Sun, J. Ji, Electropolymerization of dopamine for surface modification of complex-shaped cardiovascular stents, Biomaterials. 35 (2014) 7679–7689. https://doi.org/10.1016/j.biomaterials.2014.05.047.

[158] Q. Lyu, N. Hsueh, C.L.L. Chai, Unravelling the polydopamine mystery: is the end in sight?, Polym Chem. 10 (2019) 5771–5777. https://doi.org/10.1039/C9PY01372E.

[159] L.C. Almeida, R.D. Correia, A. Marta, G. Squillaci, A. Morana, F. la Cara, J.P. Correia, A.S. Viana, Electrosynthesis of polydopamine films - tailored matrices for laccase-based biosensors, Appl Surf Sci. 480 (2019) 979–989. https://doi.org/10.1016/j.apsusc.2019.03.015.

[160] I. Ismail, T. Okajima, S. Kawauchi, T. Ohsaka, Studies on the early oxidation process of dopamine by electrochemical measurements and quantum chemical calculations, Electrochim Acta. 211 (2016) 777–786. https://doi.org/10.1016/j.electacta.2016.05.056.

[161] N.P. Gule, N.M. Begum, B. Klumperman, Advances in biofouling mitigation: A review, Crit Rev Environ Sci Technol. 46 (2016) 535–555. https://doi.org/10.1080/10643389.2015.1114444.

[162] H. Liu, X. Qu, H. Tan, J. Song, M. Lei, E. Kim, G.F. Payne, C. Liu, Role of polydopamine's redox-activity on its pro-oxidant, radical-scavenging, and antimicrobial activities, Acta Biomater. 88 (2019) 181–196. https://doi.org/10.1016/j.actbio.2019.02.032.

[163] K. Patel, N. Singh, J. Yadav, J.M. Nayak, S.K. Sahoo, J. Lata, D. Chand, S. Kumar, R. Kumar, Polydopamine films change their physicochemical and antimicrobial properties with a change in reaction conditions, Phys Chem Chem Phys. 20 (2018) 5744–5755. https://doi.org/10.1039/C7CP08406D.

[164] B. Stöckle, D.Y.W. Ng, C. Meier, T. Paust, F. Bischoff, T. Diemant, R.Jürgen. Behm, K.-E. Gottschalk, U. Ziener, T. Weil, Precise Control of Polydopamine Film Formation by Electropolymerization, Macromol Symp. 346 (2014) 73–81. https://doi.org/10.1002/masy.201400130.

[165] G. Loget, J.B. Wood, K. Cho, A.R. Halpern, R.M. Corn, Electrodeposition of Polydopamine Thin Films for DNA Patterning and Microarrays, Anal Chem. 85 (2013) 9991–9995. https://doi.org/10.1021/ac4022743.

[166] C. Xie, X. Lu, K. Wang, H. Yuan, L. Fang, X. Zheng, C. Chan, F. Ren, C. Zhao, Pulse Electrochemical Driven Rapid Layer-by-Layer Assembly of Polydopamine and Hydroxyapatite Nanofilms via Alternative Redox in Situ Synthesis for Bone

Regeneration, ACS Biomater Sci Eng. 2 (2016) 920–928. https://doi.org/10.1021/acsbiomaterials.6b00015.

[167] S. Daboss, J. Lin, M. Godejohann, C. Kranz, Redox Switchable Polydopamine-Modified AFM-SECM Probes: A Probe for Electrochemical Force Spectroscopy, Anal Chem. 92 (2020) 8404–8413. https://doi.org/10.1021/acs.analchem.0c00995.

[168] S. Li, H. Wang, M. Young, F. Xu, G. Cheng, H. Cong, Properties of Electropolymerized Dopamine and Its Analogues, Langmuir. 35 (2019) 1119–1125. https://doi.org/10.1021/acs.langmuir.8b01444.

[169] L.C. Almeida, R.D. Correia, B. Palys, J.P. Correia, A.S. Viana, Comprehensive study of the electrochemical growth and physicochemical properties of polycatecholamines and polycatechol, Electrochim Acta. 386 (2021) 138515. https://doi.org/10.1016/j.electacta.2021.138515.

[170] G. Tan, Y. Liu, Y. Wu, K. Ouyang, L. Zhou, P. Yu, J. Liao, C. Ning, Electrically Reversible Redox-Switchable Polydopamine Films for Regulating Cell Behavior, Electrochim Acta. 228 (2017) 343–350. https://doi.org/10.1016/j.electacta.2016.12.189.

[171] Y. Zhu, L. Yao, W. Weng, K. Cheng, Redox State of PDA Directs Cellular Responses through Preadsorbed Protein, ACS Biomater Sci Eng. 5 (2019) 553–560. https://doi.org/10.1021/acsbiomaterials.8b00987.

[172] V. Ball, Impedance spectroscopy and zeta potential titration of dopa-melanin films produced by oxidation of dopamine, Colloids Surf A Physicochem Eng Asp. 363 (2010) 92–97. https://doi.org/10.1016/j.colsurfa.2010.04.020.

[173] V. Ball, J. Gracio, M. Vila, M.K. Singh, M.-H. Metz-Boutigue, M. Michel, J. Bour, V. Toniazzo, D. Ruch, M.J. Buehler, Comparison of Synthetic Dopamine–Eumelanin Formed in the Presence of Oxygen and Cu 2+ Cations as Oxidants, Langmuir. 29 (2013) 12754–12761. https://doi.org/10.1021/la4029782.

[174] J. Wang, A.J. Bard, Monitoring DNA Immobilization and Hybridization on Surfaces by Atomic Force Microscopy Force Measurements, Anal Chem. 73 (2001) 2207–2212. https://doi.org/10.1021/ac001344a.

[175] S. Guo, X. Zhu, D. Jańczewski, S.S.C. Lee, T. He, S.L.M. Teo, G.J. Vancso, Measuring protein isoelectric points by AFM-based force spectroscopy using trace amounts of sample, Nat Nanotechnol. 11 (2016) 817–823. https://doi.org/10.1038/nnano.2016.118.

[176] D. v. Vezenov, A. Noy, L.F. Rozsnyai, C.M. Lieber, Force Titrations and Ionization State Sensitive Imaging of Functional Groups in Aqueous Solutions by Chemical

Force Microscopy, J Am Chem Soc. 119 (1997) 2006–2015. https://doi.org/10.1021/ja963375m.

[177] J. Pink, T. Smith-Palmer, D. Chisholm, T.J. Beveridge, D.A. Pink, An FTIR study of Pseudomonas aeruginosa PAO1 biofilm development: interpretation of ATR–FTIR data in the 1500–1180 cm −1 region, Biofilms. 2 (2005) 165–175. https://doi.org/10.1017/S1479050505001936.

[178] G. Caniglia, M.C. Sportelli, A. Heinzmann, R.A. Picca, A. Valentini, H. Barth, B. Mizaikoff, N. Cioffi, C. Kranz, Silver-fluoropolymer (Ag-CFX) films: Kinetic study of silver release, and spectroscopic-microscopic insight into the inhibition of P. fluorescens biofilm formation, Anal Chim Acta. 1212 (2022) 339892. https://doi.org/10.1016/j.aca.2022.339892.

[179] F. Quilès, F. Humbert, A. Delille, Analysis of changes in attenuated total reflection FTIR fingerprints of Pseudomonas fluorescens from planktonic state to nascent biofilm state, Spectrochim Acta A Mol Biomol Spectrosc. 75 (2010) 610–616. https://doi.org/10.1016/j.saa.2009.11.026.

[180] J. Haas, B. Mizaikoff, Advances in Mid-Infrared Spectroscopy for Chemical Analysis, Annu Rev Anal Chem. 9 (2016) 45–68. https://doi.org/10.1146/annurev-anchem-071015-041507.

[181] Á.I. López-Lorente, P. Wang, M. Sieger, E. Vargas Catalan, M. Karlsson, F. Nikolajeff, L. Österlund, B. Mizaikoff, Mid-infrared thin-film diamond waveguides combined with tunable quantum cascade lasers for analyzing the secondary structure of proteins, Phys Status Solidi A. 213 (2016) 2117–2123. https://doi.org/10.1002/pssa.201600134.

[182] A. Teuber, B. Mizaikoff, Cascade Laser Infrared Spectroscopy, in: Encyclopedia of Analytical Chemistry, Wiley, 2021: pp. 1–45. https://doi.org/10.1002/9780470027318.a9751.

[183] S. Mezzasalma, D. Baldovino, Characterization of Silicon Nitride Surface in Water and Acid Environment: A General Approach to the Colloidal Suspensions, J Colloid Interface Sci. 180 (1996) 413–420. https://doi.org/10.1006/jcis.1996.0320.

[184] R.M. Bock, B.J. McEntire, B.S. Bal, M.N. Rahaman, M. Boffelli, G. Pezzotti, Surface modulation of silicon nitride ceramics for orthopaedic applications, Acta Biomater. 26 (2015) 318–330. https://doi.org/10.1016/j.actbio.2015.08.014.

[185] J. Sonnefeld, Determination of surface charge density parameters of silicon nitride, Colloids Surf A Physicochem Eng Asp. 108 (1996) 27–31. https://doi.org/10.1016/0927-7757(95)03356-4.

[186] K. Lin, Z. Li, Y. Tao, K. Li, H. Yang, J. Ma, T. Li, J. Sha, Y. Chen, Surface Charge Density Inside a Silicon Nitride Nanopore, Langmuir. 37 (2021) 10521–10528. https://doi.org/10.1021/acs.langmuir.1c01504.

[187] F. Nikaido, S. Inasawa, Y. Tsuji, Y. Yamaguchi, A Model of Silica Dissolution Based on Acid Dissociation of Internal Silanol, Bull Chem Soc Jpn. 86 (2013) 520–525. https://doi.org/10.1246/bcsj.20120337.

[188] W. Schmickler, E. Santos, The metal-solution interface, in: Interfacial Electrochemistry, Springer Berlin Heidelberg, Berlin, Heidelberg, 2010: pp. 39–50. https://doi.org/10.1007/978-3-642-04937-8_5.

[189] K.E. Jarmusik, S.J. Eppell, D.J. Lacks, F.R. Zypman, Obtaining Charge Distributions on Geometrically Generic Nanostructures Using Scanning Force Microscopy, Langmuir. 27 (2011) 1803–1810. https://doi.org/10.1021/la104153p.

[190] R. Raiteri, B. Margesin, M. Grattarola, An atomic force microscope estimation of the point of zero charge of silicon insulators, Sens Actuators B Chem. 46 (1998) 126–132. https://doi.org/10.1016/S0925-4005(98)00098-7.

[191] S.E. Rollauer, M.A. Sooreshjani, N. Noinaj, S.K. Buchanan, Outer membrane protein biogenesis in Gram-negative bacteria, Philosophical Transactions of the Royal Society B: Biological Sciences. 370 (2015) 20150023. https://doi.org/10.1098/rstb.2015.0023.

[192] A. Ebbensgaard, H. Mordhorst, F.M. Aarestrup, E.B. Hansen, The Role of Outer Membrane Proteins and Lipopolysaccharides for the Sensitivity of Escherichia coli to Antimicrobial Peptides, Front Microbiol. 9 (2018). https://doi.org/10.3389/fmicb.2018.02153.

[193] P. di Martino, Extracellular polymeric substances, a key element in understanding biofilm phenotype, AIMS Microbiol. 4 (2018) 274–288. https://doi.org/10.3934/microbiol.2018.2.274.

[194] E. McGillicuddy, I. Murray, S. Kavanagh, L. Morrison, A. Fogarty, M. Cormican, P. Dockery, M. Prendergast, N. Rowan, D. Morris, Silver nanoparticles in the environment: Sources, detection and ecotoxicology, Sci Total Environ. 575 (2017) 231–246. https://doi.org/10.1016/j.scitotenv.2016.10.041.

[195] M.C. Lea, Allotropic forms of silver, Am J Sci. s3-37 (1889) 476–491. https://doi.org/10.2475/ajs.s3-37.222.476.

[196] The nanodatabase, (n.d.). https://nanodb.dk/en/ (accessed September 27, 2022).

[197] B. Nowack, H.F. Krug, M. Height, 120 Years of Nanosilver History: Implications for Policy Makers, Environ Sci Technol. 45 (2011) 1177–1183. https://doi.org/10.1021/es103316q.

[198] W. Sim, R. Barnard, M.A.T. Blaskovich, Z. Ziora, Antimicrobial Silver in Medicinal and Consumer Applications: A Patent Review of the Past Decade (2007–2017), Antibiotics. 7 (2018) 93. https://doi.org/10.3390/antibiotics7040093.

[199] X.-F. Zhang, Z.-G. Liu, W. Shen, S. Gurunathan, Silver Nanoparticles: Synthesis, Characterization, Properties, Applications, and Therapeutic Approaches, Int J Mol Sci. 17 (2016) 1534. https://doi.org/10.3390/ijms17091534.

[200] X. Duan, Y. Li, Physicochemical Characteristics of Nanoparticles Affect Circulation, Biodistribution, Cellular Internalization, and Trafficking, Small. 9 (2013) 1521–1532. https://doi.org/10.1002/smll.201201390.

[201] T.C. Dakal, A. Kumar, R.S. Majumdar, V. Yadav, Mechanistic Basis of Antimicrobial Actions of Silver Nanoparticles, Front Microbiol. 7 (2016). https://doi.org/10.3389/fmicb.2016.01831.

[202] R.K. Sharma, S. Yadav, S. Dutta, H.B. Kale, I.R. Warkad, R. Zbořil, R.S. Varma, M.B. Gawande, Silver nanomaterials: synthesis and (electro/photo) catalytic applications, Chem Soc Rev. 50 (2021) 11293–11380. https://doi.org/10.1039/D0CS00912A.

[203] S. Anees Ahmad, S. Sachi Das, A. Khatoon, M. Tahir Ansari, Mohd. Afzal, M. Saquib Hasnain, A. Kumar Nayak, Bactericidal activity of silver nanoparticles: A mechanistic review, Mater Sci Energy Technol. 3 (2020) 756–769. https://doi.org/10.1016/j.mset.2020.09.002.

[204] P. Iqbal, J.A. Preece, P.M. Mendes, Nanotechnology: The “Top-Down” and “Bottom-Up” Approaches, in: Supramol Chem, John Wiley & Sons, Ltd, Chichester, UK, 2012. https://doi.org/10.1002/9780470661345.smc195.

[205] M.J. Rak, T. Friščić, A. Moores, One-step, solvent-free mechanosynthesis of silver nanoparticle-infused lignin composites for use as highly active multidrug resistant antibacterial filters, RSC Adv. 6 (2016) 58365–58370. https://doi.org/10.1039/C6RA03711A.

[206] G.R. KHAYATI, K. JANGHORBAN, Preparation of nanostructure silver powders by mechanical decomposing and mechanochemical reduction of silver oxide, Trans of Nonferrous Met Soc China. 23 (2013) 1520–1524. https://doi.org/10.1016/S1003-6326(13)62625-4.

[207] T. Tsuji, K. Iryo, N. Watanabe, M. Tsuji, Preparation of silver nanoparticles by laser ablation in solution: influence of laser wavelength on particle size, Appl Surf Sci. 202 (2002) 80–85. https://doi.org/10.1016/S0169-4332(02)00936-4.

[208] A.I. López-Lorente, R.A. Picca, J. Izquierdo, C. Kranz, B. Mizaikoff, C. di Franco, S. Cárdenas, N. Cioffi, G. Palazzo, A. Valentini, Ion beam sputtering deposition of

silver nanoparticles and TiOx/ZnO nanocomposites for use in surface enhanced vibrational spectroscopy (SERS and SEIRAS), Microchim Acta. 185 (2018) 153. https://doi.org/10.1007/s00604-018-2708-7.

[209] Y. Sun, Y. Xia, Shape-Controlled Synthesis of Gold and Silver Nanoparticles, Science (1979). 298 (2002) 2176–2179. https://doi.org/10.1126/science.1077229.

[210] C. Xue, C.A. Mirkin, pH-Switchable Silver Nanoprism Growth Pathways, Angewandte Chemie Int Ed. 119 (2007) 2082–2084. https://doi.org/10.1002/ange.200604637.

[211] Z. Zaheer, Rafiuddin, Multi-branched flower-like silver nanoparticles: Preparation and characterization, Colloids Surf A Physicochem Eng Asp. 384 (2011) 427–431. https://doi.org/10.1016/j.colsurfa.2011.04.030.

[212] H. Liang, W. Wang, Y. Huang, S. Zhang, H. Wei, H. Xu, Controlled Synthesis of Uniform Silver Nanospheres, J Phys Chem C. 114 (2010) 7427–7431. https://doi.org/10.1021/jp9105713.

[213] S. Zhou, J. Li, K.D. Gilroy, J. Tao, C. Zhu, X. Yang, X. Sun, Y. Xia, Facile Synthesis of Silver Nanocubes with Sharp Corners and Edges in an Aqueous Solution, ACS Nano. 10 (2016) 9861–9870. https://doi.org/10.1021/acsnano.6b05776.

[214] D. Bamal, A. Singh, G. Chaudhary, M. Kumar, M. Singh, N. Rani, P. Mundlia, A.R. Sehrawat, Silver Nanoparticles Biosynthesis, Characterization, Antimicrobial Activities, Applications, Cytotoxicity and Safety Issues: An Updated Review, Nanomaterials. 11 (2021) 2086. https://doi.org/10.3390/nano11082086.

[215] V.C. Karade, R.B. Patil, S.B. Parit, J.H. Kim, A.D. Chougale, V.V. Dawkar, Insights into Shape-Based Silver Nanoparticles: A Weapon to Cope with Pathogenic Attacks, ACS Sustain Chem Eng. 9 (2021) 12476–12507. https://doi.org/10.1021/acssuschemeng.1c03797.

[216] D. Hebbalalu, J. Lalley, M.N. Nadagouda, R.S. Varma, Greener Techniques for the Synthesis of Silver Nanoparticles Using Plant Extracts, Enzymes, Bacteria, Biodegradable Polymers, and Microwaves, ACS Sustain Chem Eng. 1 (2013) 703–712. https://doi.org/10.1021/sc4000362.

[217] M. Saravanan, S.K. Barik, D. MubarakAli, P. Prakash, A. Pugazhendhi, Synthesis of silver nanoparticles from Bacillus brevis (NCIM 2533) and their antibacterial activity against pathogenic bacteria, Microb Pathog. 116 (2018) 221–226. https://doi.org/10.1016/j.micpath.2018.01.038.

[218] L. Rodríguez-Sánchez, M.C. Blanco, M.A. López-Quintela, Electrochemical Synthesis of Silver Nanoparticles, J Phys Chem B. 104 (2000) 9683–9688. https://doi.org/10.1021/jp001761r.

[219] B.J. Wiley, S.H. Im, Z.-Y. Li, J. McLellan, A. Siekkinen, Y. Xia, Maneuvering the Surface Plasmon Resonance of Silver Nanostructures through Shape-Controlled Synthesis, J Phys Chem B. 110 (2006) 15666–15675. https://doi.org/10.1021/jp0608628.

[220] I. Washio, Y. Xiong, Y. Yin, Y. Xia, Reduction by the End Groups of Poly(vinyl pyrrolidone): A New and Versatile Route to the Kinetically Controlled Synthesis of Ag Triangular Nanoplates, Adv Mat. 18 (2006) 1745–1749. https://doi.org/10.1002/adma.200600675.

[221] D. Ibañez, C. Fernandez-Blanco, A. Heras, A. Colina, Time-Resolved Study of the Surface-Enhanced Raman Scattering Effect of Silver Nanoparticles Generated in Voltammetry Experiments., J Phys Chem C. 118 (2014) 23426–23433. https://doi.org/10.1021/jp5074363.

[222] M. Starowicz, B. Stypuła, J. Banaś, Electrochemical synthesis of silver nanoparticles, Electrochem Commun. 8 (2006) 227–230. https://doi.org/10.1016/j.elecom.2005.11.018.

[223] J. Bian, Z. Li, Z. Chen, X. Zhang, Q. Li, S. Jiang, J. He, G. Han, Double-potentiostatic electrodeposition of Ag nanoflowers on ITO glass for reproducible surface-enhanced (resonance) Raman scattering application, Electrochim Acta. 67 (2012) 12–17. https://doi.org/10.1016/j.electacta.2012.01.073.

[224] J.-C. Bian, Z. Li, Z.-D. Chen, H.-Y. He, X.-W. Zhang, X. Li, G.-R. Han, Electrodeposition of silver nanoparticle arrays on ITO coated glass and their application as reproducible surface-enhanced Raman scattering substrate, Appl Surf Sci. 258 (2011) 1831–1835. https://doi.org/10.1016/j.apsusc.2011.10.055.

[225] F. Bensebaa, Dry Production Methods, in: Interface Science and Technology, Elsevier, 2013: pp. 147–184. https://doi.org/10.1016/B978-0-12-369550-5.00003-3.

[226] V. Teixeira, J. Carneiro, P. Carvalho, E. Silva, S. Azevedo, C. Batista, High barrier plastics using nanoscale inorganic films, in: Multifunctional and Nanoreinforced Polymers for Food Packaging, Elsevier, 2011: pp. 285–315. https://doi.org/10.1533/9780857092786.1.285.

[227] D.M. Mattox, Physical Sputtering and Sputter Deposition (Sputtering), in: Handbook of Physical Vapor Deposition (PVD) Processing, Elsevier, 2010: pp. 237–286. https://doi.org/10.1016/B978-0-8155-2037-5.00007-1.

[228] T. Makowski, D. Kowalczyk, W. Fortuniak, S. Brzezinski, D. Kregiel, Electrochemical deposition of silver nanoparticle and polymerization of pyrrole on

fabrics via conducting multiwall carbon nanotubes, Cellulose. 22 (2015) 3063–3075. https://doi.org/10.1007/s10570-015-0725-9.

[229] A. Moradi Golsheikh, N.M. Huang, H.N. Lim, R. Zakaria, C.-Y. Yin, One-step electrodeposition synthesis of silver-nanoparticle-decorated graphene on indium-tin-oxide for enzymeless hydrogen peroxide detection, Carbon N Y. 62 (2013) 405–412. https://doi.org/10.1016/j.carbon.2013.06.025.

[230] L. Guo, G. Oskam, A. Radisic, P.M. Hoffmann, P.C. Searson, Island growth in electrodeposition, J Phys D Appl Phys. 44 (2011) 443001. https://doi.org/10.1088/0022-3727/44/44/443001.

[231] M.H. Mamme, E.A. Mernissi Cherigui, O. Dolgikh, J. Ustarroz, H. Simillion, H. Terryn, J. Deconinck, A Finite Element Simulation of the Electrochemical Growth of a Single Hemispherical Silver Nucleus, Electrochim Acta. 197 (2016) 307–317. https://doi.org/10.1016/j.electacta.2015.12.035.

[232] N. Durán, M. Durán, M.B. de Jesus, A.B. Seabra, W.J. Fávaro, G. Nakazato, Silver nanoparticles: A new view on mechanistic aspects on antimicrobial activity, Nanomedicine. 12 (2016) 789–799. https://doi.org/10.1016/j.nano.2015.11.016.

[233] J.A. Lemire, J.J. Harrison, R.J. Turner, Antimicrobial activity of metals: mechanisms, molecular targets and applications, Nat Rev Microbiol. 11 (2013) 371–384. https://doi.org/10.1038/nrmicro3028.

[234] A. Abbaszadegan, Y. Ghahramani, A. Gholami, B. Hemmateenejad, S. Dorostkar, M. Nabavizadeh, H. Sharghi, The Effect of Charge at the Surface of Silver Nanoparticles on Antimicrobial Activity against Gram-Positive and Gram-Negative Bacteria: A Preliminary Study, J Nanomater. 2015 (2015) 1–8. https://doi.org/10.1155/2015/720654.

[235] J. Said, C.C. Dodoo, M. Walker, D. Parsons, P. Stapleton, A.E. Beezer, S. Gaisford, An in vitro test of the efficacy of silver-containing wound dressings against Staphylococcus aureus and Pseudomonas aeruginosa in simulated wound fluid, Int J Pharm. 462 (2014) 123–128. https://doi.org/10.1016/j.ijpharm.2013.12.037.

[236] S. Tang, J. Zheng, Antibacterial Activity of Silver Nanoparticles: Structural Effects, Adv Healthc Mater. 7 (2018) 1701503. https://doi.org/10.1002/adhm.201701503.

[237] Y.-M. Long, L.-G. Hu, X.-T. Yan, X.-C. Zhao, Q.-F. Zhou, Y. Cai, G.-B. Jiang, Surface ligand controls silver ion release of nanosilver and its antibacterial activity against Escherichia coli, Int J Nanomedicine. Volume 12 (2017) 3193–3206. https://doi.org/10.2147/IJN.S132327.

[238] C. Gasbarri, M. Ronci, A. Aceto, R. Vasani, G. Iezzi, T. Florio, F. Barbieri, G. Angelini, L. Scotti, Structure and Properties of Electrochemically Synthesized Silver

Nanoparticles in Aqueous Solution by High-Resolution Techniques, Molecules. 26 (2021) 5155. https://doi.org/10.3390/molecules26175155.

[239] X. Li, J.J. Lenhart, H.W. Walker, Aggregation Kinetics and Dissolution of Coated Silver Nanoparticles, Langmuir. 28 (2012) 1095–1104. https://doi.org/10.1021/la202328n.

[240] N. Durán, M. Durán, M.B. de Jesus, A.B. Seabra, W.J. Fávaro, G. Nakazato, Silver nanoparticles: A new view on mechanistic aspects on antimicrobial activity, Nanomedicine. 12 (2016) 789–799. https://doi.org/10.1016/j.nano.2015.11.016.

[241] T.J. Silhavy, D. Kahne, S. Walker, The Bacterial Cell Envelope, Cold Spring Harb Perspect Biol. 2 (2010) a000414–a000414. https://doi.org/10.1101/cshperspect.a000414.

[242] S. Pal, Y.K. Tak, J.M. Song, Does the Antibacterial Activity of Silver Nanoparticles Depend on the Shape of the Nanoparticle? A Study of the Gram-Negative Bacterium Escherichia coli, Appl Environ Microbiol. 73 (2007) 1712–1720. https://doi.org/10.1128/AEM.02218-06.

[243] W.-R. Li, X.-B. Xie, Q.-S. Shi, H.-Y. Zeng, Y.-S. OU-Yang, Y.-B. Chen, Antibacterial activity and mechanism of silver nanoparticles on Escherichia coli, Appl Microbiol Biotechnol. 85 (2010) 1115–1122. https://doi.org/10.1007/s00253-009-2159-5.

[244] O. Bondarenko, A. Ivask, A. Käkinen, I. Kurvet, A. Kahru, Particle-Cell Contact Enhances Antibacterial Activity of Silver Nanoparticles, PLoS One. 8 (2013) e64060. https://doi.org/10.1371/journal.pone.0064060.

[245] I. Sondi, B. Salopek-Sondi, Silver nanoparticles as antimicrobial agent: a case study on E. coli as a model for Gram-negative bacteria, J Colloid Interface Sci. 275 (2004) 177–182. https://doi.org/10.1016/j.jcis.2004.02.012.

[246] S. Rajesh, V. Dharanishanthi, A.V. Kanna, Antibacterial mechanism of biogenic silver nanoparticles of Lactobacillus acidophilus, J Exp Nanosci. 10 (2015) 1143–1152. https://doi.org/10.1080/17458080.2014.985750.

[247] Chwalibog, Chwalibog, Sawosz, Hotowy, Szeliga, S. Mitura, K. Mitura, Grodzik, MSc Orlowski, Professor Sokolowska, Visualization of interaction between inorganic nanoparticles and bacteria or fungi, Int J Nanomedicine. (2010) 1085. https://doi.org/10.2147/IJN.S13532.

[248] G. McDonnell, A.D. Russell, Antiseptics and Disinfectants: Activity, Action, and Resistance, Clin Microbiol Rev. 12 (1999) 147–179. https://doi.org/10.1128/CMR.12.1.147.

[249] J.-H.J.S. Kim, E. Kuk, K.N. Yu, J.-H.J.S. Kim, S.J. Park, H.J. Lee, S.H. Kim, Y.H.Y.K. Park, Y.H.Y.K. Park, C.-Y. Hwang, Y.-K. Kim, Y.-S. Lee, D.H. Jeong, M.-

H. Cho, Antimicrobial effects of silver nanoparticles, Nanomedicine. 3 (2007) 95–101. https://doi.org/10.1016/j.nano.2006.12.001.

[250] I. Fenoglio, I. Corazzari, C. Francia, S. Bodoardo, B. Fubini, The oxidation of glutathione by cobalt/tungsten carbide contributes to hard metal-induced oxidative stress, Free Radic Res. 42 (2008) 437–745. https://doi.org/10.1080/10715760802350904.

[251] K. Rahman, Studies on free radicals, antioxidants, and co-factors., Clin Interv Aging. 2 (2007) 219–36. http://www.ncbi.nlm.nih.gov/pubmed/18044138.

[252] S. Liao, Y. Zhang, X. Pan, F. Zhu, C. Jiang, Q. Liu, Z. Cheng, G. Dai, G. Wu, L. Wang, L. Chen, Antibacterial activity and mechanism of silver nanoparticles against multidrug-resistant Pseudomonas aeruginosa, Int J Nanomedicine. Volume 14 (2019) 1469–1487. https://doi.org/10.2147/IJN.S191340.

[253] S. Nakamura, N. Ando, M. Sato, M. Ishihara, Ultraviolet Irradiation Enhances the Microbicidal Activity of Silver Nanoparticles by Hydroxyl Radicals, Int J Mol Sci. 21 (2020) 3204. https://doi.org/10.3390/ijms21093204.

[254] M.E. Quadros, L.C. Marr, Silver Nanoparticles and Total Aerosols Emitted by Nanotechnology-Related Consumer Spray Products, Environ Sci Technol. 45 (2011) 10713–10719. https://doi.org/10.1021/es202770m.

[255] X. Chen, H.J. Schluesener, Nanosilver: A nanoproduct in medical application, Toxicol Lett. 176 (2008) 1–12. https://doi.org/10.1016/j.toxlet.2007.10.004.

[256] P. Slepicka, N.S. Kasalkova, J. Siegel, Z. Kolska, L. Bacakova, V. Svorcik, Nano-structured and functionalized surfaces for cytocompatibility improvement and bactericidal action, Biotechnol Adv. 33 (2015) 1120–1129. https://doi.org/10.1016/j.biotechadv.2015.01.001.

[257] S.G. Lee, D.S. Ham, D.Y. Lee, H. Bong, K. Cho, Transparent Superhydrophobic/Translucent Superamphiphobic Coatings Based on Silica–Fluoropolymer Hybrid Nanoparticles, Langmuir. 29 (2013) 15051–15057. https://doi.org/10.1021/la404005b.

[258] M.C. Sportelli, M.A. Nitti, M. Valentini, R.A. Picca, E. Bonerba, L. Sabbatini, G. Tantillo, N. Cioffi, A. Valentini, Ion Beam Sputtering Deposition and Characterization of ZnO-Fluoropolymer Nano-Antimicrobials, Sci Adv Mater. 6 (2014) 1019–1025. https://doi.org/10.1166/sam.2014.1852.

[259] S. Yuan, S.O. Pehkonen, B. Liang, Y.P. Ting, K.G. Neoh, E.T. Kang, Superhydrophobic fluoropolymer-modified copper surface via surface graft polymerisation for corrosion protection, Corros Sci. 53 (2011) 2738–2747. https://doi.org/10.1016/j.corsci.2011.05.008.

[260] N. Cioffi, N. Ditaranto, L. Torsi, R.A. Picca, L. Sabbatini, A. Valentini, L. Novello, G. Tantillo, T. Bleve-Zacheo, P.G. Zambonin, Analytical characterization of bioactive fluoropolymer ultra-thin coatings modified by copper nanoparticles, Anal Bioanal Chem. 381 (2005) 607–616. https://doi.org/10.1007/s00216-004-2761-4.

[261] B. Kang, L.W. Tan, S.R.P. Silva, Fluoropolymer indium-tin-oxide buffer layers for improved power conversion in organic photovoltaics, Appl Phys Lett. 93 (2008) 133302. https://doi.org/10.1063/1.2983742.

[262] M. Sportelli, M. Valentini, R. Picca, A. Milella, A. Nacci, A. Valentini, N. Cioffi, New Insights in the Ion Beam Sputtering Deposition of ZnO-Fluoropolymer Nanocomposites, Appl Sci. 8 (2018) 77. https://doi.org/10.3390/app8010077.

[263] F. Quaranta, A. Valentini, P. Favia, R. Lamendola, R. D'Agostino, Ion-beam sputtering deposition of fluoropolymer thin films, Appl Phys Lett. 63 (1993) 10–11. https://doi.org/10.1063/1.109729.

[264] M.C. Sportelli, E. Tütüncü, R.A. Picca, M. Valentini, A. Valentini, C. Kranz, B. Mizaikoff, H. Barth, N. Cioffi, Inhibiting P. fluorescens biofilms with fluoropolymer-embedded silver nanoparticles: an in-situ spectroscopic study, Sci Rep. 7 (2017) 11870. https://doi.org/10.1038/s41598-017-12088-x.

[265] V.K. Kaushik, XPS core level spectra and Auger parameters for some silver compounds, J Electron Spectros Relat Phenomena. 56 (1991) 273–277. https://doi.org/10.1016/0368-2048(91)85008-H.

[266] P.W. Wang, Y. Jiang, J.-C. Hsu, Y.-Y. Chen, Y.-H. Lin, H.-L. Chen, Thermal Effect on Structure of Silver in Ion-Exchanged Soda-Lime Glasses and Aluminum-Doped Zinc Oxide Films, Adv Mater Sci Eng. 2011 (2011) 1–7. https://doi.org/10.1155/2011/987671.

[267] B. Abduali, T. Elmira, T. Ainur, Electrochemical Behavior of Silver in Sodium Sulphate Solution during Anodic Polarization Revisited, Orient J Chem. 29 (2013) 33–37. https://doi.org/10.13005/ojc/290105.

[268] S.S. Abd El Rehim, H.H. Hassan, M.A.M. Ibrahim, M.A. Amin, Electrochemical Behaviour of a Silver Electrode in NaOH Solutions, Monatsh Chem. 129 (1998) 1103–1117. https://doi.org/10.1007/PL00010123.

[269] N.A. Hampson, J.B. Lee, J.R. Morley, The electrochemistry of oxides of silver—a short review, Electrochim Acta. 16 (1971) 637–642. https://doi.org/10.1016/0013-4686(71)85174-5.

[270] R. Cornut, C. Lefrou, A unified new analytical approximation for negative feedback currents with a microdisk SECM tip, J Electroanal Chem. 608 (2007) 59–66. https://doi.org/10.1016/j.jelechem.2007.05.007.

[271] M.L. Bruschi, Mathematical models of drug release, in: Strategies to Modify the Drug Release from Pharmaceutical Systems, Elsevier, 2015: pp. 63–86. https://doi.org/10.1016/B978-0-08-100092-2.00005-9.

[272] A. el Afif, M. Grmela, Non-Fickian mass transport in polymers, J Rheol (N Y N Y). 46 (2002) 591–628. https://doi.org/10.1122/1.1470520.

[273] J. Siepmann, Modeling of drug release from delivery systems based on hydroxypropyl methylcellulose (HPMC), Adv Drug Deliv Rev. 48 (2001) 139–157. https://doi.org/10.1016/S0169-409X(01)00112-0.

[274] C. Radheshkumar, H. Münstedt, Antimicrobial polymers from polypropylene/silver composites—Ag+ release measured by anode stripping voltammetry, React Funct Polym. 66 (2006) 780–788. https://doi.org/10.1016/j.reactfunctpolym.2005.11.005.

[275] C. Damm, H. Münstedt, Kinetic aspects of the silver ion release from antimicrobial polyamide/silver nanocomposites, Appl Phys A. 91 (2008) 479–486. https://doi.org/10.1007/s00339-008-4434-1.

[276] M.H. Kim, T.-H. Kim, J.A. Ko, S. Ko, J.-M. Oh, H.J. Park, Kinetic and thermodynamic studies of silver migration from nanocomposites, J Food Eng. 243 (2019) 1–8. https://doi.org/10.1016/j.jfoodeng.2018.08.028.

[277] G. Marletta, Chemical reactions and physical property modifications induced by keV ion beams in polymers, Nucl Instrum Methods Phys Res B. 46 (1990) 295–305. https://doi.org/10.1016/0168-583X(90)90716-8.

[278] L. Calcagno, G. Compagnini, G. Foti, Structural modification of polymer films by ion irradiation, Nucl Instrum Methods Phys Res B. 65 (1992) IN7-422. https://doi.org/10.1016/0168-583X(92)95077-5.

[279] A. Kondyurin, M. Bilek, Interactions of energetic ions with polymers: chemical picture, in: Ion Beam Treatment of Polymers, Elsevier, 2015: pp. 29–67. https://doi.org/10.1016/B978-0-08-099445-1.00003-1.

[280] A. Kondyurin, M. Bilek, Structure of polymers after ion beam treatment, in: Ion Beam Treatment of Polymers, Elsevier, 2015: pp. 69–127. https://doi.org/10.1016/B978-0-08-099445-1.00004-3.

[281] J.J. Dynes, J.R. Lawrence, D.R. Korber, G.D.W. Swerhone, G.G. Leppard, A.P. Hitchcock, Morphological and biochemical changes in Pseudomonas fluorescens biofilms induced by sub-inhibitory exposure to antimicrobial agents, Can J Microbiol. 55 (2009) 163–178. https://doi.org/10.1139/W08-109.

[282] L.S. van Overbeek, L. Eberl, M. Givskov, S. Molin, J.D. van Elsas, Survival of, and induced stress resistance in, carbon-starved Pseudomonas fluorescens cells

residing in soil, Appl Environ Microbiol. 61 (1995) 4202–4208. https://doi.org/10.1128/aem.61.12.4202-4208.1995.

[283] E. Cefalì, S. Patanè, A. Arena, G. Saitta, S. Guglielmino, S. Cappello, M. Nicolò, M. Allegrini, Morphologic variations in bacteria under stress conditions: Near- field optical studies, Scanning. 24 (2006) 274–283. https://doi.org/10.1002/sca.4950240601.

[284] P. Cardoso, H. Glossop, T.G. Meikle, A. Aburto-Medina, C.E. Conn, V. Sarojini, C. Valery, Molecular engineering of antimicrobial peptides: microbial targets, peptide motifs and translation opportunities, Biophys Rev. 13 (2021) 35–69. https://doi.org/10.1007/s12551-021-00784-y.

[285] H. Nikaido, Multidrug Resistance in Bacteria, Annu Rev Biochem. 78 (2009) 119–146. https://doi.org/10.1146/annurev.biochem.78.082907.145923.

[286] G.G. Anderson, G.A. O'Toole, Innate and Induced Resistance Mechanisms of Bacterial Biofilms, in: Bacterial Biofilms, Springer Berlin Heidelberg, 2008: pp. 85–105. https://doi.org/10.1007/978-3-540-75418-3_5.

[287] S. Agnihotri, S. Mukherji, S. Mukherji, Size-controlled silver nanoparticles synthesized over the range 5–100 nm using the same protocol and their antibacterial efficacy, RSC Adv. 4 (2014) 3974–3983. https://doi.org/10.1039/C3RA44507K.

[288] C. Quintero-Quiroz, L.E. Botero, D. Zárate-Triviño, N. Acevedo-Yepes, J.S. Escobar, V.Z. Pérez, L.J. Cruz Riano, Synthesis and characterization of a silver nanoparticle-containing polymer composite with antimicrobial abilities for application in prosthetic and orthotic devices, Biomater Res. 24 (2020) 13. https://doi.org/10.1186/s40824-020-00191-6.

[289] T. Wang, Wusigale, D. Kuttappan, M.A. Amalaradjou, Y. Luo, Y. Luo, Polydopamine-coated chitosan hydrogel beads for synthesis and immobilization of silver nanoparticles to simultaneously enhance antimicrobial activity and adsorption kinetics, Adv Compos Hybrid Mater. 4 (2021) 696–706. https://doi.org/10.1007/s42114-021-00305-1.

[290] I. Osório, R. Igreja, R. Franco, J. Cortez, Incorporation of silver nanoparticles on textile materials by an aqueous procedure, Mater Lett. 75 (2012) 200–203. https://doi.org/10.1016/j.matlet.2012.02.024.

[291] S. Hemmati, Z. Joshani, A. Zangeneh, M.M. Zangeneh, Biosynthesis and chemical characterization of polydopamine-capped silver nanoparticles for the treatment of acute myeloid leukemia in comparison to doxorubicin in a leukemic mouse model, Appl Organomet Chem. 34 (2020). https://doi.org/10.1002/aoc.5277.

[292] I.I. Niyonshuti, V.R. Krishnamurthi, D. Okyere, L. Song, M. Benamara, X. Tong, Y. Wang, J. Chen, Polydopamine Surface Coating Synergizes the Antimicrobial Activity of Silver Nanoparticles, ACS Appl Mater Interfaces. 12 (2020) 40067–40077. https://doi.org/10.1021/acsami.0c10517.

[293] D. Wang, L. Bao, H. Li, X. Guo, W. Liu, X. Wang, X. Hou, B. He, Polydopamine stabilizes silver nanoparticles as a SERS substrate for efficient detection of myocardial infarction, Nanoscale. 14 (2022) 6212–6219. https://doi.org/10.1039/D2NR00091A.

[294] A. GhavamiNejad, L.E. Aguilar, R.B. Ambade, S.-H. Lee, C.H. Park, C.S. Kim, Immobilization of silver nanoparticles on electropolymerized polydopamine films for metal implant applications, Colloids Interface Sci Commun. 6 (2015) 5–8. https://doi.org/10.1016/j.colcom.2015.08.001.

[295] J. Lu, J. Fang, J. Li, C. Wang, Z. He, L. Zhu, Z. Xu, H. Zeng, Polydopamine Nanotubes Decorated with Ag Nanoparticles as Catalyst for the Reduction of Methylene Blue, ACS Appl Nano Mater. 3 (2020) 156–164. https://doi.org/10.1021/acsanm.9b01861.

[296] A. Kumar, B. Mishra, B.P. Tripathi, Polydopamine assisted synthesis of ultrafine silver nanoparticles for heterogeneous catalysis and water remediation, Nano-Struct Nano-Objects. 23 (2020) 100489. https://doi.org/10.1016/j.nanoso.2020.100489.

[297] K. Fajerwerg, V. Ynam, B. Chaudret, V. Garçon, D. Thouron, M. Comtat, An original nitrate sensor based on silver nanoparticles electrodeposited on a gold electrode, Electrochem Commun. 12 (2010) 1439–1441. https://doi.org/10.1016/j.elecom.2010.08.003.

[298] D. Ibañez, D. Izquierdo, C. Fernandez-Blanco, A. Heras, A. Colina, Electrodeposition of silver nanoparticles in the presence of different complexing agents by time-resolved Raman spectroelectrochemistry, J of Raman Spectrosc. 49 (2018) 482–492. https://doi.org/10.1002/jrs.5307.

[299] D. Zhang, Y. Tang, F. Jiang, Z. Han, J. Chen, Electrodeposition of silver nanoparticle arrays on transparent conductive oxides, Appl Surf Sci. 369 (2016) 178–182. https://doi.org/10.1016/j.apsusc.2016.02.059.

[300] D.A. Crespo-Yapur, A.S. Elizondo, D. Herrera, M. Videa, Galvanostatic electrodeposition of silver nanoparticles: Nucleation and growth studies, Mater Today Proc. 48 (2022) 1–4. https://doi.org/10.1016/j.matpr.2020.04.760.

[301] B.-A. Zhao, W.-F. Cai, K.-B. Pu, J.-R. Bai, J.-Y. Gao, Y.-H. Wang, Electrochemical deposition of flower-like nanostructured silver particles with a PVA modified carbon

cloth cathode, RSC Adv. 12 (2022) 21793–21800. https://doi.org/10.1039/D2RA02495K.

[302] A. Alqudami, S. Annapoorni, P. Sen, R.S. Rawat, The incorporation of silver nanoparticles into polypyrrole: Conductivity changes, Synth Met. 157 (2007) 53–59. https://doi.org/10.1016/j.synthmet.2006.12.006.

[303] J. Pan, Z. Zhang, Z. Zhan, Y. Xiong, Y. Wang, K. Cao, Y. Chen, In situ generation of silver nanoparticles and nanocomposite films based on electrodeposition of carboxylated chitosan, Carbohydr Polym. 242 (2020) 116391. https://doi.org/10.1016/j.carbpol.2020.116391.

[304] L. Heerman, A. Tarallo, Theory of the chronoamperometric transient for electrochemical nucleation with diffusion-controlled growth, J Electroanal Chem. 470 (1999) 70–76. https://doi.org/10.1016/S0022-0728(99)00221-1.

[305] B. Scharifker, G. Hills, Theoretical and experimental studies of multiple nucleation, Electrochim Acta. 28 (1983) 879–889. https://doi.org/10.1016/0013-4686(83)85163-9.

[306] M.H. Mamme, J. Deconinck, J. Ustarroz, Transition between kinetic and diffusion control during the initial stages of electrochemical growth using numerical modelling, Electrochim Acta. 258 (2017) 662–668. https://doi.org/10.1016/j.electacta.2017.11.111.

[307] M. Fleischmann, S. Pons, J. Sousa, J. Ghoroghchian, Electrodeposition and electrocatalysis: The deposition and dissolution of single catalyst centres, J Electroanal Chem. 366 (1994) 171–190. https://doi.org/10.1016/0022-0728(93)02738-4.

[308] H.S. Harned, C.L. Hildreth, The Diffusion Coefficient of Silver Nitrate in Dilute Aqueous Solution at 25°, J Am Chem Soc. 73 (1951) 3292–3293. https://doi.org/10.1021/ja01151a088.

[309] M.E. Snowden, A.G. Güell, S.C.S. Lai, K. McKelvey, N. Ebejer, M.A. O'Connell, A.W. Colburn, P.R. Unwin, Scanning Electrochemical Cell Microscopy: Theory and Experiment for Quantitative High Resolution Spatially-Resolved Voltammetry and Simultaneous Ion-Conductance Measurements, Anal Chem. 84 (2012) 2483–2491. https://doi.org/10.1021/ac203195h.

[310] C.L. Bentley, Scanning electrochemical cell microscopy for the study of (nano)particle electrochemistry: From the sub-particle to ensemble level, Electrochem Sci Adv. 2 (2022). https://doi.org/10.1002/elsa.202100081.

[311] A.J. Bard, L.R. Faulkner, Basic potential step methods, in: Electrochemical Methods: Fundamentals and Applications, 2nd ed., John Wiley & Sons, Inc, New York, 2000: p. 864.

[312] N.P. Shumbula, S.S. Nkabinde, Z.B. Ndala, S. Mpelane, M.P. Shumbula, P.S. Mdluli, Z. Njengele-Tetyana, P. Tetyana, T. Hlatshwayo, M. Mlambo, N. Moloto, Evaluating the antimicrobial activity and cytotoxicity of polydopamine capped silver and silver/polydopamine core-shell nanocomposites, Arab J Chem. 15 (2022) 103798. https://doi.org/10.1016/j.arabjc.2022.103798.

[313] B. Reidy, A. Haase, A. Luch, K. Dawson, I. Lynch, Mechanisms of Silver Nanoparticle Release, Transformation and Toxicity: A Critical Review of Current Knowledge and Recommendations for Future Studies and Applications, Materials. 6 (2013) 2295–2350. https://doi.org/10.3390/ma6062295.

[314] D.C. Choo, T.W. Kim, Degradation mechanisms of silver nanowire electrodes under ultraviolet irradiation and heat treatment, Sci Rep. 7 (2017) 1696. https://doi.org/10.1038/s41598-017-01843-9.

[315] J.-F. Collet, S.-H. Cho, B.I. Iorga, C. v. Goemans, How the assembly and protection of the bacterial cell envelope depend on cysteine residues, J Biol Chem. 295 (2020) 11984–11994. https://doi.org/10.1074/jbc.REV120.011201.

[316] F. Hamadi, H. Latrache, H. Zahir, A. Elghmari, M. Timinouni, M. Ellouali, The relation between Escherichia coli surface functional groups' composition and their physicochemical properties, Braz J Microbiol. 39 (2008) 10–15. https://doi.org/10.1590/S1517-83822008000100003.

[317] F. Xue, C.D. Cox, N. Bavi, P.R. Rohde, Y. Nakayama, B. Martinac, Membrane stiffness is one of the key determinants of E. coli MscS channel mechanosensitivity, Biochim Biophys Acta Biomembr. 1862 (2020) 183203. https://doi.org/10.1016/j.bbamem.2020.183203.

[318] R.T. Coughlin, A.A. Peterson, A. Haug, H.J. Pownall, E.J. McGroarty, A pH titration study on the ionic bridging within lipopolysaccharide aggregates, Biochim Biophys Acta Biomembr. 821 (1985) 404–412. https://doi.org/10.1016/0005-2736(85)90044-6.

[319] E.R. Rojas, G. Billings, P.D. Odermatt, G.K. Auer, L. Zhu, A. Miguel, F. Chang, D.B. Weibel, J.A. Theriot, K.C. Huang, The outer membrane is an essential load-bearing element in Gram-negative bacteria, Nature. 559 (2018) 617–621. https://doi.org/10.1038/s41586-018-0344-3.

[320] K.H. Jacobson, I.L. Gunsolus, T.R. Kuech, J.M. Troiano, E.S. Melby, S.E. Lohse, D. Hu, W.B. Chrisler, C.J. Murphy, G. Orr, F.M. Geiger, C.L. Haynes, J.A.

Pedersen, Lipopolysaccharide Density and Structure Govern the Extent and Distance of Nanoparticle Interaction with Actual and Model Bacterial Outer Membranes, Environ Sci Technol. 49 (2015) 10642–10650. https://doi.org/10.1021/acs.est.5b01841.

[321] J.L. Hutter, J. Bechhoefer, Calibration of atomic-force microscope tips, Rev Sci Instrum. 64 (1993) 1868–1873. https://doi.org/10.1063/1.1143970.

[322] R.F. Fan, D. Demaille, Preparation of tips for scanning electrochemical microscopy, in: A.J. Bard, M.V. Mirkin (Eds.), Scanning Electrochem. Microscopy, 2nd ed., CRC Press, Boca Raton, 2012: pp. 25–51.

[323] R.M. Pinto, F.A. Soares, S. Reis, C. Nunes, P. van Dijck, Innovative Strategies Toward the Disassembly of the EPS Matrix in Bacterial Biofilms, Front Microbiol. 11 (2020). https://doi.org/10.3389/fmicb.2020.00952.

[324] R.N. Forthofer, E.S. Lee, M. Hernandez, Probability Distributions, in: Biostatistics, Elsevier, 2007: pp. 103–133. https://doi.org/10.1016/B978-0-12-369492-8.50010-8.

List of figures

Figure 1.1. Schematic of the steps involved in the formation of bacterial biofilms. 22
Figure 2.1. Schematic of the SECM instrument. 26
Figure 2.2. Diffusion profiles at (**a**) a macroelectrode (planar diffusion) and (**b**) microelectrode (hemispherical diffusion). Schemes are not to scale. Schemes of SECM feedback mode for (**c**) insulating samples (negative feedback) and (**d**) conducting samples (positive feedback). Theoretical approach curves for (**e**) insulating samples (negative feedback) and (**f**) conducting samples (positive feedback). The approach curves are derived from equations 2.4 and 2.5, respectively, for a UME with RG – ratio of the insulating glass sheath radius and the electrode radius – equal to 10. 28
Figure 2.3. Schematic of SECM operational modes. (**a**) Substrate-Generation/Tip-Collection (SG/TC). (**b**) Tip-Generation/Substrate-Collection (TG/SC). (**c**) Potentiometric mode with an ion-selective electrode, where M^{n+} is a cation in solution with charge n. 29
Figure 2.4. (**a**) Square-wave waveform formed by the superimposition of a (**b**) symmetric square wave on a (**c**) base staircase potential. ESW and ΔEs determine the amplitude of the square-wave and the potential step of the staircase potential, respectively, τ is the square-wave period, if and ir are the forward and the reverse currents, respectively. The arrows highlight the time when the forward and backward current is recorded. (**d**) Square-wave voltammogram (black line) of the oxidation of 20 mmol L^{-1} $K_4Fe(CN)_6$ in 2.0 mol L^{-1} KNO_3 recorded at a Pt UME with a radius of 13 µm. The dotted lines represent the forward current (red) and the reverse current (blue). [Adapted from reference [75] ref with permission of Elsevier Science]. 30
Figure 2.5. (**a**) Schematic of the SECCM instrumentation. Detail of (**b**) single-barrel pipette and (**c**) double-barrel pipette. Abbreviations: $V1$ applied potential, $V2$ potential applied between the QRCEs, IDC induced ion current, $Isurf$ current of the sample surface. 32
Figure 2.6. Schematic of an approach curve of a SECCM single-barrel pipette and respective current response before and after the pipette-sample contact. Three parts are identified: in air, where the pipette meniscus has not yet established contact with the sample, the jump-to-contact (dotted line), and the contact regime, where a droplet is formed between the pipet and the sample. 33
Figure 2.7. Schematic of the AFM instrumentation. 34
Figure 2.8. (**a**) Simplified Lennard-Jones potential curve highlighting the force regimes for the different AFM operational modes. Schematics of the AFM operational mode: (**d**) contact mode, (**c**) non-contact mode, also known as frequency modulation, FM-AFM, and (**d**) intermittent mode, also known as amplitude modulation, AM- AFM. fA and fB denote the frequency of the probe in dependence of the material (material A and B), recorded in FM-AFM mode, d is the AFM probe-surface distance; AA and AB denote the amplitude of the probe recorded for material A and B, respectively, in AM -AFM mode. 35
Figure 2.9. Illustration of an AFM force-distance curve, highlighting the non-contact position of the cantilever (position A), the jump-to-contact with the tip indentation (position B), the maximum

contact force with high repulsive interactions (position C), and the retraction where adhesion forces produce adhesion hysteresis (position D). 38
Figure 3.1. (**a**) Schematic of the Gouy-Chapman-Stern model EDL at a positively charged surface. (**b**) Representation of the surface charge measurement using AFM. This method is based on the overlapping of AFM tip and surface EDLs. Panel adapted with permission from the Annual Review of Analytical Chemistry, Volume 15 © 2022 by Annual Reviews, reference [110]..... 45
Figure 3.2. Strategies for tailoring the surface charge density of a substrate. (**a**) Electrochemical approach. (**b**) Functionalization with negative groups (passive biofouling). (**c**) Functionalization with biocide groups (active biofouling)..... 46
Figure 3.3. Proposed mechanistic pathways for the electro-polymerization of dopamine and final polymeric products. "**E**" denotes an electrochemical reaction and "**C**" is a chemical reaction. 48
Figure 3.4. (**a**) Chronoamperometric curve during the pulsed-deposition of PDA: first cycle (black) and hundredth cycle (red). (**b**) Cyclic voltammograms were recorded in 5 mmol L^{-1} ferrocene-methanol and 0.1 M KCl before (Au substrate, black) and after e-PDA deposition (100-pulsed cycles, red); scan rate 0.05 V s^{-1}. 51
Figure 3.5. Schematics of the interactions between the AFM probe and the e-PDA substrate at (**a**) acidic pH (pH < 6), (**b**) neutral and slightly acidic pH (pH 6 – 7), and (**c**) alkaline pH (pH > 8). ... 52
Figure 3.6. (**a**) Force titration curve of e-PDA. Force titrations on e-PDA were performed in MilliQ water with the pH adjusted by adding HCl or NaOH. Histograms of the adhesion forces at (**b**) pH 3.27, (**c**) pH 6.80, and (**d**) pH 9.40 (n = 300). 53
Figure 3.7. Fitting of force-distance curves assuming constant charge conditions at (**a**) pH 3.27, (**b**) pH 4.80, and (**c**) pH 7.30. (**d**) Effect of the pH on the surface charge density of e-PDA at 25°C. Fitting parameters: curvature radius of the AFM probe r = 20 nm, surface charge of the AFM probe -0.010 C m^{-2} < σT< +0.015 C m^{-2} [190], Debye length 10^{-7} m < λD < 10^{-9} m depending on the pH. For each pH value, 20 approach curves were used to obtain the surface charge density. 55
Figure 3.8. Contact mode AFM topography images recorded in air of E. coli grown on (**a**) negatively charged PDA, (**b**) neutral PDA, and (**c**) positively charged PDA. 56
Figure 3.9. (a) Bar chart of the measured adhesion forces of *E. coli* grown on e-PDA at different pH values (error bars reflect the measurements of at least 4 cells and 300 force curves). (b) Exemplary force curves recorded in solution on *E. coli* grown at pH 5.00 (positive e-PDA, red curve), pH 5.50 (neutral e-PDA, green line), and pH 7.00 (negative e-PDA, blue line)..... 57
Figure 3.10. ATR-FTIR spectra of *E. coli* biofilms grown at positively (red), neutral (green), and negatively (blue) charged e-PDA films. 58
Figure 4.1. Schematics of the *top-down* and *bottom-up* processes for the synthesis of nanomaterials. 62
Figure 4.2. Schematic illustration of the ion beam sputtering setup, including a second gridded ion source focused on the substrate. 64
Figure 4.3. Mechanism of the electrochemical growth of NPs following the Volmer-Weber model. 65

Figure 4.4. Silver(I) release mechanism. (**a**) Oxidative dissolution of the AgNP regulated by capping agents. (**b**) Formation of a “core-shell” AgNP through the treatment of metallic AgNPs with UV-ozone and consequent dissolution of the oxide outer shell and the catalytic dissolution of the metallic silver core. The dissolution of pure metallic silver cores is not thermodynamically favored. 66
Figure 4.5. Schematic structure of (**a**) gram-negative bacterial cell envelope and (**b**) gram-positive bacterial cell envelope. AgNPs (grey particles) and silver(I) ions (blue particles) can interact with polysaccharides, phospholipids, proteins, and peptidoglycans, leading to cell envelope damage. 67
Figure 4.6. General mechanism for the antimicrobial action of AgNPs and silver(I) ions. 68
Figure 4.7. (**a**) TEM image and (**b**) particle size distribution (n = 243) of the AgNPs in the Ag-CF_X film. (**c**) XPS high-resolution spectra of Ag $3d_{3/2}$ and Ag $3d_{5/2}$ from the Ag-CF_X films. (**d**) Auger Ag(MNN) transition lines. 70
Figure 4.8. Peak deconvolution of an exemplary square wave voltammogram (silver(I) concentration in solution equals 2735 µg L^{-1}). 71
Figure 4.9. (**a**) Square wave voltammograms at different $AgNO_3$ concentrations measured in the bulk solution with a Pt UME (radius: 12.5 µm and RG = 9). (**b**) Calibration curve (red line) of silver(I) recorded at the Pt UME with increasing $AgNO_3$ concentrations. The blue lines denote the uncertainty range, and the error bars reflect three repetitive measurements. Electrolyte: 0.5 M KNO_3..... 72
Figure 4.10. (a) Cyclic voltammogram for the reduction of dissolved oxygen measured with a 12.5 µm-diameter Pt UME in 0.1 mol L^{-1} KNO_3. (b) Approach curve (black line) recorded at the Ag-CF_X surface using oxygen as a redox active species. The red line represents the simulated approach curve obtained using the fitting by Cornut and Lefrou [270]. 73
Figure 4.11. (a) First-order kinetic model of silver(I) release obtained by SECM-SWV at a distance of 79.0 µm above Ag-CF_X surface. (b) $\mathrm{Log}(\mathrm{Ag}+\mathrm{t}/\mathrm{Ag}+\infty)$ vs. $\log(\mathrm{t})$ graph according to the Korsmeyer-Peppas kinetic model of silver(I). The error bars reflect the measurement of three different samples. 74
Figure 4.12. (**a**) Schematics of the probed area by ETAAS. (**b**) Geometry of an SECM tip positioned at 79 µm to the surface and the estimated diffusion layer of silver(I). 76
Figure 4.13. (**a, b**) AFM image in air of the (**a**) patterned Ag-CF_X film on a silicon substrate and (**b**) scratched Ag-CF_X film on a silicon substrate. (**c, d**) Line scans display the depth profile before the immersion and after the immersion in water for 10 h; (**c**) the patterned Ag-CF_X sample and (**d**) the scratched Ag-CF_X sample..... 77
Figure 4.14. (**a**) Swelling behavior of patterned Ag-CF_X film monitored in water over a time of 24h. (**b**) Swelling behavior of patterned (black) and scratched (red) Ag-CF_X samples in MilliQ water monitored for 10 h. (**c**) Swelling behavior of patterned Ag-CF_X film monitored in water (black) and PBS (blue) over a time of 15 h. The error bars reflect the measurement of three different samples. 78

Figure 4.15. (**a, b**) Contact mode AFM topography image recorded in air of *P. fluorescens* after 30 h of incubation on the (**a**) pristine and (**b**) swollen surface Ag-CF_X. (**c**) Bar chart of the measured coverage. Error bars reflect the measurements of three different samples. 79
Figure 4.16. (**a, b**) Contact mode AFM topography image of *P. fluorescens* after 30 h of incubation on (**a**) a pristine sample and (**b**) a previously swollen film. Images were recorded in air. (**c, d**) Frequency counts of bacteria circularity of *P. fluorescens* after 30 h of incubation on (**c**) a pristine sample and (**d**) a previously swollen film. 80
Figure 4.17. (**a**) Schematic of the SECCM setip for the AgNPs electro-deposition on PDA using a single-barrel pipet probe. The arrows indicate the movement of the probe across the substrate (working electrode). (**b**) Detail of the confined electrochemical cell when the pipet approaches the surface and forms a contact meniscus. (**c**) Schematic of the steps for the electro-deposition of AgNPs *via* the double-potentiostatic method. 83
Figure 4.18. (**a**) Experimental current-time transient curve of the growth of silver nuclei (green line), linear fitting (blue dotted line), and square root fitting (red dotted line). (**b**) Experimental current-time transient of the growth of silver nuclei (black line) and parabolic fitting (red dotted line). Nuclei growth conditions: $AgNO_3$ concentration = 5.0 mmol L^{-1}, potential = – 0.2 V vs Ag/AgCl, substrate = PDA_{25}-gold. 85
Figure 4.19. (**a, b**) Current transient (red line) and fitted curve using equation 4.8 (black line) for the (**a**) nucleation step and (**b**) growth step of the AgNPs on PDA_{25}-gold substrates. (**c, d**) Normalized current transient (red line) and corresponding Cottrell current (black line) for (**c**) the nucleation step and (**d**) the growth step of the AgNPs on PDA_{25}-gold substrates. Current is expressed as i/iss and time as τ. 86
Figure 4.20. (**a**) SEM images (false color image) of an AgNPs spot obtained by electrochemical deposition using 0.05 mmol L^{-1} $AgNO_3$, a nucleation potential of -0.4 V (for 0.5 s), and growth potential of -0.2 V (for 2.5 s). The AgNPs at the edge and the center of the spot are highlighted in red and green. (**b**) Size distribution of the AgNPs grown at the edge (red line) and the center (green line) of the localized microelectrochemical cell. (**c**) Bar chart of the AgNPs diameter. Error bars reflect the measurement of at least 150 NPs. 87
Figure 4.21. Representative SEM images of AgNP spots obtained *via* SECCM using pipettes with a diameter of *ca*. 5 µm. Nucleation and growth potential were kept constant (En = -0.4 V and Eg = -0.2 V vs. Ag/AgCl). (**a**) [$AgNO_3$] = 5.0 mmol L^{-1}, tn = 0 s, tg = 4.0 s; substrate PDA_{25}; (**b**) [$AgNO_3$] = 5.0 mmol L^{-1}, tn = 0.5 s, tg = 3.5 s; substrate PDA_{25}; (**c**) [$AgNO_3$] = 5.0 mmol L^{-1}, tn = 0.5 s, tg = 2.5 s; substrate PDA_{25}; (**d**) [$AgNO_3$] = 0.5 mmol L^{-1}, tn = 0.5 s, tg = 2.5 s; substrate PDA_{25}; (**e**) [$AgNO_3$] = 0.05 mmol L^{-1}, tn = 0.5 s, tg = 2.5 s; substrate PDA_{25}; (**f**) [$AgNO_3$] = 5.0 mmol L^{-1}, tn = 0.5 s, tg = 2.5 s; substrate PDA_{50}. 89
Figure 4.22. Representative SEM images of AgNPs (**a**) before and (**b**) after UV-ozone treatment. (**c**) Size distribution of the AgNPs before (blue line) and after (red line) the treatment with UV-ozone. The NPs were deposited on PDA_{25} with the following parameters: En = -0.4 V, Eg = -0.2 V vs. Ag/AgCl, tn = 0.5 s, tg = 2.5 s, and [$AgNO_3$] = 0.5 mmol L^{-1}. 91

Figure 4.23. AFM topography images recorded in air of *E. coli* inoculated at the AgNPs spots/PDA. (**a**) Single-cell (green arrow) attached in the proximity of the AgNPs spot. (**b**) Overview of small communities of bacteria (blue arrow) attached at more than 20 µm from the AgNPs spot. 91
Figure 4.24. (**a-c**) AFM topography images recorded in air of *E. coli* (**a**) attached more than 20 µm from the AgNPs spot and (**c**) attached in the proximity (*ca*. 2 µm) of the AgNPs spot. (**b-d**) Longitudinal (green line) and transversal (blue line) cross-sections of *E. coli* corresponding to (**b**) Figure 4.24a and (**d**) Figure 4.24c..... 92
Figure 4.25. Bar charts of the measured (**a**) adhesion forces and (**b**) Young´s modulus. Error bars reflect the measurements of at least 9 cells and 430 force curves. 93

CURRICULUM VITAE

PERSONAL INFORMATION

Name **Giada** | Surname **Caniglia**

giada.caniglia@uni-ulm.de

Germany

Sex Female | Nationality Italian

WORK EXPERIENCE

Apr 2017 – May 2017 Practice in Nuclear Magnetic Resonance Service, *Universidad de La Laguna (Tenerife, Spain)*

Work: H-NMR, C^{13}-NMR, 2D-NMR, 2D-COSY

Feb 2016 – Apr 2016 Practice in Quality Laboratory Control, *Compañia Cervecera de Canarias (Tenerife, Spain)*

Work*: brewing quality analysis*

Jul 2015 – Nov 2015 Practice in Inorganic Chemistry department, *Universidad de La Laguna (Tenerife, Spain)*

Work*: synthesis and characterization of tungsten bronzes (solid state synthesis, XPS analysis, SEM analysis)*

EDUCATION

2023 - Present **Postdoctoral researcher at Ulm University**

Ulm University, Ulm (Germany)

Topic: Investigation of light-driven catalysis *via* scanning probe microscopy

Supervisor: Christine Kranz

2019 – 2023 **PhD student at Ulm University**

Ulm University, Ulm (Germany)

Thesis: Investigation of antimicrobial and antibiofouling systems *via* scanning probe microscopy

Supervisor: Christine Kranz

Jan 2022 – Feb 2022: Secondment in the Warwick Electrochemistry & Interfaces Group at University of Warwick, under Prof. Dr. Patrick Unwin (Coventry, United Kingdom).

2017 – 2019 **Researcher at Universidad de La Laguna**

Universidad de La Laguna, San Cristobal de La Laguna (Spain)

Topic: Application of scanning electrochemical microscopy for the characterization of the initial stages of corrosion processes

Supervisors: Ricardo M. Souto Suárez and Javier Izquierdo Pérez

2016 – 2017 **Master in chemistry**

Universidad de La Laguna, San Cristobal de La Laguna (Spain)

Thesis: Gelling properties of carbohydrate based triazoles

Supervisor: Jesús María Trujillo Vázquez

2012 – 2016 **Bachelor in Chemistry**

Universidad de La Laguna, San Cristobal de La Laguna (Spain)

Thesis: Substitution reactions in cobalt (II) complexes. Kinetic study of the reaction and spectroscopic analysis

Supervisors: Pedro F. Martín Zarza and Francisco R. García Manrique

PERSONAL SKILLS

Mother tongue Italian

Foreign languages Spanish (C2); English (B2); German (A2)

Organizational skills **2022:** 12th advanced study course on optical chemical sensors (ASCOS, Obergurgl, Austria)

2020: Participation in the EU *vs* Virus Heckathon in the Health and Life Challenge and Social and Political Cohesion Challenge (on-line)

2015 – **2017**: Member of the Student Congress Organizing Committee of the Science Faculty (Universidad de La Laguna, Spain)

Job-related experience Scanning Electrochemical Microscopy (SECM); Atomic Force Microscopy (AFM); AFM-based force spectroscopy; Microbiology; Electrochemistry; Nuclear Magnetic Resonance; X-ray photoelectron spectroscopy (XPS)

CONFERENCES

2023 *Scanning probe microscopies and their potential to study biofilm formation and antimicrobial activity* presented in the Break Biofilm Workshop (Vienna, Austria)

Authors: G. Caniglia, C. Kranz

2023 *Infrared spectroscopic and atomic force studies on the role of surface charge for the anti-biofouling properties of polydopamine films* presented in the Break Biofilm Workshop (Vienna, Austria)

Authors: A. Teuber, G. Caniglia, C. Kranz, B. Mizaikoff

2022 *Electrochemical deposition of silver-nanoparticles and investigation of their antimicrobial activity using scanning probe microscopes* presented in the ISE Regional Meeting (Prague, Czech Republic)

Authors: G. Caniglia, G. Tezcan, D. Valavanis, P. Unwin, C. Kranz

2022 *Structured silver-nanoparticles-modified polydopamine films: synthesis and antimicrobial activity* presented in the 18th International Conference on Electroanalysis (ESEAC, Vilnius, Lithuania)

Authors: G. Caniglia, G. Tezcan, D. Valavanis, P. Unwin, C. Kranz

2022 *Mapping the antimicrobial properties of polydopamine films and the role of surface charge via atomic force spectroscopy and infrared spectroscopy* presented in the Biofilms 10 Conference (Leipzig, Germany)

Authors: G. Caniglia, A. Teuber, B. Mizaikoff, C. Kranz

2022 *A novel bacterial sensing platform: Diamond Thin-Film Waveguides based on Quantum Cascade Laser Mid-Infrared Spectroscopy* presented in the Biofilms 10 Conference (Leipzig, Germany).

Authors: A. Teuber, G. Caniglia, C. Kranz, B. Mizaikoff

2021 *Charge density of Escherichia coli biofilms studied with Scanning Probes Techniques* presented in the 72nd Annual Meeting of the ISE (on line)

Authors: G. Caniglia, C. Kranz

2021 *Characterization of polydopamine thin films and their antibacterial properties studied with scanning probes microscopy* presented in the 2021 Fall Meeting of the European Materials Research Society (E-MRS, on line)

Authors: G. Caniglia, S. Daboss, C. Kranz

2021 *Charge density of Escherichia coli biofilms studied with Scanning Probes Techniques* presented in the 72stAnnual Meeting of the International Society of Electrochemistry (on-line)

Authors: G. Caniglia, C. Kranz

2021 *Antimicrobial activity of silver nanoparticle-based films studied by Scanning Probe Microscopy*, presented in the XXVI International Symposium on Bioelectrochemistry and Bioenergetics of the Bioelectrochemical Society (on-line)

Authors: G. Caniglia, A. Heinzmann, M.C. Sportelli, A. Valentini, N. Cioffi, C. Kranz

2020 *Antibacterial activity of silver-nanoparticle-based films investigated with scanning probe microscopy*, presented in the 71stAnnual Meeting of the International Society of Electrochemistry (on-line)

Authors: G. Caniglia, A. Heinzmann, M.C. Sportelli, A. Valentini, N. Cioffi, C. Kranz

2020 *Scanning probe microscopy study on antimicrobial silver-nanoparticle-based composite film*, presented in the XXII Annual Linz Winter Workshop (Linz, Austria)

Authors: G. Caniglia, A. Heinzmann, M.C. Sportelli, A. Valentini, N. Cioffi, C. Kranz

2019 *SECM kinetic study of the heterogeneous adsorption of green corrosion inhibitors*, presented in the10thInternational Workshop on SECM and related techniques (Fontainebleau, France)

Authors: J. Izqueirdo, G. Caniglia, S. Varvara, R.M. Souto

2019 C*orrosion inhibition respectful with the environment. Kinetic and microelectrochemical study*, presented in the XII Congreso de Estudiantes de la Sección de Química (Universidad de La Laguna, Canary Island, Spain)

Authors: G. Caniglia, J. Izquierdo, R.M. Souto

2018 *Study of corrosive processes by scanning electrochemical microscopy*, presented in the XXII Semana Científica Antonio González (Canary Islands, Spain)

Authors: G. Caniglia, J. Izquierdo, R.M. Souto

2018 *Supramolecular Structure of Aril Triazoles*, presented in the XI Congreso de Estudiantes de la Sección de Química (Universidad de La Laguna, Canary Island, Spain)

Authors: G. Caniglia, A. Favero Giorgis, J.M. Trujillo Vázquez, S. Tejera Díaz, R. Lelia Dorta

2017 *Supramolecular Structure of Aril Triazoles*, presented in the XXI Semana Científica Antonio González (Canary Islands, Spain)

Authors: G. Caniglia, A. Favero Giorgis, J.M. Trujillo Vázquez, S. Tejera Díaz, R. Lelia Dorta

2015 *Carbon Quantum Dots: the chemistry of carbon in nanoparticles*, presented in the XI Congreso de Estudiantes de la Sección de Química (Universidad de La Laguna, Canary Island, Spain)

Authors: G. Caniglia, A. Favero Giorgis, J.A. Palenzuela López, M. del Mar Afonso Rodríguez

2015 *Biological Oxidations. What can we learn from the P450 system?* presented in the XI Congreso de Estudiantes de la Sección de Química (Universidad de La Laguna, Canary Island, Spain)

Authors: G. Caniglia, A. Favero Giorgis, P.F. Martín Zarza

2014 *Organic Chemistry: bridge between science and archeology*, presented in the X Congreso de Estudiantes de la Sección de Química (Universidad de La Laguna, Canary Island, Spain)

Authors: G. Caniglia, A. Favero Giorgis, J.A. Palenzuela López, M. del Mar Afonso Rodríguez

SEMINARS AND SCHOOLS

2023 Catalight Spring School: workshops and tutorials on photocatalysis (Bad Staffelstein, Germany)

2022 12th advanced study course on optical chemical sensors (ASCOS, Obergurgl, Austria) – Part of the organization staff

2022 CataLight Kick-off: introduction to CataLight project (Jena, Germany)

2022 Break Biofilm training event: build-up a virtual company (Ulm, Germany)

2022 Break Biofilm training event: advanced electrochemistry (Warwick, UK)

2021 Break Biofilm training event (Aarhus, Denmark)

2021 *Advanced scientific writing: how to write for high impact journals* (Aarhus University, on-line)

2020 Break Biofilm training event: how to start a start-up (Oviedo, Spain)

2019 *Chess 2019 School. Conventional and high-energy spectroscopies surface analysis* (Florence, Italy)

2018 *Introduction to Scanning Probe Microscopy, Electrochemical SPM and Hybrid SPM techniques*, by apl. Prof. Dr. Christine Kranz, head of Kranz Research Group at Ulm University (Ulm, Germany)

2018 *BCZY-MDC (M: Y, Gd) composites for hydrogen separation: chemical and mechanical stability in simulated operational environment*, by Dr. Monica Fabrizio, executive researcher in the Institute of Condensed Matter Chemistry and Energy Technologies (Padova, Italy)

2018 *Engineering of thermoelectric materials for low-medium temperature applications*, by Dr. Monica Fabrizio, executive researcher in the Institute of Condensed Matter Chemistry and Energy Technologies (Padova, Italy)

GRANTS AND SCHOLARSHIPS

2021 Graduate student award by E-MRS 2021 fall meeting

2019 H2020-MSCA-ITN (PhD Studies)

2018 Cabildo de Tenerife Scholarship (PhD Studies)

2017 Spanish State Scholarships (Master Studies)

2012 – 2016 Spanish State Scholarships (Bachelor Studies)

PUBLICATIONS

1.Tejera, S.; Caniglia, G.; Dorta, R. L.; Favero, A.; González-Platas, J.; Vázquez, J. T. Influence of the Cis / Trans Configuration on the Supramolecular Aggregation of Aryltriazoles. *Beilstein J. Org. Chem.* **2019**, *15* (15), 2881–2888. https://doi.org/10.3762/bjoc.15.282.

2.Varvara, S.; Caniglia, G.; Izquierdo, J.; Bostan, R.; Găină, L.; Bobis, O.; Souto, R. M. Multiscale Electrochemical Analysis of the Corrosion Control of Bronze in Simulated Acid Rain by Horse-Chestnut (Aesculus Hippocastanum L.) Extract as Green Inhibitor. *Corros. Sci.* **2020**, *165*, 108381. https://doi.org/10.1016/j.corsci.2019.108381.

3.Caniglia, G.; Kranz, C. Scanning Electrochemical Microscopy and Its Potential for Studying Biofilms and Antimicrobial Coatings. *Anal. Bioanal. Chem.* **2020**, *412* (24), 6133–6148. https://doi.org/10.1007/s00216-020-02782-7.

4.Hellmann, A.; Caniglia, G.; Kranz, C. Applications of Miniaturized Electrochemical Biosensors. In *Reference Module in Biomedical Sciences*; Elsevier, 2022. https://doi.org/10.1016/B978-0-12-822548-6.00152-7.

5.Caniglia, G.; Tezcan, G.; Meloni, G. N.; Unwin, P. R.; Kranz, C. Probing and Visualizing Interfacial Charge at Surfaces in Aqueous Solution. *Annu. Rev. Anal. Chem.* **2022**, *15* (1), 247–267. https://doi.org/10.1146/annurev-anchem-121521-122615.

6.Caniglia, G.; Sportelli, M. C.; Heinzmann, A.; Picca, R. A.; Valentini, A.; Barth, H.; Mizaikoff, B.; Cioffi, N.; Kranz, C. Silver-Fluoropolymer (Ag-CFX) Films: Kinetic Study of Silver Release, and Spectroscopic-Microscopic Insight into the Inhibition of P. Fluorescens Biofilm Formation. *Anal. Chim. Acta* **2022**, *1212* (April), 339892. https://doi.org/10.1016/j.aca.2022.339892.

7.Caniglia G.; Teuber A.; Mizaikoff B.; Kranz C. Anti-biofouling properties of polydopamine films: the role of surface charge via atomic force spectroscopy and infrared spectroscopy. *Anal. Bioanal. Chem.* **2023**, *415*, 2059-2070**.** https://doi.org/10.1007/s00216-022-04431-7.

8. Teuber A.; Caniglia G.; Wild M.; Godejohann M.; Kranz C.; Mizaikoff B. Espresso Laser Spectroscopy: Diamond Thin-Film Waveguides for the Qualitative and Quantitative Analysis of Caffeine. *ACS Sensors*, **2022**, *8* (5), 1871-1881. https://doi.org/10.1021/acssensors.2c01841.

Ulm, 30.05.2023

(Place, Date)

(Signature)

DECLARATION OF AUTHORSHIP

I declare that I have developed this PhD thesis independently and through my own research and that I have not used any aids other than those listed in the work. All statements taken *verbatim* or in spirit from publications are clearly marked. The literature used is indicated in the list of references.

EIDESSTATTLICHE ERKLÄRUNG

Hiermit erkläre ich, dass ich die vorliegende Dissertation selbständig und durch eigene Recherche angefertigt habe und keine anderen als die in der Arbeit angeführten Hilfsmittel verwendet habe. Alle Stellen die wörtlich oder sinngemäß aus Veröffentlischungen entnommen wurden, sind als solche gekennweichnet. Die verwendete Literatur ist im Quellenverzeichnis angegeben.

Ulm, 14.12.2022 _____

(Place, Date) (Signature)